Self-seeded III-V Semiconductor Nanowire Growth by Metal-organic Chemical Vapor Deposition (MOCVD)

by
Sema Ermez

B.Sc. Materials Science and Engineering
Sabancı University, 2010

Submitted to the Department of Materials Science and Engineering
In Partial Fulfillment of the Requirements for the Degree of

Doctor of Philosophy
at the
Massachusetts Institute of Technology

June 2016

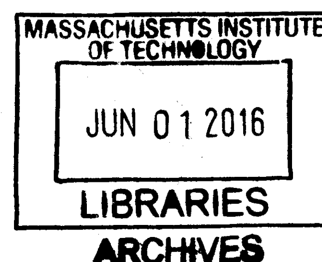
MASSACHUSETTS INSTITUTE OF TECHNOLOGY
JUN 01 2016
LIBRARIES
ARCHIVES

© 2016 Massachusetts Institute of Technology. All rights reserved.

Signature of Author: Signature redacted
Department of Materials Science and Engineering
April 29th, 2016

Certified by: Signature redacted
Silvija Gradečak
Associate Professor in Materials Science and Engineering
Thesis Supervisor

Accepted by: Signature redacted
Donald R. Sadoway
Chair, Departmental Committee on Graduate Students

Self-seeded III-V Semiconductor Nanowire Growth by Metal-organic Chemical Vapor Deposition (MOCVD)

by
Sema Ermez

Submitted to the Department of Materials Science and Engineering on April 29, 2016
In Partial Fulfillment of the Requirements for the Degree of
Doctor of Philosophy in Materials Science and Engineering

III-V semiconductor epitaxial nanowires have gained significant attention in recent years, as they showcase an opportunity to combine III-V material properties with a non-planar morphology. To date, semiconductor devices have been continuously engineered to realize opto-electronic devices with ever smaller size, higher efficiency, and lower power consumption. However, many device improvements have reached fundamental physical limitations. One way to address these challenges is to adapt a non-planar device structure. Nanowires are one-dimensional structures that can be grown on a substrate with epitaxial relationship using traditional vapor deposition techniques such as metal-organic chemical vapor deposition (MOCVD). Therefore, the novelty of non-planar morphology can be achieved using industrial scale high throughput deposition techniques. To realize the full potential of nanowires as building blocks in a range of different devices, growth of nanowire arrays with controlled density, morphology, composition and alignment is necessary.

In this thesis, we demonstrate controlled growth of self-seeded III-V binary and ternary nanowires by MOCVD. First, self-seeded binary III-V nanowire growth is demonstrated for gallium (Ga)-seeded gallium arsenide (GaAs) nanowires. High yield of vertical nanowires are grown reproducibly by a two-step approach: *in situ* deposition of Ga seed particles at high temperatures (500°C – 600°C), followed by GaAs nanowire growth at lower temperatures (420°C – 435°C). The fabricated GaAs nanowires show a single crystalline structure at the base and occasional twin planes along the nanowire growth direction. We develop a growth model based on incorporation and extraction of Ga from seed particle to explain the observed tapering of nanowires.

Second, control over the density and diameter of nanowire arrays is achieved by controlling seed deposition conditions. We demonstrate that higher seed deposition temperatures or changing the GaAs substrate orientation from (111)A to (110) and (111)B yield reduced areal density and larger nanowire diameters. Seed deposition temperature affects the surface diffusion of Ga adatoms, whereas substrate orientation affects the nucleation of seed particles due to varied chemical potential of Ga adatoms and surface energies on different surface orientations.

Lastly, controlled self-seeded ternary III-V nanowire growth is realized in the case of Ga-seeded $GaAs_{1-x}P_x$ nanowire growth on GaAs substrates. Composition control for $x = 0 - 0.3$ and growth of GaP nanowires are demonstrated by varying group-V precursor percentage. It was found that strain due to lattice mismatch between GaAs substrate and GaAsP nanowires can be released due to nanowire geometry. Cathodoluminescence measurements have shown emission

of light in GaAsP band gap energies, confirming the successful growth of nanowires in this ternary material system.

The methods developed for self-seeded growth of GaAs and GaAsP nanowires, as well as density and diameter control of self-seeded growth are extendable to other self-seeded III-V nanowire material systems.

Thesis Supervisor: Silvija Gradečak

Title: Associate Professor of Materials Science and Engineering

Acknowledgments

First, I would like to thank my thesis advisor, Professor Silvija Gradečak, for her guidance and support during my PhD. She has been a great mentor as well as a role model, and I feel very fortunate to have the opportunity to learn so much from her. Thanks to her insightful comments, continuous support, and patience I was able to grow as a scientist and complete my PhD.

I would like to thank my thesis committee members, Professor Lionel C. Kimerling and Professor Eugene A. Fitzgerald, for their great insight and suggestions to my research. Their immense knowledge on semiconductor growth has helped me to ask the right questions as I tried to understand the science behind nanowire growth.

I would like to thank my collaborators, Dr. Filippo Fabbri and Dr. Kunal Mukherjee for helping me in acquisition and interpretation of optical properties and strain characterization of ternary nanowires. I would like to thank to Dr. Eric Jones for mentoring and supporting me on MOCVD training and operation as well as fruitful discussions on nanowire growth. Furthermore, I would like to thank Fitzgerald group members for sharing invaluable information on MOCVD operation.

I owe many thanks to Gradečak group, current members and alumni, who have been very supportive and made my life at MIT very enjoyable. Thanks to the collaborative nature of group environment and constructive feedback from group members, I was able to improve myself and grow as a scientist. Special thanks to my office mates, Jordan Chesin and John Hanson, and unofficial office mate Eric Jones, for dragging me out of the office with coffee breaks.

Finally, I would like to thank to my friends and family, who made my life complete. My roommates, Gozde Rainville, Nancy Twu and Ece Alpaslan, thank you for being great friends and making me feel at home. My classmates Nancy Twu, Kunal Mukherjee and Tim Milakovich, thank you for making grad school such a great experience. My fiancé, Onur Can Ulusel, thank you for always supporting me, making me laugh and helping me keep a positive perspective. And finally I would like to my family – my mom and dad, my brother, sister-in-law and niece for their continuous love and support.

Table of Contents

Chapter 1: Introduction **21**

1.1. Motivation 21

1.2. Nanowire fabrication techniques 24

1.2.1 Top-down nanowire fabrication 24

1.2.2 Bottom-up nanowire growth 26

1.3. Outline of the thesis 33

Chapter 2: Experimental methods **35**

2.1. Growth of self-seeded III-V nanowire by MOCVD 35

2.1.1 Metal-organic chemical vapor deposition 35

2.1.2 Self-seeded III-V binary GaAs nanowire growth 37

2.1.3 Self-seeded III-V ternary GaAsP nanowire growth 38

2.2. Structural and compositional characterization 40

2.2.1 Scanning electron microscopy (SEM): morphology, density, diameter and length of nanowires 41

2.2.2 Transmission electron microscopy (TEM): structure of nanowires 42

2.2.3 Energy dispersive x-ray spectroscopy (EDS) to determine composition 43

2.2.4 High resolution x-ray diffraction (XRD) reciprocal space mapping (RSM) to determine strain and composition 47

2.3. Optical characterization of nanowires using cathodoluminescence (CL) 50

Chapter 3: Binary material system - GaAs nanowire growth **53**

3.1. Introduction 53

3.2. Ga-seeded GaAs nanowire growth 55

3.3. Nucleation and growth of nanowires 60

3.4. Nanowire morphology: Tapering.. 64

3.5. Growth Model 65

3.6. Investigation of radial shell growth 67

3.7. Effect of growth temperature 69

3.8. Effect of AsH_3 flow during annealing and during cooling 71

3.9. Conclusions... 73

Chapter 4: Density and diameter control of self-seeded nanowires.................................. 75

4.1. Introduction... 76

4.2. Effect of seed deposition temperature on density and diameter control 78

4.3. Effect of substrate orientation on density and diameter control 81

4.4. Seed nucleation kinetics.. 83

4.5. Effect of seed deposition duration on nanowire density 87

4.6. Conclusions... 92

Chapter 5: Ternary material system - GaAsP nanowire growth 93

5.1. Introduction... 93

5.2. Self-seeded GaAsP nanowire growth 95

5.3. Composition control using group V flow percentage and growth temperature...... 101

5.4. Strain and composition measured by x-ray diffraction... 110

5.5. Optical properties of GaAsP nanowires.. 120

5.6. Summary 123

Chapter 6: Gas sensor application 125

6.1. Introduction... 125

6.2. Gas sensor device structure 126

6.3. Volatile organic compound sensing using GaAs/polymer chemiresistors 128

6.4. Conclusion 129

Chapter 7: Conclusions 131

7.1. Summary of the thesis 131

7.2. Suggested future work 135

7.2.1 Nanowire growth on more abundant substrates 135

7.2.2 Axial heterostructures 135

List of Figures

Figure 1.1 Nanowire heterostructures. a) Substrate junction where substrate and nanowire are composed of different materials or doping levels to create a junction at the interface. b) Axial heterostructure where nanowire composition or doping is altered along the nanowire length. c) Radial (core-shell) heterostructure where composition or doping levels are altered in radial direction. Green and blue colors represent different material composition or doping levels. 23

Figure 1.2 Nanowire fabrication and growth processes. a) Top-down nanowire fabrication by patterning (top) and subsequent etching (middle). After fabrication, pattern can be etched (bottom). b) Bottom-up nanowire growth by selective area epitaxy (SAE). First, a mask layer is patterned (top), then epitaxial growth only occurs in the openings of the mask layer (middle). Oxide mask layer can be removed by etching (bottom). c) Seed particle assisted nanowire growth. Seed particles are deposited on the substrate (top) and preferential decomposition of precursors and nucleation at the seed particle/nanowire interface leads to one-dimensional nanowire growth (middle). Seed particles can be removed by selective etching (bottom). Gray, green, transparent and yellow represent metal, nanowire material, oxide and seed metal, respectively........ 26

Figure 1.3 Vapor-liquid-solid (VLS) nanowire growth mechanism described for Si nanowire growth. a) Growth stages of VLS growth of Si nanowires and b) corresponding phase diagram. Solid gold particle (step 1) alloys with Si vapor and becomes a AuSi alloy. As Si content in the alloy particle increases, particle enters liquid phase (step 2) and becomes a

supersaturated AuSi alloy (step 3), which drives formation of Si layer at the particle/substrate interface (step 4). Nanowire growth occurs as step 4 is repeated............ 28

Figure 1.4 Effective growth mechanisms during particle-seeded GaAs nanowire growth. Ga precursor (TMGa) reaches the collector particle via surface diffusion and direct impingement, decomposes at the collector surface, and contributes vapor-liquid-solid (VLS) growth (left). Ga precursor decomposes during gas-phase transport and Ga ad-atoms reach the nanowire sidewalls and deposit on sidewalls via vapor-solid (VS) mechanism (right). (Image courtesy of SK Lim). 29

Figure 2.1 Schematic of the MOCVD setup used in this work. Precursors are delivered to the reaction zone where nanowire growth occurs... 36

Figure 2.2 Growth procedure schematic of a typical self-seeded GaAs nanowire growth. Temperature profile is given by solid line and flow rates are represented by dashed lines. 38

Figure 2.3 Growth procedure schematic of a typical self-seeded GaAsP nanowire growth. Temperature profile is given by solid line and flow rates are represented by dashed lines. 40

Figure 2.4 Various signal produced upon interaction of high-energy electron beam with a sample. Using these signals, morphology, structure, chemical composition and optical properties of the sample can be investigated. 41

Figure 2.5 EDS spectrum of GaAsP nanowire showing characteristic x-ray energies of Ga, As, P elements emerging from nanowire and Cu element emerging from TEM grid................... 44

Figure 2.6 Schematic of the x-ray diffraction setup for reciprocal space mapping of (422) plane of a sample with <111> normal. X-ray beam incidence angle (ω^-), exit angle (ω^+) total scattering angle (2θ), angle between the surface normal and scattering vector (τ), and angle between surface normal and scattering plane (φ) are shown. 47

Figure 3.1 Ga seed formation by *in situ* deposition. SEM image of Ga droplets formed on the GaAs (111)B growth substrate immediately after the Ga deposition step at 420°C. 56

Figure 3.2 Self-seeded nanowire growth. (a) SEM image of a GaAs nanowire array showing the alignment of nanowires on the GaAs (111)B substrate. (b) SEM image of a single nanowire taken at 45° tilt showing the nanowire morphology with two regions (base and nanowire) that have distinct tapering rates. (c) Nanowire growth schematic; *in situ* Ga seed deposition is followed by nanowire nucleation and growth. The balance of Ga incorporation into the seed particle and Ga extraction from the seed particle determines the tapering of the nanowire during growth. Nanowire length and diameter is denoted as *l* and *d*, respectively. 57

Figure 3.3 Effect of low seed deposition temperature on repeatability of nanowire growth. (a, b) SEM images of different GaAs nanowires growths performed at the same seed deposition temperature and growth temperature (420°C) and same precursor flow rates. Repeatability of growths is unachievable in the case of low temperature seed deposition conditions....... 59

Figure 3.4 Structure of the nanowire base region. (a) Cross-sectional TEM image of the nanowire base and substrate. Outside of the nanowire base, defective overgrowth layer can be seen. The red box outlines the base-substrate junction, shown in high magnification in (b) and (c). The green and orange boxes outline the regions used to obtain SAD patterns from the base and nanowire, respectively. (b-c) High resolution TEM images of the interface between the base and substrate, taken along ⟨10-1⟩ zone axis. Base region is defect-free whereas a defective overgrowth layer can be seen outside of the nanowire base. (d-e) SAD patterns from the base (d) and nanowire (e) regions. Twinning planes in the nanowire cause double spots seen in the nanowire SAD pattern. (f-g) Schematic

representation of two possible base formation mechanisms: base formation occurs as a part of the nucleation process (f) or as a result of preferential sidewall deposition at the substrate-nanowire junction (g). 61

Figure 3.5 Structural analysis of the nanowires. (a) Bright field TEM images of GaAs nanowires along the [10-1] zone axis. (b) High resolution TEM image showing rotational twins. (c) SAD pattern obtained from the region shown in (a) with double spot structure as a result of rotational twins.. 63

Figure 3.6 Length-diameter relationship. Length of nanowires (*l*) *vs.* starting nanowire diameter (*d*) for growths performed with the same V/III ratio, but with different seed deposition conditions ("temperature" refers to the seed deposition temperature, whereas "TMGa" refers to the flow rate of Ga precursor during the 60 s Ga seed deposition step)................ 65

Figure 3.7 Effect of radial growth on the nanowire structure investigated by TEM. (a) Bright field TEM images of GaAs nanowires along the [10-1] zone axis. (b) High resolution TEM image showing defective radial growth nucleated through the twin plane (shown in red arrow). (c) SAD pattern obtained from the region shown in (a) where extra spots appear due to twinned structure of the radial growth.. 68

Figure 3.8 Growth temperature studies of GaAs nanowire growth. (a-e) SEM images of GaAs nanowire growth with similar growth conditions except growth temperature. Growth temperature ranges from 420°C to 480°C, as denoted on each image. Increasing growth temperature worsens the nanowire morphology and nanowire kinking is observed........... 69

Figure 4.1 Effect of Ga seed deposition temperature on the nanowire density and diameter. (a-e) Top-view SEM images of GaAs nanowires grown with different Ga seed deposition temperatures (indicated in each image). All growths are performed on GaAs (111)B

substrates at 435°C. Nanowires appear as dots in the top-view images because they grow vertically on the substrate. Insets show the nanowire morphology obtained at a 45° tilt. (f) Areal density and average diameters of nanowire arrays as a function on the seed deposition temperature. 80

Figure 4.2 Effect of substrate orientation on nanowire density and diameter. (a-c) GaAs nanowire growth on (111)B, (110) and (111)A substrate, respectively. Areal density is given at the bottom-left corner of each image. 82

Figure 4.3 Chemical potentials and surface energies that affect seed particle formation. Here, chemical potential of Ga adatoms is indicated as μ^{surf}_{Ga}, chemical potential of Ga in liquid form is μ^{l}_{Ga}, surface tension of Ga liquid particle is γ_{lv}, surface energy of substrate under Ga-rich conditions is γ_{sv}, and interface energy between substrate - Ga liquid seed is γ_{ls}...... 84

Figure 4.4 The dependence of nanowire density on seed deposition temperature shown in Arrhenius plot. Seed deposition is performed by flowing TMGa at 1.67 sccm for 1 min. Density is measured after nanowire growth........ 85

Figure 4.5 Effect of Ga seed deposition duration on GaAs nanowire density. Seed deposition is performed at 420°C with TMGa flow of 0.674 sccm and denoted on the caption for each nanowire growth. Top row shows top-view SEM images nanowires to reveal density, whereas bottom row shows 45°tilt SEM images to reveal the morphology of nanowires. Nanowire growth conditions are the same for all growths, with V/III=5........ 88

Figure 5.1 Schematic of GaAsP nanowire growth. First, Ga seed particles are *in situ* deposited on the substrate by flowing TMGa at higher temperatures (left). Then, at the nanowire growth temperature, GaAs stem is nucleated by flowing TMGa and AsH_3. (middle). Introduction of GaAs stem was found essential to increase yield of vertical GaAsP nanowire

growth. Then, GaAsP nanowire growth occurs by flowing TMGa, AsH_3 and PH_3. Ga incorporates into the seed particle during growth, and then extracted at the seed/nanowire interface as a result of GaAsP layer nucleation. The balance of Ga incorporation and extraction dictates seed volume, hence nanowire diameter. 96

Figure 5.2 GaAsP nanowire morphology as a function of PH_3 %. (a-g) SEM images taken at 45°tilt show the morphology of nanowires, where PH_3% for each growth is given at the top of each image. Vertical nanowire nucleation yield decreases with increasing PH_3%. 98

Figure 5.3 Effect of PH_3% and growth temperature on GaAsP nanowires. SEM images taken at 45°tilt shows the morphology of GaAsP nanowires grown at 450°C (a-c), 475°C (d-f) and 500°C (g-i). PH_3% ranges 70%, 90% and 98% from left to right. Increasing growth temperature and PH_3% results in to lower vertical nanowire yield. 100

Figure 5.4 Composition of GaAsP nanowires as a function of the group V precursor composition. Composition is determined by quantification and averaging of tens of EDS-TEM point spectra for each growth. P content increases with increasing PH_3 flow percentage. Growth temperature does not affect composition of nanowires. The trend of composition (x) as a function of PH_3% can be fitted to an equation shown in the inset with a parameter k, which represents incorporation ratio. 102

Figure 5.5 $GaAs_{1-x}P_x$ thin film growth. Phosphorus content of thin film (x) as a function of the input phosphine ratio for growth temperatures between 650 - 850°C. Adapted from Smeets.[126] 105

Figure 5.6 Compositional homogeneity along the length of GaAsP nanowires. a) Phosphorus distribution along the nanowire length for different growth temperatures, given in

percentage, and b) artificially-colored dark-field STEM images. These nanowires are grown with 98% PH_3 flow percentage; scale bar is the same for all nanowires shown in (b)....... 107

Figure 5.7 EDS linescans and corresponding dark-field STEM images showing elemental distributions along nanowire diameter for growths performed with 98% PH_3 flow at different growth temperatures (labeled for each figure). EDS intensity is shown in red, green and blue for Ga, As and P, respectively (a-c, images on the left). Linescan locations are given by yellow line on the dark-field STEM images (a-c, images on the right)......... 109

Figure 5.8 2theta-omega diffraction maps shown for (422) reflections coming from GaAsP nanowires and GaAs (111)B substrate. We qualitatively investigate the shift of (422) peak coming from GaAsP nanowire as a function of PH_3 percentage during growth (top right turquoise spot in images is GaAsP reflection, below 90% PH_3 the spot for GaAsP nanowire overlaps with GaAs spot). All nanowires are grown at 450°C. 111

Figure 5.9 Effect of growth temperature and PH_3% on P composition, deduced from 2theta-omega diffraction maps. Growth conditions are given at the label of each image. (422) reflections coming from GaAsP nanowires and GaAs (111)B substrate are labeled in figure (f). GaAsP peak shifts in 2theta and omega, showing the changes in lattice spacing as a result of compositional changes.. 113

Figure 5.10 RSM ($q_x - q_z$ maps) of (422) reflection of GaAsP nanowires grown on GaAs (111) substrates under different growth temperature and PH_3% conditions (each image is labeled with the growth conditions). Composition and strain is later calculated using the peak positions of GaAs and GaAsP reflections.. 115

Figure 5.11 a) Composition and b) relaxation of GaAsP nanowires calculated using RSM of (422) reflection by XRD. P content increases with increasing PH_3% during growth, similar

to results measured by EDS (a). Relaxation graph shows the relaxation of strain in GaAsP built up due to lattice mismatch between GaAs and GaAsP. Nanowires show over 65% relaxation in all cases; however, a clear trend between growth conditions and relaxation was not observed. 117

Figure 5.12 The source of GaAsP peak in RSM is nanowires. a, b) RSM is performed on a GaAs substrate that has GaAsP nanowires. c) Corresponding SEM image of sample used to obtain maps in (a, b) is shown. d, e) RSM is performed on a sample, where GaAsP nanowires are removed mechanically. f) Corresponding SEM image of sample used to obtain maps in (d, e). Nanowires are removed but an overgrowth layer is observed. During growth, along with nanowires, a parasitic over-growth occurs on the substrate. By removing the nanowires but keeping the over-growth layer intact, we performed RSM measurement and observed only GaAs peak. Therefore, the over-growth layer does not contribute to the information on RSM and GaAsP peak comes from GaAsP nanowires. 119

Figure 5.13 Optical properties of GaAsP nanowires measured by CL in SEM. a,d) SEM image, b,e) PanCL image at room temperature and c,f) spot mode analysis at 77K are shown for GaAsP nanowire growths performed with 90% PH_3 (a-c) and 95% PH_3 flow percentage at 450°C. 121

Figure 5.14 Room temperature monochromatic CL (720nm) of GaAsP nanowires on GaAs (111)B substrate grown at 450°C with 95% PH_3 flow percentage. Emission at 720nm would indicate a P composition x = 0.24. Comparing SEM image and monoCL map of corresponding region confirms that nanowire bases consist of GaAsP. Locations of the nanowire bases are labeled for ease of comparison. 122

Figure 6.1 The structure of GaAs nanowire/PEDOT polymer gas sensor. a-b) SEM images of GaAs nanowires grown on (110) substrate (shown at top view) and (111)A substrate (shown at 45° tilt), respectively. The insets show the nanowire morphology at 45° tilt, scale bar is 500nm. c) Schematic of gas sensor device structure, where GaAs nanowires are coated with PEDOT polymer and metal contacts are placed to measure the resistance. d-e) SEM images of PEDOT polymer coating on GaAs nanowires grown on GaAs (110) and (111)A, respectively (shown at 45° tilt). Conformal coating of polymer can be seen in the insets of the images. 127

Figure 6.2 Resistive response of GaAs/PEDOT polymer gas sensors to a) methanol and b) toluene. Two types of gas sensors is used based on the density of GaAs nanowires. Ga sensors based on high density nanowire arrays give a larger absolute resistive response, suggesting the importance of surface area increase as a result of density increase........... 128

List of Tables

Table 5-1 Growth conditions for GaAsP nanowires of varying PH_3 percentage flows. Flow percentage is PH_3 ranges 50% - 100% by keeping the total group-V flow, thus V/III ratio the same (~10). Growth time of GaAsP is adjusted to ensure fully grown nanowires.............. 97

Table 5-2 Incorporation coefficient values (k) for thin film growth experiments[125] (left column) is extrapolated to lower growth temperature ranges where nanowire growth is generally performed.. 106

Chapter 1: Introduction

1.1. Motivation

Electronic and photonic devices have fueled the technological advancements of the 20th century, and the control of materials properties through advanced processing techniques has been at the core of these achievements. Building electronic and photonic devices with smaller size, higher efficiency, and lower power consumption requires fundamental advances in semiconductors from the materials science and processing perspective. The state-of-the-art devices are currently fabricated starting with a planar morphology, where semiconductors are deposited as thin films followed by doping, etching, metallization, etc. to build the device structure. Adapting a non-planar morphology can address some of the aforementioned challenges by providing inherent advantages in physical processes such as confinement of electrons as well as scattering and absorption of light.

Semiconductor nanowires are defined as one-dimensional structures with diameters ranging from only a few nanometers up to tens of nanometers, and lengths in microns scale. Nanowires are typically grown or fabricated epitaxially on a substrate, and have a non-planar morphology. Nanowires combine the intrinsic properties of semiconductors with low dimensionality, which makes them suitable building blocks for electronic and optoelectronic applications,[1–3] such as solar cells,[4–8] light emitting diodes (LEDs),[9,10] and high electron mobility devices.[11,12]

The ability to grow semiconductor materials in one-dimensional nanowire morphology provides various advantages for electronic and optoelectronic applications. Continuous improvement of circuit performance has been historically achieved by downscaling the transistor

size. However, in planar field-effect transistors (FET), scaling of the gate length deteriorates electrostatic control of the conducting channel. Vertical nanowires enable a gate-all-around geometry in FET devices, in which a gate is wrapped around a nanowire channel. This structure would lead to superior electrostatic control of the conductivity in the FET channel and therefore could enable continued scaling of circuits.[2,13–16] Radial nanowire heterostructures facilitate band gap engineering along the diameter of nanowires, which can lead to improved transport properties due to confinement of carriers[17,18] and specifically high electron mobility due to confined electron gas[11] in core-shell nanowire structures.

In optoelectronic applications, one-dimensional morphology of nanowires can provide advantages in physical processes such as light generation, propagation, and amplification.[9,10,19] Light generation in LEDs may be improved as a result of lower defect densities in nanowires due to effective strain relaxation at the nanowire/substrate interface and larger surface area per footprint of quantum-well structures in the case of core-shell heterostructures.[20] Light propagation through nanowires can provide efficient extraction of light,[21,22] whereas periodic arrays can enhance light extraction due to directional emission of light.[23] In laser applications, semiconductor nanowires integrate both gain materials and lasing cavity, thus realizing compact photonic lasers.[24]

In particular, the geometry of nanowires has strong potential benefits for solar cells in terms of electrical and optical properties, strain relaxation, charge separation mechanisms, and a possibly decreased cost compared to planar wafer-based or thin film solar cells.[4,25–27] Light absorption in nanowire-based solar cells is improved due to reduced reflection compared to a planar morphology[28] and enhanced light trapping due to scattering in nanowire arrays.[29,30] In inorganic photovoltaic devices, nanowires can be exploited *via* three types of junctions as shown

in Figure 1.1: substrate junction, axial junction or radial (core-shell) junction. Substrate junctions occur when nanowire material or doping level is different than substrate. Axial junctions are aimed to be used for tandem solar cells, which stack up different bandgap materials along the nanowire growth direction to maximize the absorption of solar spectrum[5]. Radial junctions offer advantages by separating absorption and charge collection directions. In radial junctions, optical absorption occurs along the nanowire length, which is sufficiently long for absorption, and charge collection occurs radially along the diameter providing short collection lengths for free carriers[25]. Radial p-n[31] and p-i-n[32] junctions have been shown in GaAs nanowires with suitable doping.

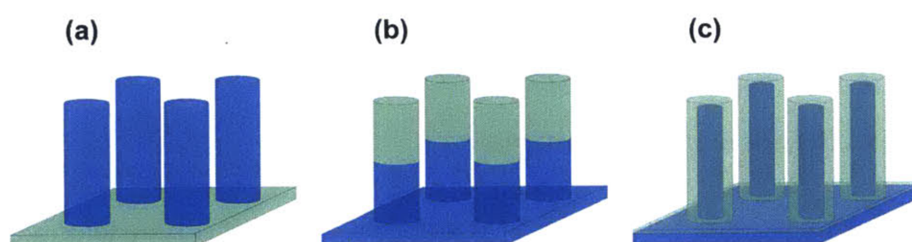

Figure 1.1 Nanowire heterostructures. a) Substrate junction where substrate and nanowire are composed of different materials or doping levels to create a junction at the interface. b) Axial heterostructure where nanowire composition or doping is altered along the nanowire length. c) Radial (core-shell) heterostructure where composition or doping levels are altered in radial direction. Green and blue colors represent different material composition and/or doping levels.

Whereas one-dimensional nanowire morphology can provide unique advantages in physical processes related to optoelectronic applications, the realization of these advantages can be achieved by using high quality nanowires with controlled areal density, nanowire diameter, and length. In particular, nanowire growth techniques impart the material quality of nanowires. A common method to grow bottom-up nanowires involves the use of foreign seed particles (*i.e.* Au) to facilitate one-dimensional growth.[33] However, atoms from the foreign seed particles may

incorporate into the nanowire and affect the material quality. Therefore, in this thesis, we investigate growth of III-V nanowires by self-seeded mechanism, where group-III element of the nanowire is utilized as a seed particle. This method eliminates foreign elements to be used as seed particles and thus circumvents the potential incorporation of foreign elements into the nanowire.

The research objectives of this thesis are to establish a framework on self-seeded III-V nanowire growth using Ga seed particles for GaAs nanowire growth, and achieve density and diameter control of nanowire arrays. Then, we extend the understanding of self-seeded growth into growth of ternary GaAsP nanowires and investigate the compositional control of ternary nanowires in self-seeded mechanism.

1.2. Nanowire fabrication techniques

Semiconductor nanowires can be fabricated using top-down methods by selectively etching a patterned planar material or can be grown on a substrate by vapor deposition techniques or solution processing techniques such as hydrothermal growth in the case of bottom-up approaches. In this section, we give an overview of these techniques for the growth of III-V nanowires and explain relevant growth mechanisms.

1.2.1 Top-down nanowire fabrication

Top-down approaches start with a planar layer with desired properties, such as composition and axial heterostructure, which is then etched away in defined positions to create nanowire morphology. The mask layer is defined by techniques such as optical lithography, electron beam lithography, nano-imprint lithography or anodic aluminum oxide.[34–37] Then, etching is performed by techniques such as wet etching, reactive ion etching and metal-assisted etching.[38–40] A

schematic of this process is shown in Figure 1.2a for top-down nanowire fabrication by metal-assisted etching. First, a metal layer with openings is created by lithography (top image) and then substrate under metal layer is etched by metal-assisted mechanism in solution (middle image) and nanowire morphology is obtained. Lastly, metal layer can be removed by etching to obtain nanowire array on the substrate. While this method can achieve highly uniform nanowire arrays with controlled size and length, it may introduce surface roughness due to etching process and has limited possibilities for development of axial heterostructures. GaAs nanowires by reactive ion etching[40] and Si nanowires by metal-assisted etching[38,41,42] have been realized by top-down approaches.

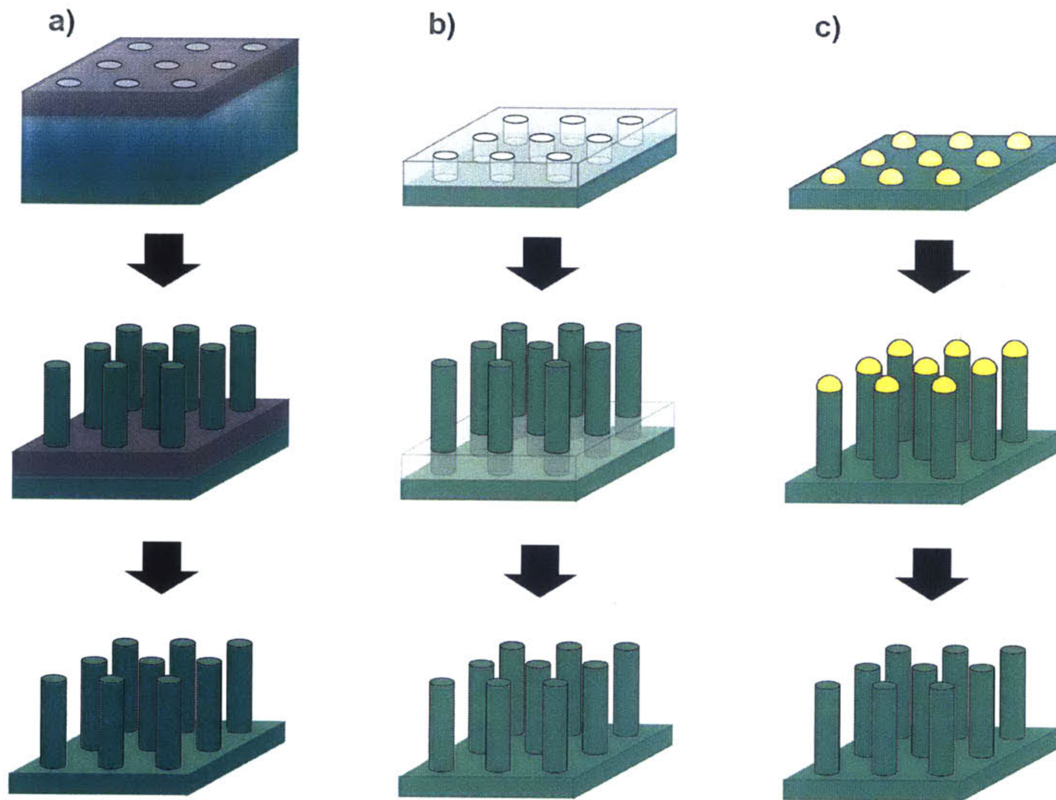

Figure 1.2 Nanowire fabrication and growth processes. a) Top-down nanowire fabrication by patterning (top) and subsequent etching (middle). After fabrication, pattern can be etched (bottom). b) Bottom-up nanowire growth by selective area epitaxy (SAE). First, a mask layer is patterned (top), then epitaxial growth only occurs in the openings of the mask layer (middle). Oxide mask layer can be removed by etching (bottom). c) Seed particle assisted nanowire growth. Seed particles are deposited on the substrate (top) and preferential decomposition of precursors and nucleation at the seed particle/nanowire interface leads to one-dimensional nanowire growth (middle). Seed particles can be removed by selective etching (bottom). Gray, green, transparent and yellow represent metal, nanowire material, oxide and seed metal, respectively.

1.2.2 Bottom-up nanowire growth

Bottom-up approaches are usually conducted *via* vapor phase epitaxy – growth of nanowires from vapor phase precursors – which include chemical vapor deposition (CVD)[43], metal-organic chemical vapor deposition (MOCVD)[44,45] and molecular beam epitaxy (MBE)[46]. In bottom-up approaches, common methods to grow III-V semiconductor nanowires are selective area epitaxy

(SAE) and particle-seeded growth (*i.e.* vapor-liquid-solid (VLS) method). Here, we first explain growth by SAE and then particle-seeded growth methods.

1.2.2.1 Selective area epitaxy

In SAE, substrate is covered with a mask layer where deposition of materials is minimal and deposition only occurs at the openings of the mask. Therefore, nanowire morphology can be achieved. This technique is schematically described in Figure 1.2b. First, a mask layer such as SiO_2[47] or SiN_x[48] is deposited and nanowire nucleation spots (openings) are patterned with lithography (top image), then one-directional nanowire growth is promoted in these openings (middle image) and the mask layer can be removed after growth (bottom image).

1.2.2.2 Particle-seeded nanowire growth mechanisms

Particle seeded growth mechanisms involve seed particles to achieve one-dimensional growth of nanowires, as shown in Figure 1.2c. A common method to grow one-dimensional nanowires involves the use of foreign seed particles;[33] in this approach, a seed particle alloys with the nanowire material(s) and nanowire nucleation occurs preferentially at the seed particle-nanowire interface. Commonly, nanowire growth is achieved using foreign metal seeds such as Au,[45,49,50] Ni,[51,52] Cu[53] or Pd,[54–56] which alloy with at least one of the nanowire constituent elements.

The vapor-liquid-solid (VLS) mechanism is a common growth method for vapor phase epitaxy of nanowires. It was first proposed by Wagner and Ellis in 1964 to explain the growth of Si whiskers.[33] This method is schematically shown in Figure 1.3 for the case of Si nanowire growth in CVD, in which Au is used as a collector particle. $SiCl_4$ or SiH_4 is introduced as the Si precursor, which decomposes to Si and alloys with the metal particle. Growth temperatures are above the eutectic temperature for Si-Au system, therefore the metal alloy particle becomes

liquid above certain Si content (*i.e.*16 at% Si at 550°C). The incorporation of Si results in supersaturation of the alloy particle, and Si solidifies preferentially at the particle-substrate interface as a monolayer.[57,58] These processes are described schematically in Figure 1.3a. The area of the seed particle-nanowire interface controls the nanowire diameter and one-dimensional growth occurs *via* layer-by-layer growth.[59–61]

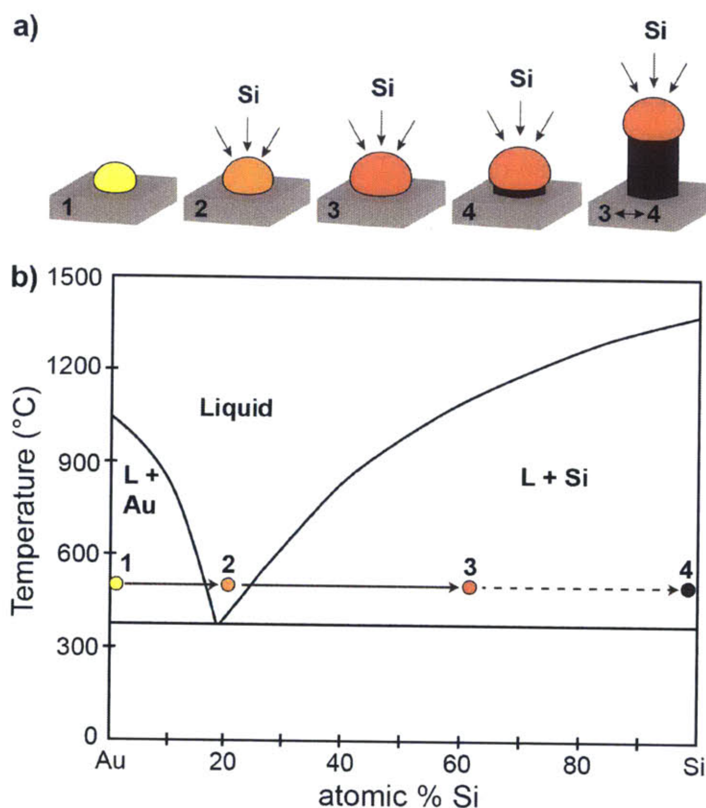

Figure 1.3 Vapor-liquid-solid (VLS) nanowire growth mechanism described for Si nanowire growth. a) Growth stages of VLS growth of Si nanowires and b) corresponding phase diagram. Solid gold particle (step 1) alloys with Si vapor and becomes a AuSi alloy. As Si content in the alloy particle increases, particle enters liquid phase (step 2) and becomes a supersaturated AuSi alloy (step 3), which drives formation of Si layer at the particle/substrate interface (step 4). Nanowire growth occurs as step 4 is repeated.

Growth of III-V nanowires by VLS is more complex than the elemental nanowire case, due to the necessity of incorporation of both elements for nanowire growth. Group-III materials

usually have sufficient solubility in Au; however, most group-V materials have very low solubility in Au[49,62]. Therefore, while group-III elements can diffuse through Au particle to reach particle-nanowire interface for solidification, the incorporation of group-V material should have another route. Experimental observations suggest that group-V material first reaches the triple-phase boundary (TPB), *i.e.* the vapor-liquid-solid interface, by surface diffusion on Au particle or on the nanowire; then diffuses along the particle-nanowire interface to form a III-V compound.[49,63]

During VLS growth of nanowires, sidewall deposition on nanowires and film formation on substrate may be observed, which are governed by a different mechanism than VLS, as shown in Figure 1.4. Some precursors decompose to their elemental sources during gas phase transport and may incorporate directly onto the nanowire sidewalls or substrate. The direct deposition of vapor phase decomposed precursor atoms on solid surfaces without going through liquid collector particle is referred as vapor-solid (VS) growth. VS growth is a thermally activated process and can be minimized and eliminated by lower growth temperatures.[45,64]

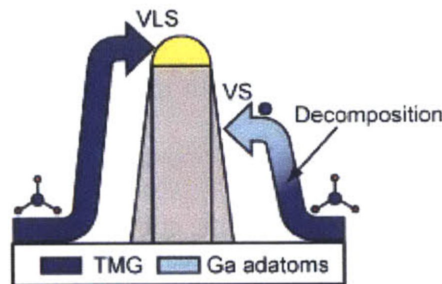

Figure 1.4 Effective growth mechanisms during particle-seeded GaAs nanowire growth. Ga precursor (TMGa) reaches the collector particle via surface diffusion and direct impingement, decomposes at the collector surface, and contributes vapor-liquid-solid (VLS) growth (left). Ga precursor decomposes during gas-phase transport and Ga ad-atoms reach the nanowire sidewalls and deposit on sidewalls via vapor-solid (VS) mechanism (right). (Image courtesy of SK Lim).

1.2.2.3 Self-seeded nanowire growth mechanism

The self-seeded nanowire growth is a subsection of particle-seeded method, where a collector particle is composed of elements constituting the wire instead of a foreign metal (*i.e.* in the self-seeded mechanism, GaAs nanowire growth would be referred as Ga-seeded growth, where the Ga particle would be collector particle on top of the nanowire). The self-seeded mechanism aims to eliminate the unintentional impurity incorporation to the nanowire by the metal collector particle during growth, and it is exploited in III-V nanowire growth on III-V substrates and Si substrates. Unintentional incorporation should be especially eliminated for the growth on Si substrates, since Au (common metal collector particle) has deep level traps in Si and could diffuse into the Si substrate.

Both foreign-seed particle VLS and SAE methods require a primary step – either deposition of seed (collector) particle or depositing mask layer and patterning openings for nanowire nucleation and growth. In self-assisted growth, these pre-steps are usually not necessary, because collector particle is a group-III material, which can be deposited *in-situ* prior to growth.[65] Even in the conditions that it is not deposited *in situ*, group-III rich flows may result in droplet formation of group-III material during growth due to the ratio of precursors and volatility of group-V material.[66] However, it is worth noting that some groups deposit a very thin layer of SiO_x or SiO_2 to help with immobilization of the collector particles.[66,67]

Although VLS method with foreign metal seed particles can be used to control nanowire morphology,[68,69] incorporation of metal atoms into nanowires during the growth and/or post-processing can affect the nanowire optoelectronic properties.[70–72] Incorporation of the seed atoms depends on the exact materials system, such as the combination of seed particle and nanowire elements, and on the growth conditions including temperature and growth rate. Recent electron

microscopy and electron tomography studies have provided direct visualization of seed atoms incorporated into nanowires for Au-seeded[73] and Al-seeded[74] Si nanowires as well as Au-seeded GaAs nanowires.[75] Furthermore, the presence of foreign metal seeds may influence the growth of more complex nanowire structures. For example, in the case of core-shell nanowires, Au incorporation into the nanowire during a high-temperature shell deposition has been observed affecting n-type shell doping of GaAs nanowires.[76] Finally, for many optoelectronic devices, including nanowire-based solar cells, removal of metal seed particles may be necessary prior to device fabrication to reduce reflection and eliminate non-radiative recombination centers.[8,77]

Self-seeded growth, in which one of the nanowire constituent elements is used as the seed particle, circumvents the issue of possible contamination by eliminating the use of foreign seeds. In the case of III-V nanowires, the group-III elements form seed droplets on the substrate and drive the nanowire growth. Self-seeded nanowire growth has been demonstrated in several III-V material systems, including InAs,[66,78,79] InP,[65,80] GaAs[67,81] and GaP.[82] To date, the self-seeded growth of GaAs nanowire arrays has been achieved by MBE.

Some early reports on self-assisted nanowire growth include growth of In-assisted InP by Novotny and Yu in 2005[80] and growth of In-assisted In(As)P nanowires in 2006 by Mattila *et al.*[65] According to the proposed nucleation and growth mechanism of self-assisted III-V nanowire growth (Fig. 5); group-III material forms collector particles on the substrate and nanowire growth occurs by solidification at the collector particle-nanowire interface, similar to Au-assisted VLS mechanism.[66] Some studies have discussed the necessity of a thin SiO_2 layer (10Å – 6nm) for self-assisted growth. The question becomes: how does the group-III particle form and what is the role of the very thin silicon oxide layer? Mandl *et al.* asserted that the main role of the SiO_x layer is to immobilize the collector particles in well-defined areas.[66] Morral *et*

al. suggested that interaction of reactive gallium with SiO_2 pinholes induces formation of nanocraters on SiO_2 layer during pre-growth annealing, which are favorable areas for group-III droplet formation. Other studies that use Si substrates etch the native oxide prior to growth and still observe successful nanowire growth.[82,83] Currently, there is not a consensus on the role of oxide layer, although most of the studies suggest that nanowire growth occurs *via* a VLS like mechanism with group-III collector particle. After growth, depending on cooling conditions, the particle may be observed at the top of the nanowire.[67,81,84] Some studies do not observe the particle, and it is suggested that during cooling, existence of group-V material in the reactor results in crystallization of nanowire tip.[66]

Self-assisted growth requires careful optimization of the growth parameters, such as temperature, flow rates of precursors and relative ratio of group-V and group-III precursor flow rates (V/III ratio). Temperature affects the growth rate, decomposition of precursors, lateral growth, desorption rate and diffusion length of adatoms in nanowire growth[81]. Usually, there's a limited temperature window in which nanowires can be grown[64,84,85]. Below that temperature window, decomposition of precursors may not be sufficient for growth and/or mobility of adatoms might be small and nanowire growth is not observed. Above certain temperatures, adatoms do not stick to the substrate (they desorb before clustering)[85]. Flow rates are crucial because they determine the growth rate, along with temperature. V/III ratio is also very important, especially in self-assisted growth, as group-III rich conditions have been necessary for growth of self-assisted nanowires[81,86].

Self-assisted growth is a dynamic process as the collector particle consists of group-III material and it is consumed during growth. Growth system would reach the steady state conditions when the incorporation and extraction rates of group-III material in the collector

particle are equal. In the case of *in situ* deposited group-III particles, providing excess group-V material can result in consumption of collector particle (group-III element) gradually, thus collector particle volume decreases and nanowire diameter gets smaller along the length resulting in tapered nanowires where bottom of nanowire is wider than the top of nanowire. This has been observed for In-assisted InP nanowires grown by MOCVD[64]. The opposite scenario occurs with excess group-III material during growth, when growth is group-V limited as observed for Ga-assisted GaAs nanowires grown by MBE. Excess group-III material accumulates in collector particle, which results in volume expansion in the collector particle, and inverse tapered nanowires are observed[81]. Thus tapering in self-assisted mechanism can happen as a result of VLS growth and careful optimization of growth parameters should be done to fabricate non-tapered nanowires.

1.3. Outline of the thesis

This thesis is organized as follows: Chapter 1 motivates the study of nanowires and introduces the topics of fabrication of nanowires using various top-down and bottom-up methods. Growth mechanism of particle-seeded growth (vapor-liquid-solid mechanism) is described in detail. In Chapter 2, we describe the methods used for the growth and characterization of III-V nanowires. Growth is performed in metal organic chemical vapor deposition (MOCVD). Structure, morphology, optical properties of nanowires was determined with various electron microscopy and x-ray techniques. In Chapter 3, we discuss self-seeded growth of GaAs nanowires by MOCVD and explain the nucleation and growth mechanisms. Two-step growth with *in* situ deposition of Ga seed particles followed by GaAs nanowire growth has been crucial in achieving reproducible high vertical yield nanowire arrays. In Chapter 4, we build on self-seeded GaAs nanowire growth and explore the density and diameter control of

nanowires. We use parameters such as seed deposition temperature and substrate orientation to induce control of seed formation kinetics, which controls the nanowire density and diameter kinetics. In Chapter 5, we extend the binary nanowire growth into ternary material system – GaAsP. Ga-seeded GaAsP nanowires are grown in a similar method to GaAs nanowires and more importantly we establish control of composition in GaAsP nanowires. Various techniques such as energy dispersive x-ray spectroscopy, reciprocal space mapping and cathodoluminescence are used to investigate the structure and composition of nanowires. In Chapter 6, we conclude our work and describe potential future work that can be built upon this knowledge we contribute to the field.

Chapter 2: Experimental methods

In this chapter, we introduce the experimental techniques used in this work to study self-seeded III-V nanowire growth. First, self-seeded III-V binary and ternary nanowire growth by metal-organic chemical vapor deposition (MOCVD) is described. Second, characterization of morphology, structure, composition, and strain of nanowires using scanning electron microscopy (SEM), transmission electron microscopy (TEM), energy dispersive x-ray spectroscopy (EDS), and reciprocal space mapping (RSM) by x-ray diffraction (XRD) are presented. Lastly, optical characterization of nanowires using cathodoluminescence (CL) in SEM is described.

2.1. Growth of self-seeded III-V nanowire by MOCVD

III-V binary and ternary nanowires (*i.e.* GaAs, GaAsP) were grown by MOCVD using Ga (group-III element) as the seed particle to drive one-dimensional growth. Details of the experimental setup, substrate preparation, and self-seeded nanowire growth conditions are described below.

2.1.1 Metal-organic chemical vapor deposition

MOCVD is a widely utilized technique for epitaxial growth of single crystalline semiconductor nanowires on a range of substrates. MOCVD is commonly used in industry for growths of thin films as large-scale wafers can be used and high growth rates are obtained at low or atmospheric pressures. Therefore, research products such as controlled self-seeded nanowire growth can be moved up to industrial scale once realization of desired structures is achieved at smaller scale.

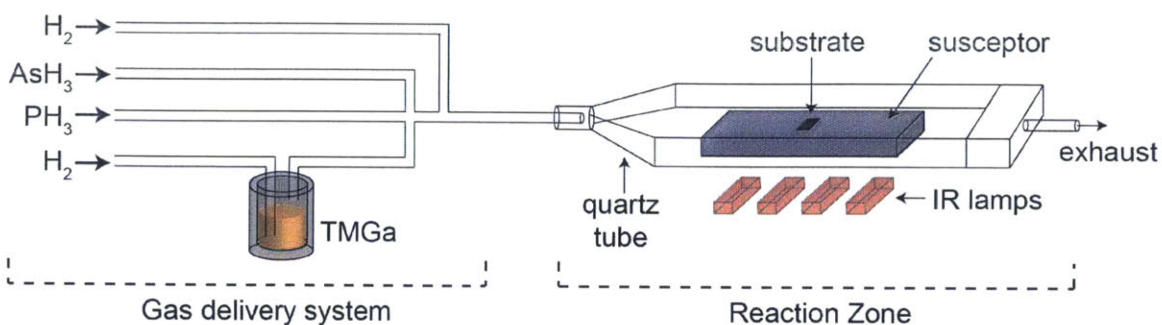

Figure 2.1 Schematic of the MOCVD setup used in this work. Group-III precursor is trimethylgallium (TMGa) and group-V precursors are arsine (AsH_3) and phosphine (PH_3). Precursors and carrier gas (H_2) are delivered to the reaction zone where nanowire growth occurs. Reaction zone is heated to the desired growth temperatures by heating the susceptor using IR lamps.

III-V nanowires were grown by a Thomas Swan CS62820 cold-walled horizontal-flow MOCVD operated at atmospheric pressure. MOCVD can be described in two parts: (1) gas delivery system and (2) reaction zone (Figure 2.1). Precursors and carrier gas are delivered to the reaction zone where nanowire growth occurs. The precursors used for III-V nanowire growth in this thesis are trimethylgallium (TMGa) as group-III precursor and arsine (AsH_3) and phosphine (PH_3) as group-V precursors. Mass flow controllers (MFC) were used for precise control of flow rates of gases.

Metal-organic group-III precursors are in a liquid phase and stored in bubblers. Temperature of the bubbler determines vapor pressure, whereas carrier gas flow rate through the bubbler determines the effective flow rate of group-III precursor vapors. TMGa flow rates reported in the thesis are effective flow rates that were calculated from the vapor pressure and carrier gas flow rates. The TMGa bubbler temperature was kept at 1°C. Group-V precursors have high vapor pressures, therefore can be delivered as gas precursors from tanks (217 psi for AsH_3 and 507 psi for PH_3 at 20°C)[87] and gas delivery lines are equipped with pressure regulators and MFCs.

$TMGa$ and AsH_3 precursors were diluted to enable a greater range of flow rates during growth. In addition to precursors, a carrier gas (H_2 or N_2) was delivered to the reaction zone to stabilize the flow of the gas mixture.

Reaction zone consists of a graphite susceptor that was locally heated by infrared emission from halogen lamps. The quartz tube that encapsulates the reaction zone is at a lower temperature compared to the susceptor. This cold-walled configuration enables reaction and deposition of materials on substrates that are heated through the susceptor, and minimizes deposition on quartz tube walls. Finally, all gases flow to exhaust where filters and scrubbers treat unreacted precursors.

2.1.2 Self-seeded III-V binary GaAs nanowire growth

This section describes details of the experimental procedure used for the growth of self-seeded GaAs nanowire.

Substrate cleaning. Prior to growth, GaAs (111)B, (111)A, and (110) substrates were cleaned by sonication in acetone, methanol, and deionized water for 5 min each to remove any organic contamination. After sonication, substrates were dried with compressed air and stored in MOCVD glovebox under nitrogen environment.

Nanowire growth. Substrates were loaded into the MOCVD reactor. During heating, growth, and cooling down to 350°C, H_2 carrier gas was flown at 15 slpm (standard liters per minute), and the carrier gas was then switched to N_2 during cooling below 350°C. The growth procedure started with annealing at 600°C for 10 min under H_2 flow. Following annealing, Ga seed deposition was performed by flowing TMGa for one minute at temperatures between 500°C – 600°C with an effective flow rate of 1.67 sccm (standard cubic centimeters per minute), except when noted otherwise. After Ga seed deposition, substrates were cooled to the growth

temperature under hydrogen, and the nanowire growth was performed by flowing TMGa and AsH_3 between 420°C – 435°C. Effective flow rates of precursors during growth range between 0.36 – 1.67 sccm for TMGa and 3.35 – 18.6 sccm for AsH_3, except noted otherwise. At the end of the growth, both precursors were turned off and the chamber was cooled under hydrogen ambient. The growth procedure is shown schematically in Figure 2.2. Experiments in section 4.2 and section 4.3 (density and diameter control by seed deposition temperature and surface orientation) were cooled under AsH_3 and H_2 flow until 350°C.

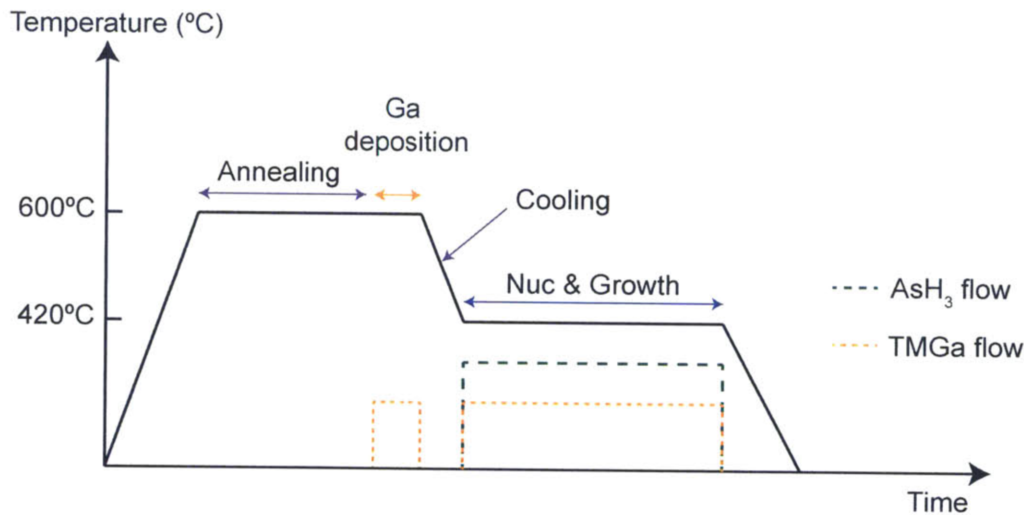

Figure 2.2 Growth procedure schematic of a typical self-seeded GaAs nanowire growth. Temperature profile is given by solid line and flow rates are represented by dashed lines.

2.1.3 Self-seeded III-V ternary GaAsP nanowire growth

Self-seeded growth of ternary GaAsP nanowires followed a similar procedure to the growth of binary GaAs nanowires described above. In general, ternary nanowires were grown at higher growth temperatures (450°C – 500°C) compared to the growth of binary nanowires (420°C – 435°C) to increase decomposition percentage of PH_3 and AsH_3 precursors. Also, AsH_3 was flown along with H_2 carrier gas during heating, some part of annealing, and nanowires were

cooled under AsH_3, PH_3 and H_2 gas flow until 350°C. While there was not substantial effect of group-V precursor flow during heating, cooling under group-V precursor flow was performed to follow general semiconductor processing practice.

Substrate cleaning. Prior to growth, GaAs (111)B substrates were cleaned by sonication in acetone, methanol, and deionized water for 5 min each to remove any organic contamination. After sonication, substrates were dried with compressed air and stored in MOCVD glovebox under nitrogen environment.

Nanowire growth. Substrates were loaded into the MOCVD reactor. Throughout the heating, growth and cooling until 350°C, H_2 carrier gas was flown at 15 slpm, then carrier gas was switched to N_2 during cooling below 350°C. Growth procedure started with AsH_3 flow (3.35 sccm) above 350°C during heating. When reached to 600°C, annealing step was performed for a total duration of 10 min, with gas flows of AsH_3 and H_2 during first 7 min and gas flow of only H_2 during last 3 min. The last 3 minutes under H_2 also serve as a purge step between annealing with AsH_3 and Ga seed deposition. Immediately after annealing, Ga seed deposition was performed by flowing TMGa at 600°C with an effective flow rate of 1.67 sccm for one minute. After Ga seed deposition, substrates were cooled to the growth temperature (450°C – 500°C) under hydrogen, and the nanowire growth was performed in two steps. First, GaAs stem growth was performed for 1.5 – 2 min by flowing TMGa and AsH_3 at 1.67 sccm and 8.49 sccm, respectively (V/III = 5). Second, GaAsP nanowire growth was performed for 3.5 – 10 min with TMGa flow at 1.67 sccm and AsH_3 and PH_3 total flow at 16.7 sccm (V/III=10). The percentage of AsH_3 and PH_3 was varied between 50% PH_3 – 100% PH_3 by keeping the total group-V flow at 16.7 sccm. After GaAsP nanowire growth, TMGa was turned off and the chamber was cooled

under AsH_3 PH_3 and H_2 flow until 350C. Growth procedure is shown schematically in Figure 2.3.

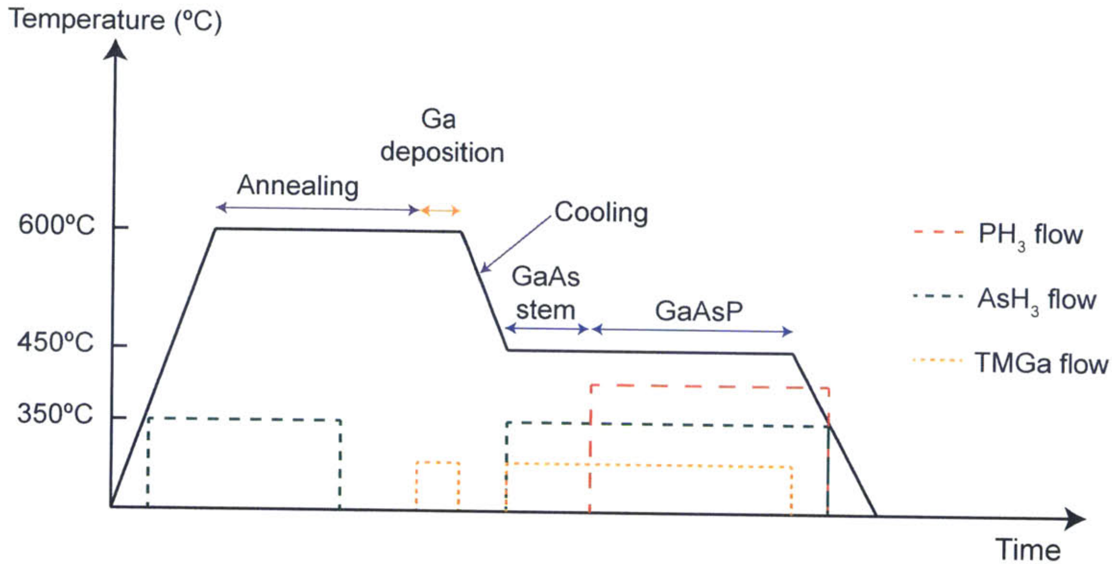

Figure 2.3 Growth procedure schematic of a typical self-seeded GaAsP nanowire growth. Temperature profile is given by solid line and flow rates are represented by dashed lines.

2.2. Structural and compositional characterization

To study the structure and composition of nanowires, we utilized electron microscopy and x-ray diffraction techniques. The high resolution that can be achieved with electron microscopy makes it a primary tool to study morphology and structure of nanoscale materials, including nanowires. Furthermore, x-ray diffraction (XRD) is one of the most common tools to investigate the crystal structure of thin films and we have applied this technique to investigate nanowire crystal structure, which gives information about composition and strain in ternary nanowire, and assessed the applicability of XRD to the study of nanowires.

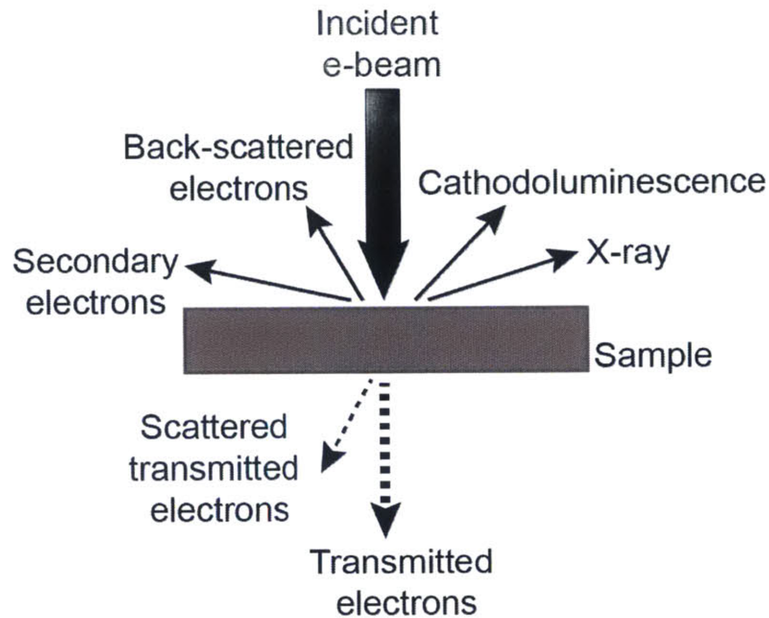

Figure 2.4 Various signal produced upon interaction of high-energy electron beam with a sample. Using these signals, morphology, structure, chemical composition and optical properties of the sample can be investigated.

Electron microscopy is a versatile tool due to various types of signals produced upon irradiation of a sample with a high-energy electron beam. Morphology and crystal structure can be investigated using secondary electrons, back-scattered electrons, scattered transmitted electrons and transmitted electrons. Compositional analysis can be performed using characteristic x-rays of elements. Optical properties such as band gap can be determined using cathodoluminescence signal.

2.2.1 Scanning electron microscopy (SEM): morphology, density, diameter and length of nanowires

Morphological properties of nanowire arrays were investigated using scanning electron microscopy (SEM). Using SEM images, we determine morphology, density of nanowire arrays and diameter-length of single nanowires.

In electron microscopy, a beam of accelerated electrons is focused on a sample using electromagnetic lenses. Upon interaction of electron beam with the sample, various signals are produced. One of these signals is secondary electron signal, which are the electrons that have energy less than 50 eV (Figure 2.4). Among the secondary electrons generated as a result of interaction of the electron beam with the sample, only secondary electrons that are close to sample surface can escape. Furthermore, yield and detection of secondary electrons is sensitive to the sample topography such that larger number of secondary electrons escape from discontinuous *vs.* flat surfaces. Therefore, we utilized secondary electron imaging to assess the morphology of nanowire arrays on substrate.

SEMs used in this study were FEI Helios NanoLab 600 Dual Beam Microscope and Zeiss Merlin High Resolution SEM, both operated at accelerating voltage of 5kV. Images were collected at top-view and 45° tilt conditions. The areal density and homogeneity was obtained from top-view images, whereas diameter and length of nanowires were measured from 45° tilted SEM images. Sample preparation in our case was not required for SEM imaging because as-grown nanowire arrays on substrate can be directly imaged.

2.2.2 Transmission electron microscopy (TEM): structure of nanowires

When a highly accelerated electron beam irradiates a thin sample, transmitted electron beam conveys information about the crystal structure of the sample. In TEM, we use transmitted and diffracted electrons to form an image and generate diffraction pattern of the crystal.

Nanowire structure was investigated using JEOL 2010F TEM operated at 200 kV. Bright field imaging, high-resolution imaging, selected area diffraction and energy dispersive x-ray spectroscopy (EDS) are the different modes utilized to investigate nanowire structure. EDS is described in the next section in more detail.

Sample preparation. Two types of TEM samples were prepared either by mechanically removing nanowires from the substrate or by polishing nanowires on the substrate using focused ion beam (FIB). First, nanowires were removed from the growth substrate by placing a carbon lacey TEM grid upside-down onto the substrate and gently sliding it. The nanowires broke from the substrate and were transferred to the grid horizontally. Because nanowire diameter varies between hundreds of nanometers to tens of nanometers, the thickness of the sample is appropriate for TEM imaging without further thinning. Second, cross-sectional TEM samples were prepared using an FIB lift-out method. Lift-out was performed in FEI Helios 600 focused ion beam (FIB) microscope using the following procedure: nanowire arrays were loaded into the microscope and a protective layer of platinum was deposited on the region of interest using first electron beam and then Ga ion beam. Then, Ga ion was used to etch trenches around the region of interest to create a lamella. A high precision probe was inserted and the lamella was first welded to a probe and then separated from the substrate. Lifted-out lamella was transferred to a TEM grid and Ga ion beam etching was performed at 30 kV to thin down the lamella. Lastly, sample was thinned with 5 kV Ga ions to remove amorphous regions that are produced during high-energy etching. With this method, we have produced TEM samples used to study the interface of substrate and nanowire base.

2.2.3 Energy dispersive x-ray spectroscopy (EDS): nanowire composition

Characteristic x-rays can be utilized to identify elements present in the sample and quantify its composition. When a high-energy electron beam ejects one of the inner-shell electrons of an atom, it leaves a hole that is filled with an outer-shell electron. During the process, the difference between outer-shell and inner-shell energies may be emitted as a photon, which is referred as characteristic x-ray (Figure 2.4); or this energy can be transferred to another outer shell electron

causing it to be ejected from the atom, where ejected electron is known as Auger electron. The probability of x-ray emission instead of Auger electron emission increases with increasing atomic number of elements.[88] Since inner-shell and outer-shell energies are specific for every element, emitted x-rays energies can be associated with an element. The spectra of x-ray counts with respect to energy can be used to identify the elements of the sample and quantify the composition (Figure 2.5).

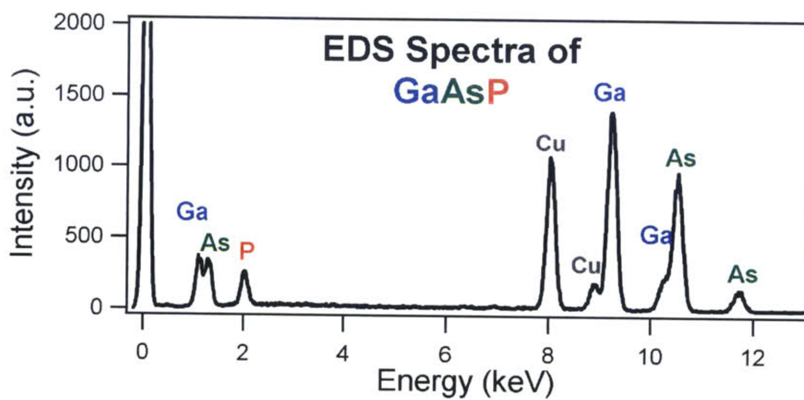

Figure 2.5 EDS spectrum of GaAsP nanowire showing characteristic x-ray energies of Ga, As, P elements emerging from nanowire and Cu element emerging from TEM grid.

In this work, we combined scanning transmission electron microscopy (STEM) imaging with EDS measurements to determine the composition of III-V ternary nanowires. JEOL 2010F TEM can be operated in STEM mode where incident electron beam is converged to have a probe size less than 1 nm, instead of the parallel electron beam used in TEM imaging. When EDS is coupled with STEM, converged beam is scanned over the sample to collect x-rays from specific areas. This way, x-ray spectra can be obtained as a point measurement, linescans or elemental maps of a region. EDS analysis is performed using x-rays with energies from 0-20 keV. In GaAsP, we use the K-series of characteristic x-rays (K_α and K_β at 9.225-9.252 keV and 10.260-10.264 keV for Ga, 10.508-10.544 keV and 11.720-11.736 keV for As, and 2.013-2.014 keV and 2.134 keV for P, where the range denotes the peaks for α_1 and α_2 or β_1 and β_2 transitions. In EDS

spectra, α_1 and α_2 transitions and β_1 and β_2 transitions overlap and show a single peak. The energy range should be above the highest characteristic x-ray energy of the elements of interest, in our case arsenic (characteristic x-rays of arsenic, K_α and K_β are at 10.5 keV and 11.7 keV,[89] as shown in Figure 2.5).

We have performed three types of analysis using EDS-STEM: point spectra, line spectra and elemental maps. Each of this analysis gives information about the composition of the nanowires; however, the advantage of each analysis varies such that point spectra can be quantified directly and reliably, line spectra can show the distribution of elemental x-ray counts with high precision whereas elemental maps can show the distribution of elements in an area with lower count rates per pixel compared to line spectra. Point spectrum is collected when the electron beam is fixed on a single spot and x-rays are collected for a certain time. In general, at least 1000 counts were collected for reliable statistics and quantification. Collection and quantification of EDS spectra was performed by INCA software. An important advantage of the point spectrum analysis is that INCA software takes into account thickness and density of the sample to accurately quantify the spectrum. In our analysis, point spectra were taken from the nanowire center such that the thickness is estimated as the nanowire diameter. The density was estimated from the densities of GaAs (5.32 g/cm^3) and GaP (4.14 g/cm^3). An important point in quantification is the relative amount of group III (*i.e.* Ga) and group V (*i.e.* As and P) elements – where we expect Ga atomic percentage to be 50%. When EDS quantification gives 50±2% for Ga atomic percentage, the quantification is regarded as accurate. The composition values of nanowires were calculated from EDS point spectra. For each nanowire, 4-10 point spectra were quantified and averaged to give the average composition of the nanowire. This was repeated for multiple nanowires (5-10)

and an average composition and standard deviation for a specific nanowire growth was obtained by averaging compositions of multiple nanowires.

EDS linescans were collected to analyze the distribution of phosphorus along the nanowire diameter or length. This gives information about the homogeneity of P incorporation. It should be noted that, due to hexagonal shape of nanowire cross section and tapered morphology of nanowire length, the thickness of x-ray collection changes during line-scan along diameter and length, respectively. Furthermore, raw data of linescans report the x-ray intensity with respect to position. However, x-ray intensity of an element can be affected by preferential absorption of x-rays from one of the elements in the sample that can occur under three conditions; i) when sample is too thick, ii) if an element of the sample has characteristic x-ray energy less than ~1-2 keV, or iii) when characteristic x-ray energies of elements differ in energy by > 5-10 keV.[88] In linescans of GaAsP nanowires, the changes in thickness could affect the amount of x-ray absorption by the sample, and when that is the case, characteristic x-rays of P are likely to be preferentially absorbed more than Ga and As due to low energy of x-ray emission of P (at 2.01-2.14 keV). Therefore, we use the raw data of linescans to observe the trends of x-ray intensity rather than for quantification purposes.

Elemental maps were collected to analyze possible segregation of elements. However, it should be noted that to attain a reliable elemental map, one should collect sufficient number of x-ray counts. While this can be achieved by increased collection time, the spatial resolution of the map could be affected by sample drift over time. Therefore, this technique was used with caution and we used it to determine possible major compositional segregation in the nanowire.

2.2.4 High resolution x-ray diffraction (XRD) reciprocal space mapping (RSM) to determine strain and composition

In this section, the method of using x-ray diffraction for reciprocal space mapping (RSM) is described. Also, the equations to calculate composition and relaxation based on RSM are given.

RSM was collected using Bruker D8 high resolution XRD with incident wavelength of Cu $K_{\alpha 1}$ (λ=1.540562 Å) equipped with Bruker Lynxeye linear array detector with an angular resolution of 0.014°. We performed two-dimensional 2theta-relative omega scans for various omega values. RSM was analyzed by using DIFFRACplus LEPTOS 7 software. These two-dimensional maps show the diffraction intensity of crystal planes of interest. The position of crystal plane peaks in reciprocal space contains information about lattice mismatch in lateral and normal directions. Then, lattice mismatch between substrate and nanowires is used to calculate composition and relaxation as described below.

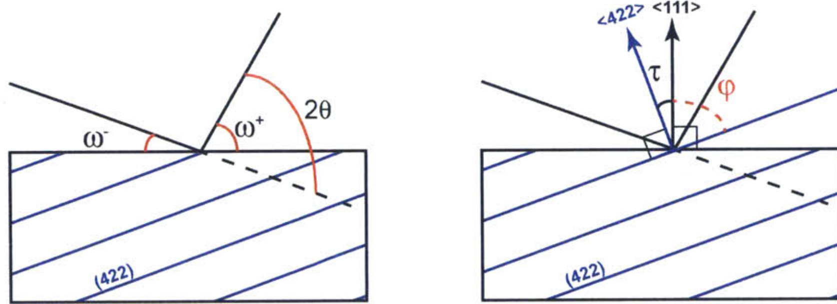

Figure 2.6 Schematic of the x-ray diffraction setup for reciprocal space mapping of (422) plane of a sample with <111> normal. X-ray beam incidence angle (ω^-), exit angle (ω^+) total scattering angle (2θ), angle between the surface normal and scattering vector (τ), and angle between surface normal and scattering plane (φ) are shown.

The LEPTOS software converts 2theta – omega maps to $q_x - q_z$ maps using following relations:[90]

$$q_x = -2K \sin\theta_{S,N} \sin\tau_{S,N}$$

$$q_z = 2K \sin \theta_{S,N} \cos \tau_{S,N}$$

where K is the wave vector of the incident x-ray beam, $\theta_{S,N}$ are Bragg angles for the substrate and nanowire, respectively, $\tau_{S,N}$ are the angles between the surface normal and the scattering vectors (Figure 2.6), respectively, defined as:

$$\theta_{S,N} = \frac{\omega^{+}_{S,N} + \omega^{-}_{S,N}}{2}$$

$$\tau_{S,N} = \frac{\omega^{+}_{S,N} - \omega^{-}_{S,N}}{2}$$

The lateral and normal lattice mismatch can be calculated as following:

$$\frac{\Delta a}{a} = \frac{\sin \theta_S}{\sin \theta_N} \frac{\cos \varphi_S}{\cos \varphi_N} - 1$$

$$\frac{\Delta c}{c} = \frac{\sin \theta_S}{\sin \theta_N} \frac{\sin \varphi_S}{\sin \varphi_N} - 1$$

where $\varphi_{S,N} = \frac{\pi}{2} - \tau_{S,N}$.

Combining the equations above, the relationship of mismatch to q_x and q_z becomes:

$$\frac{\Delta a}{a} = \frac{q_x^S - q_x^L}{q_x^L}$$

$$\frac{\Delta c}{c} = \frac{q_z^S - q_z^L}{q_z^L}$$

Using the mismatch values, the strained nanowire lattice parameters can be found from lattice constant of substrate, a_S:

$$a_N = a_S\left(\frac{\Delta a}{a} + 1\right)$$

$$c_N = a_S\left(\frac{\Delta c}{c} + 1\right)$$

Even though GaAsP nanowire is a cubic material, due to biaxial strain, it is expected to undergo a transformation to a rhombohedral unit cell (or a pseudo-hexagonal unit cell when

viewed along <111> direction) near the interface. The relaxed nanowire would have only one lattice constant, $a^R{}_N$, because of its cubic crystal structure.

The lattice mismatch exerts a biaxial isotropic in-plane strain. From anisotropic elastic theory, biaxial strain with zero stress perpendicular to the interface and no mismatch shear strains at the interface, strain tensor components along lateral and normal directions are related via Poisson's ratio of the material for a cubic material:

$$\varepsilon_{zz} = -\frac{2v}{1-v}\varepsilon_{xx}$$

This relationship is valid for cubic or tetragonal materials, and Poisson ratio along normal direction of the biaxial strain should be used. ε_{xx} and ε_{zz} correspond to strain along lateral and normal directions, respectively. For growth direction of <111>, $GaAs_{1-x}P_x$ Poisson ratio is calculated by using Poisson ratio along <111> direction for GaAs and GaP via Vegard's law.

$$v_{GaAsP}(x) = (1-x)v_{GaAs} + xv_{GaP}$$

$$\varepsilon_{xx} = \frac{a_N - a_N^R}{a_N^R}$$

$$\varepsilon_{zz} = \frac{c_N - a_N^R}{a_N^R}$$

The lattice constants of the strained nanowire, a_N and c_N were calculated using RSM. To find the strain and relaxed composition, equations above can be solved numerically and composition, x, can be determined.

Relaxation of nanowire is calculated using lateral lattice constant difference between strained nanowire and relaxed state with respect to the substrate lattice constant.

$$R = \frac{a_N - a_S}{a_N^R - a_S}$$

The (422) reflection with grazing incidence was selected for several reasons. Firstly, to determine the strain and composition of a layer together, asymmetrical reflections should be considered. An asymmetrical reflection is a plane reflection that is not perpendicular to the growth direction (for example (333) reflection is a symmetrical reflection for <111> growth direction). Symmetrical reflections can only be used to determine lattice constant along the growth direction, but do not contain information about the strain state. However, an asymmetrical reflection of a plane contains both the lattice constant and relaxation information. An asymmetrical reflection can be collected by grazing incidence or grazing exit angles. Grazing incidence denotes that the incidence of x-ray beam is a small angle. This is especially useful for a thin layer sample or a low-density sample (*i.e.* nanowire array) because the thickness of the irradiated sample would be small, therefore the diffraction intensity from the surface layer (*i.e.* nanowire) and substrate would be comparable. Otherwise, substrate diffraction intensity may dominate the data.

2.3. Optical characterization of nanowires using cathodoluminescence (CL)

Optical properties of nanowires were investigated using cathodoluminescence coupled with SEM (CL-SEM). The process of light emission from sample due to electron beam irradiation is called cathodoluminescence. When a semiconductor sample is irradiated with an electron beam, electrons in the valence band are excited to conduction band and an electron-hole pair is created. This electron-hole pair undergoes radiative recombination in direct band gap semiconductors and the energy difference between the conduction band and the valence band is emitted as a photon. The energy of the photon corresponds to the band gap of the material at room temperature and this type of emission is called band edge emission. Therefore CL gives information about the

band gap of the material. For ternary semiconductors, the band gap is dependent on the composition; therefore indirect information about composition can be achieved using CL-SEM.

Measurements were performed in SEM operated with 15 kV accelerating voltage and 1.3 nA beam current. Different types of measurements were carried out to determine the band gap of nanowires. Panchromatic CL (PanCL) maps were collected to obtain the map of light emission from the sample to determine radiative recombination regions. Monochromatic CL (monoCL) maps were collected to map the regions with a specific emission wavelength. Apart from the emission maps, point spectra were collected both at room temperature and liquid nitrogen temperature.

Chapter 3: Binary material system - GaAs nanowire growth

This chapter demonstrates the growth of self-seeded binary GaAs nanowires using metal-organic chemical vapor deposition (MOCVD). Two-step growth has been crucial to achieve Ga-seeded GaAs nanowires, where *in situ* deposition of Ga droplets is followed by growth of GaAs nanowires. Single crystalline nanowires exhibit epitaxial relationship with the substrate and have a tapered morphology – nanowire diameter gets smaller towards the tip of nanowire. Based on structural investigations of the nanowire/substrate interface and nanowire tapering, a growth model of self-seeded growth is developed. Ga-seeded GaAs growth establishes important groundwork for the growth of III-V nanowires and the knowledge developed in this section can be transferred to other binary and ternary III-V materials systems.

3.1. Introduction

Among various methods used for growth of nanowires, a versatile and common approach is vapor-liquid-solid (VLS) growth, described in more details in 0. In short, in the VLS mechanism a seed particle mediates one-dimensional nanowire growth by acting as a collector of nanowire precursors and layers of solid nanowire preferentially nucleate and grow at the particle - nanowire interface. For III-V nanowire growth, VLS method has been realized using a variety of seed particles including foreign metal seeds such as Au,[45,49,50] Ni,[51,52] Cu[53] or Pd,[54–56] . While VLS method with foreign metal seed particles has been a common choice for nanowire growth,

incorporation of metal atoms into nanowires during the growth[75] and/or post-processing can affect the nanowire optoelectronic properties[70–72] as detailed in the Introduction.

Self-seeded growth, in which one of the nanowire constituent elements is used as the seed particle, circumvents the issue of possible contamination by eliminating the use of foreign seeds. During growth of III-V nanowires, the group-III elements (i.e. Ga, Al, In) form seed droplets on the substrate and drive the nanowire growth. Self-seeded nanowire growth has been demonstrated in several III-V material systems, including InAs,[66,78,79] InP,[65,80] GaAs[67,81] and GaP.[82] Self-seeded growth of GaAs nanowire arrays has been demonstrated by molecular beam epitaxy (MBE); however, we have achieved Ga-seeded GaAs nanowire growth using metal-organic chemical vapor deposition (MOCVD), where higher growth rates and scalability can be achieved.

In this work, we focus on GaAs nanowire growth due to technologically appealing properties of GaAs material system. The intrinsic properties of GaAs, including a direct bandgap of 1.42 eV – suitable for realization of solar cells with theoretical efficiencies up to 32.8%[91] – and a high electron mobility (8800 $cm^2/V.s$),[92] make GaAs a suitable material system for a number of applications including solar cells, high electron mobility devices, and lasers. Furthermore, the ability to alloy GaAs with other materials such as P, Al, and In enables an access to a wide span of tunable optoelectronic properties such as band gap energies. The knowledge developed during self-seeded GaAs nanowire growth by MOCVD becomes a crucial for the growth of GaAs based ternary nanowires.

Despite the recent success in MBE growth of self-seeded GaAs nanowires, self-seeded growth of GaAs nanowire array by MOCVD has shown limited progress, although MOCVD is an industrial-scale technique that can yield high growth rates and high nanowire throughput.

Early studies have shown the premise of Ga as a seed material[93] and GaAs nanowire growth was achieved on SiO_2 [94,95] or bare GaAs substrates;[96] however alignment, morphology or density-diameter control of nanowire arrays were limited. Although diameter and position controlled nanowires has been grown without a seed particle by selective area epitaxy (SAE) in MOCVD, this method requires mask pattern layer to drive one-dimensional growth of nanowires.[50,97]

In this chapter, we demonstrate self-seeded growth of binary GaAs nanowire arrays and in the Chapter 4: we demonstrate controlled density and diameter on GaAs substrates without any mask or oxide layer and using MOCVD. We show that the growth of nanowires and the resulting morphology depend on the balance of incorporation and extraction rates of Ga into and out of the Ga droplets. By decoupling seed deposition and nanowire growth steps, we achieve successful nanowire growth. Analysis of our results demonstrates that this technique is general and can be applied to other self-seeded III-V nanowires.

3.2. Ga-seeded GaAs nanowire growth

In this work, Ga-seeded GaAs nanowires were grown by MOCVD using a two-step growth: in the first step Ga seed droplets were deposited by flowing TMGa at elevated temperatures and in the second step nanowire growth was performed by flowing TMGa and AsH_3. In this section, we show the evolution of the growth in each step and propose a growth model to explain nanowire morphology.

Ga-seeded GaAs nanowire growths were performed on GaAs substrates with (111)B surface normal. Substrates were cleaned to remove organic contamination and loaded into MOCVD. First, substrates were annealed at 600°C under H_2 carrier gas to remove native oxide of the substrates. After annealing, *in situ* deposition of Ga seed particles was performed by flowing TMGa at 600°C for 1 min. Following seed deposition, temperature was dropped for nanowire

growth and TMGa and AsH_3 are flown together for GaAs nanowire growth and reactor was cooled. Details of growth conditions are given in section 2.1.2.

Ga seed deposition. Prior to discussion of GaAs nanowire growth, *in situ* deposition of Ga seed particles in the first step was confirmed by a separate experiment where TMGa is flown (0.36 standard cubic centimeters per minute, sccm) on GaAs (111)B substrate at 420°C for 1 min and sample was cooled immediately under H_2 flow. Figure 3.1 shows SEM images of Ga seed particles that were formed as a result of TMGa flow. It should be noted that control of Ga seed diameter-density using the seed deposition parameters can be achieved, discussed in Chapter 4:.

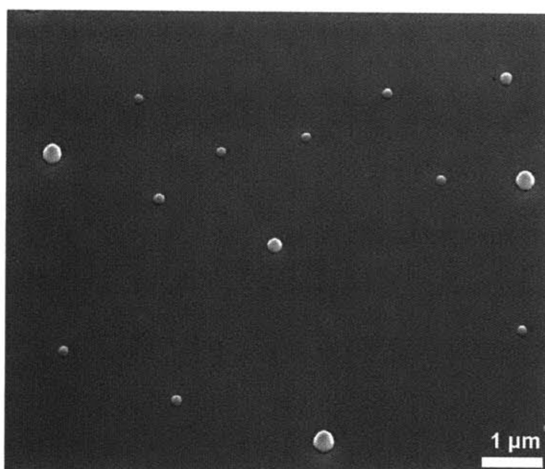

Figure 3.1 Ga seed formation by *in situ* deposition. SEM image of Ga droplets formed on the GaAs (111)B growth substrate immediately after the Ga deposition step at 420°C.

GaAs nanowire growth. Figure 3.2a shows the resulting morphology of as-grown self-seeded GaAs nanowires grown on GaAs (111)B substrate at 420°C with V/III ratio of 2. The majority of nanowires exhibits an epitaxial relationship with the substrate resulting in vertical nanowires on the substrate and is observed to have two distinct regimes of tapering (diameter change per length), as shown in Figure 3.2b. At the nanowire base, significant tapering is observed followed by a discrete reduction in tapering that is maintained throughout the nanowire growth. We suggest that the observed morphology evolves through the following steps (Figure 3.2c): (i) Ga

droplet formation starts as a result of effective *in situ* TMGa deposition at higher temperatures (500°C – 600°C);[98] (ii) after engaging both precursors (TMGa and AsH_3) at 420°C – 435°C, GaAs nanowires start to nucleate preferentially at the Ga seeds and the Ga droplets transform into GaAs bases; (iii) after the base formation, nanowire growth occurs as a result of TMGa and AsH_3 supply, and the nanowire growth ceases when Ga droplet is depleted.

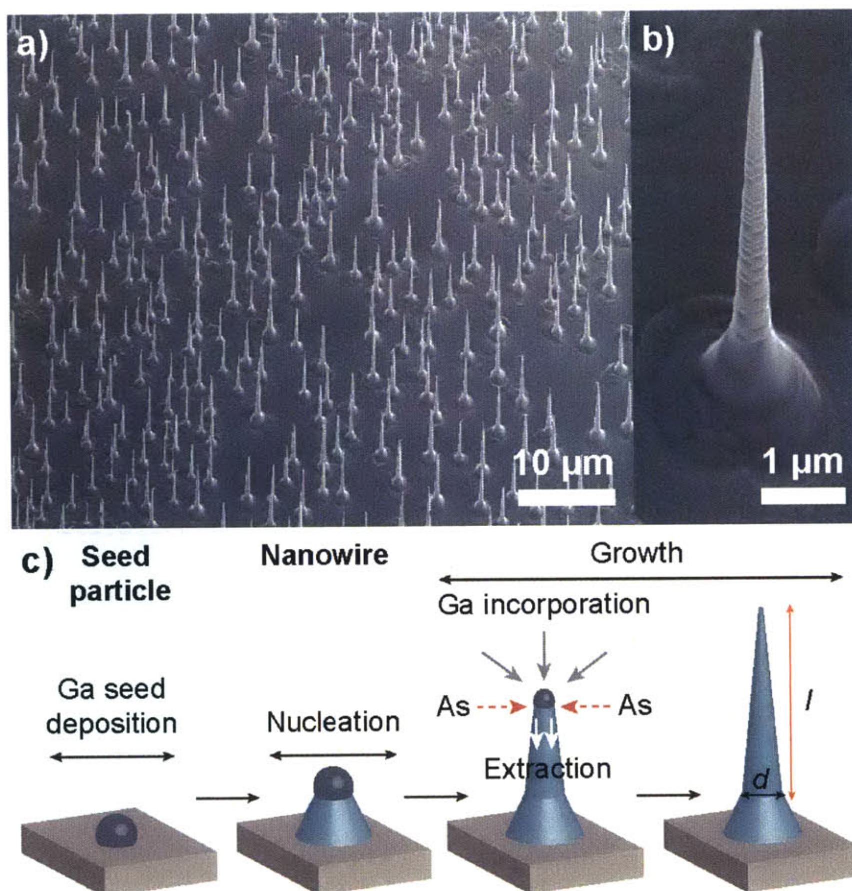

Figure 3.2 Self-seeded nanowire growth. (a) SEM image of a GaAs nanowire array showing the alignment of nanowires on the GaAs (111)B substrate. (b) SEM image of a single nanowire taken at 45° tilt showing the nanowire morphology with two regions (base and nanowire) that have distinct tapering rates. (c) Nanowire growth schematic; *in situ* Ga seed deposition is followed by nanowire nucleation and growth. The balance of Ga incorporation into the seed particle and Ga extraction from the seed particle determines the tapering of the nanowire during growth. Nanowire length and diameter is denoted as *l* and *d*, respectively.

Necessity of two-step growth. It has been crucial to separate seed deposition temperature and nanowire growth temperature in Ga-seeded GaAs nanowire growth by MOCVD to achieve high yield of vertical nanowires with epitaxial relationship to the substrate. Nanowires were grown at lower temperatures (<500°C) to promote preferential nucleation at the seed particle – substrate interface. Our initial attempts to perform seed deposition and nanowire growth *both at the low temperatures* (such as 420°C) have resulted in mostly kinked nanowires, suggesting seed particle instability during growth. In rare cases vertical nanowires with epitaxial relation to the substrate were grown (Figure 3.3a); however, uniformity and reproducibility of these growths could not be accomplished, Figure 3.3b. In these growths, seed deposition temperature and nanowire growth temperature were the same (420°C), Ga seeds were deposited by flowing TMGa (0.836 sccm) for 1 min and GaAs nanowires were grown for 20 min by flowing TMGa (0.836 sccm) and AsH_3 (3.350 sccm) on GaAs (111)B substrate. Therefore, even though Ga seed particles can be deposited at lower temperatures (*i.e.* 420°C) as shown in Figure 3.1, subsequent nanowire growth attempts have resulted in successful growths for a small portion of substrate and repeatability and substrate uniformity of growths has been problematic. At first glance, kinked nanowire growth (Figure 3.3b) might be attributed to the growth conditions that are not optimized. However, nanowire growths with a wide span of growth conditions had resulted in similarly kinked nanowires. On the contrary, when seed deposition is performed at high temperatures (500°C – 600°C) and nanowires are grown subsequently at lower temperatures (420°C – 450°C), high yield of vertical nanowires with epitaxial relationship with the substrate are achieved for every growth of sufficient growth duration, such as Figure 3.2a. Therefore, for optimized Ga-seeded GaAs nanowire growth, seed deposition has been performed at high temperatures.

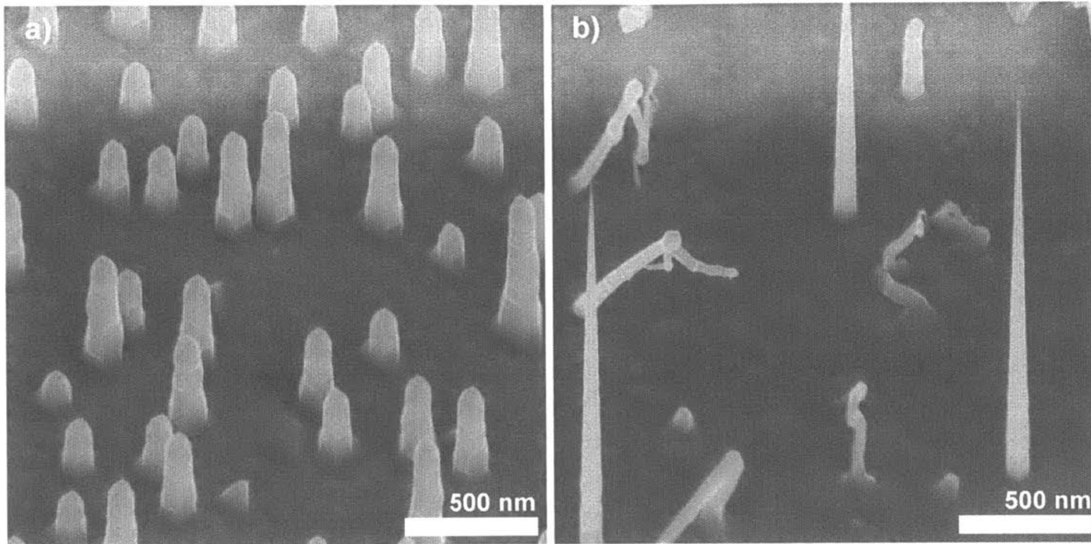

Figure 3.3 Effect of low seed deposition temperature on repeatability of nanowire growth. (a, b) SEM images of different GaAs nanowires growths performed at the same seed deposition temperature and growth temperature (420°C) and same precursor flow rates. Repeatability of growths is unachievable in the case of low temperature seed deposition conditions.

As demonstrated above, a two-step growth – where Ga seed deposition is performed at higher temperatures and nanowire growth is performed at lower temperatures – is required for epitaxial nanowire nucleation and stable Ga droplet to prevent kinking along the nanowire. We attribute the requirement for high temperatures during Ga seed deposition to two aspects of group-III droplet formation and kinetics. First, temperature plays a role in decomposition of TMGa precursor during the seed deposition. Comparing MBE and MOCVD growth of self-seeded GaAs nanowires, different temperatures for seed deposition and nanowire growth are not necessary during MBE growth. However, MOCVD requires TMGa decomposition to form Ga adatoms. Therefore, higher temperatures are required for effective TMGa decomposition[98] during the seed deposition step compared to the nanowire growth step, when the temperature is lowered to confine precursor decomposition only at the seed particle. High temperatures also promote thermodynamic equilibrium between the Ga seed particle and the substrate. Second, Ga

droplets have temperature-dependent physical mobility; between ~610°C – 630°C Ga droplet mobility is at its lowest, whereas below 600°C or above 630°C the droplet mobility increases.[99] The Ga droplets in the study were formed by excess evaporation of arsenic during high temperature annealing of GaAs in vacuum. Our seed deposition and nanowire growth conditions are different from this study that observes temperature-dependent Ga mobility,[99] such that Ga droplets are deposited in H_2 ambient at atmospheric pressure rather than formed by accumulation of Ga due to excess arsenic evaporation. However, if Ga droplets are stable when deposited at temperatures near 600°C and can retain stability (immobility) due to effects such as equilibrium of chemical potentials of Ga between GaAs substrate and Ga droplet, an enhancement of epitaxial vertical growth at nanowire growth temperatures (420-450°C) can be achieved, as we observed in our growths (Figure 3.2a-b).

3.3. Nucleation and growth of nanowires

To gain a better understanding of nanowire nucleation and growth mechanisms, we investigated the base and nanowire body using cross-sectional TEM structural analysis (Figure 3.4). First, a TEM sample was prepared using focused ion beam (FIB); a cross-sectional lamella of GaAs nanowire on the substrate was thinned and lifted from the substrate and attached to a TEM grid. Further thinning was performed to achieve electron-transparent thickness and low voltage thinning was performed to remove amorphous regions caused by the beam damage. With this technique, we obtained a TEM sample that shows the interface between the substrate, base and nanowire.

Cross-sectional TEM image of a nanowire on the GaAs substrate is shown in Figure 3.4a. The base has an epitaxial relationship with the substrate and is single crystalline, free of stacking faults and twin planes (Figure 3.4b, c). The selected area diffraction (SAD) pattern obtained from

the base and substrate region (Figure 3.4d) shows a zincblende single crystal structure with a <111> growth direction and no twinning reflections were observed. In contrast, the SAD pattern from the nanowire region (Figure 3.4e) exhibits double-spot features, a signature of twin planes in this region.

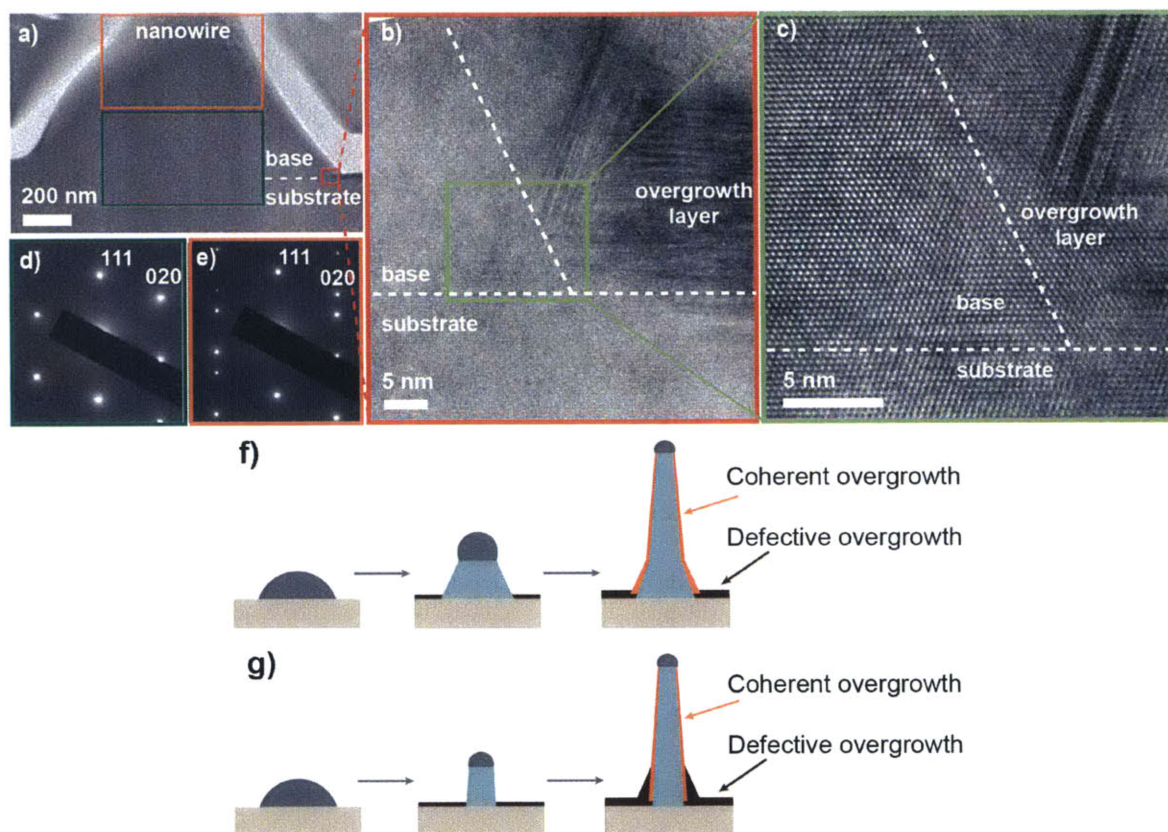

Figure 3.4 Structure of the nanowire base region. (a) Cross-sectional TEM image of the nanowire base and substrate. Outside of the nanowire base, defective overgrowth layer can be seen. The red box outlines the base-substrate junction, shown in high magnification in (b) and (c). The green and orange boxes outline the regions used to obtain SAD patterns from the base and nanowire, respectively. (b-c) High resolution TEM images of the interface between the base and substrate, taken along ⟨10-1⟩ zone axis. Base region is defect-free whereas a defective overgrowth layer can be seen outside of the nanowire base. (d-e) SAD patterns from the base (d) and nanowire (e) regions. Twinning planes in the nanowire cause double spots seen in the nanowire SAD pattern. (f-g) Schematic representation of two possible base formation mechanisms: base formation occurs as a part of the nucleation process (f) or as a result of preferential sidewall deposition at the substrate-nanowire junction (g).

Investigation of the structural quality at the interface can help us understand base formation mechanism. Two possible mechanisms that can explain the base formation are: (1) base formation occurs during nucleation (Figure 3.4f), or (2) base formation occurs as a result of preferential sidewall deposition at the nanowire-substrate junction (Figure 3.4g). These hypotheses can be examined by the extent of the parasitic overgrowth at the base-substrate interface where nucleation occurs. From higher magnification images obtained at the edge of the base-substrate region (as shown in the red box in Figure 3.4a and at higher magnification in Figure 3.4b), we observe that the overgrowth layer – which appears as a darker contrast due to the presence of defects – stops at the base edge and the base/substrate interface is free of defects (Figure 3.4c). Simultaneously with the nanowire growth, a parasitic thin film overgrowth on the substrate occurs *via* excess adatoms that do not contribute to the nanowire growth. This thin-film overgrowth layer has a lower growth rate than the nanowire base because of lower nucleation probability on the bare substrate than below the seed particle, and is defective due to non-optimized conditions for thin film growth. If the base formation occurs as a part of the nucleation process (schematically shown in Figure 3.4f), the parasitic overgrowth layer would be observed on the substrate but not in the base region. However, if the base formation occurs due to preferential sidewall growth at the substrate-nanowire junction during the growth, as depicted in Figure 3.4g, the defective overgrowth layer would also be observed in the base region. Cross-sectional TEM study in Figure 3.4a-c shows that overgrowth layer does not extend into the base region, suggesting that the operating mechanism is as depicted in Figure 3.4f, and that base formation occurs as a part of the nucleation process.

In contrast to the defect-free structure of the base, structural analysis of the nanowires above the base (Figure 3.5) reveals the presence of rotational twin planes perpendicular to the nanowire

growth direction. The sidewalls of the self-seeded GaAs nanowires have a zigzag structure when viewed along the [10-1] zone axis (Figure 3.5a-b) due to a change of sidewall direction after each twin plane. The SAD pattern (Figure 3.5c) confirms the zincblende crystal structure of the nanowires and growth along the <111> direction, whereas the observed double spot structure in the SAD pattern is caused by symmetry in the crystal structure due to twin planes.[62,100] This observation of twin planes along the <111> growth direction is consistent with twinning commonly observed in III-V nanowires.[62,100–103]

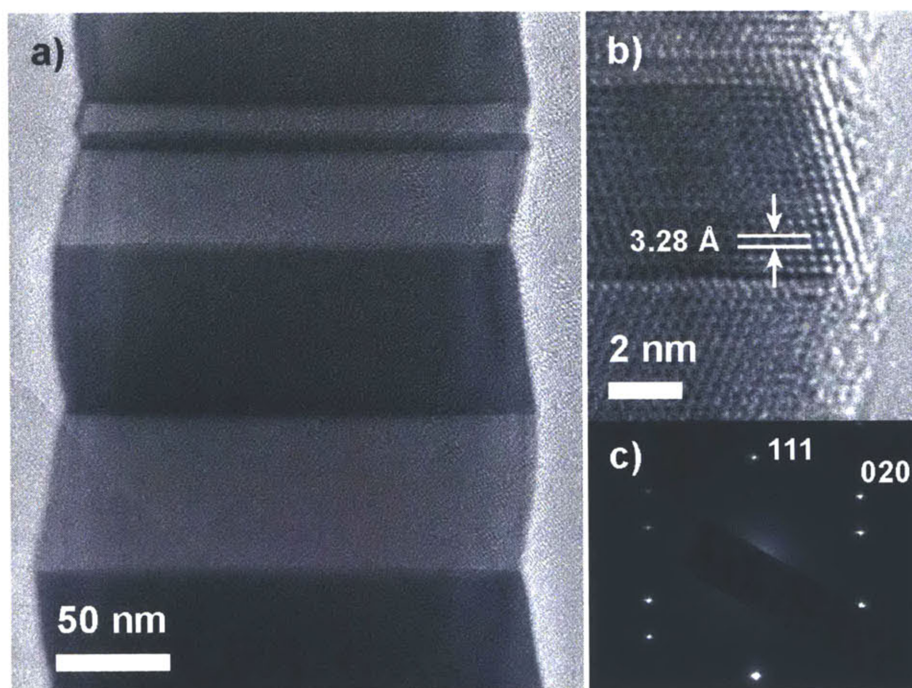

Figure 3.5 Structural analysis of the nanowires. (a) Bright field TEM images of GaAs nanowires along the [10-1] zone axis. (b) High resolution TEM image showing rotational twins. (c) SAD pattern obtained from the region shown in (a) with double spot structure as a result of rotational twins.

3.4. Nanowire morphology: Tapering

Self-seeded GaAs nanowires grown using MOCVD have tapered nanowire morphologies where nanowire diameter narrows towards the tip of the nanowire. To understand the tapering of nanowires, we investigate the nanowire length (l) as a function of starting nanowire diameter (d), and define tapering ratio as $T'=d/l$. Figure 3.6 shows the length-diameter relationship for three different growths with the same V/III ratio, but with different seed deposition conditions (temperature and TMGa flux, as denoted in the graph legend) that yielded nanowire diameters from 250 nm to 1.7 μm. (We note that smaller TMGa flux during seed deposition results in less dense nanowires with smaller diameters). For each growth the length – diameter relationship follows a linear trend, meaning the tapering rate is similar irrespective of starting nanowire diameter. Furthermore, the length-diameter relationship among different growths with the same V/III ratio follows a linear trend up to the starting nanowire diameters of ~1.2 μm, meaning the tapering rate is similar between growths and determined by the growth conditions rather than seed deposition conditions. The nanowires with starting diameters larger than ~1.2 μm show a slight deviation from the linear relationship; however, this may be due to the lower areal density in larger diameter regions, which can alter local growth conditions. Here, nanowire diameter and length is measured from base/nanowire interface (the inset of Figure 3.6) where there is a discrete reduction in tapering that is maintained throughout the nanowire length, compared to significant tapering at the base.

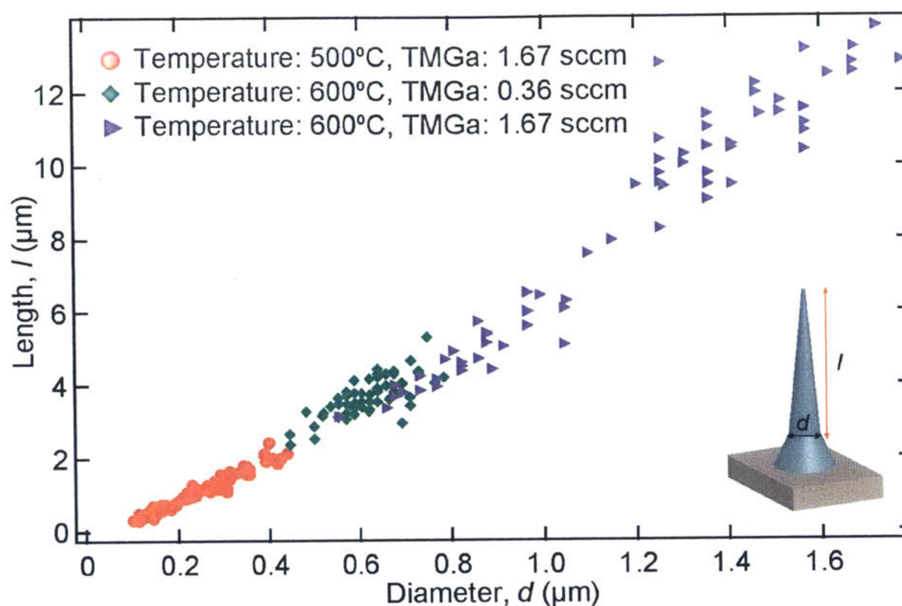

Figure 3.6 Length-diameter relationship. Length of nanowires (*l*) *vs.* starting nanowire diameter (*d*) for growths performed with the same V/III ratio, but with different seed deposition conditions ("temperature" refers to the seed deposition temperature, whereas "TMGa" refers to the flow rate of Ga precursor during the 60 s Ga seed deposition step).

The tapering rate is determined by the balance of Ga incorporation into the seed particle and its extraction out of the seed particle, dictated by the TMGa and AsH_3 flow rates, respectively (Figure 3.2c). When the incorporation rate of Ga is smaller than extraction rate, Ga is depleted from the seed, which shrinks and consequently yields a tapered nanowire morphology. For a given growth, the tapering rate $T'=d/l$ depends on the growth parameters and is similar irrespective of starting nanowire diameter (Figure 3.6), which we successfully modeled by a simple incorporation and extraction mechanism of elements from the seed particle in the growth model section 3.5.

3.5. Growth Model

We model the nanowire growth and tapering for the self-seeded growth mechanism to explain the constant tapering as a function of growth parameters. Here, to understand the

evolution of the tapering, we define diameter change per length change as $\Delta d/\Delta l$. The nanowire diameter is constrained by the seed diameter that depends on the incorporation and extraction rates of Ga into and out of the seed particle:

$$\Delta V/\Delta t = I - E$$

Equation 3-1

where V is the volume of the seed particle, t is the time, I and E are incorporation and extraction rates, respectively, in μm^3/min. The nanowire length change depends upon the growth rate, $G = \Delta l/\Delta t$, measured in µm/min. Assuming the seed particle mostly consists of Ga due to low solubility of As in the Ga liquid and the growth rate is not dependent on the nanowire diameter (a reasonable assumption for large diameter nanowires), we can express the tapering for a hemisphere seed particle as:

$$\Delta d/\Delta l = (I\text{-}E) / (\tfrac{1}{4}\,\pi\, d^2\, G)$$

Equation 3-2

where the dominator ($\frac{1}{4}\,\pi\, d^2$) describes the relation of the seed volume to the seed diameter ($\Delta V/\Delta d$) for a hemispherical particle. Therefore tapering ($\Delta d/\Delta l$) has a negative value when incorporation is less than extraction, and nanowire diameter gets smaller towards the tip of the nanowire. This relation can be further generalized by normalizing the incorporation ratio, I, to the seed particle surface area, and obtaining incorporation rate per area, k, in µm/min:

$$k = I / (\tfrac{1}{2}\,\pi\, d^2)$$

Equation 3-3

We can also relate G and E by the area of the seed/nanowire interface, such that $E = G * (\frac{1}{4}\,\pi\, d^2)$. Inserting these relations into Equation 3-2, we obtain:

$$\Delta d/\Delta l = 2k/G - 1$$

Equation 3-4

This result shows that the tapering rate is a function of the growth parameters k (incorporation rate per area, in μm/min) and G (growth rate, in μm/min), which depends on the precursor fluxes and the growth temperature, and it is independent of the starting diameter, as experimentally measured and shown in Figure 3.6. It should be noted that this growth model can be further refined by taking into account (i) non-hemispherical seeds, where the contact angle is not 90°, (ii) molar volume differences of Ga and GaAs when relating the extraction rate of Ga (E) to the growth rate of GaAs nanowire (G). For example, for a seed particle with a contact angle of 110°, and including the molar volume differences of Ga and GaAs, the tapering relation becomes $\Delta d/\Delta l = 1.69k/G - 0.23$. Upon refinement of the model, the tapering is still dependent upon the growth parameters k and G, and independent of the starting diameter. We note that increase of TMGa flow rate would be expected to increase both k and G, and increase in AsH_3 flow rate would increase G while also affecting TMGa decomposition kinetics,[104] thereby increasing k indirectly. Therefore, reducing the tapering rate of nanowires by changing flow rate of a single precursor is not anticipated due to complexity of precursor decomposition kinetics.

3.6. Investigation of radial shell growth

Whereas nanowires grow in the VLS mechanism through the seed particle, excess precursor adatoms can decompose along the nanowire sidewalls and deposit directly onto the sidewalls from vapor phase *via* vapor-solid (VS) radial growth. Optimized growth conditions, such as low nanowire growth temperatures to minimize precursor decomposition on the sidewalls and low V/III ratios to increase the surface diffusion of group-III adatoms, can inhibit radial growth. Under optimized growth conditions, TEM images of nanowire sidewalls showed smooth facets free of defects that changed direction as a result of twin planes (Figure 3.5). However, in the case of the VS radial growth, twin planes along the nanowire can be a nucleation point for defective

layers in the radial direction. To investigate structural quality of the radial layers, we have intentionally implemented radial growth by continuing the precursor delivery for 10 min after seed particle is consumed (when VLS growth is completed). Nanowire morphology does not change significantly during longer growth, since the seed-mediated growth is completed after the Ga seed particle is consumed. However, a slight increase in nanowire diameter is observed as a result of the additional 10 min growth.

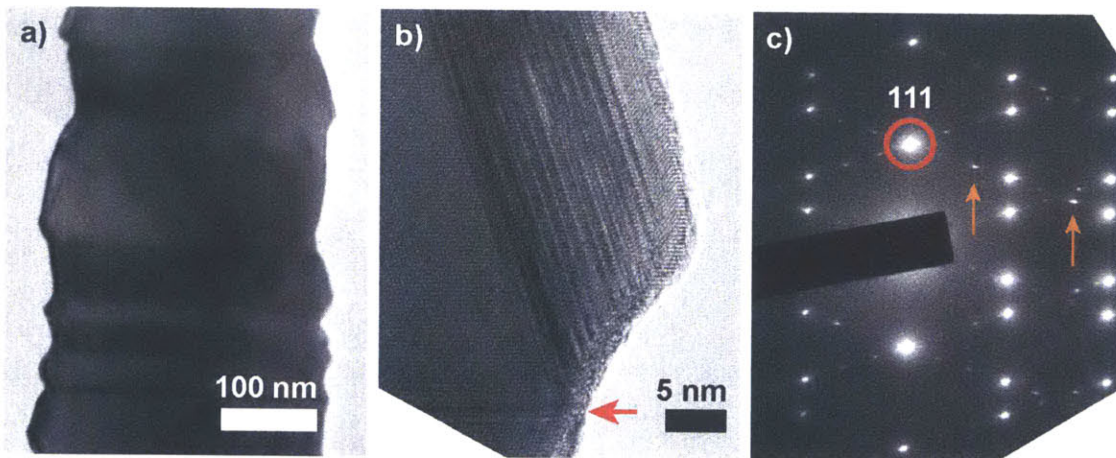

Figure 3.7 Effect of radial growth on the nanowire structure investigated by TEM. (a) Bright field TEM images of GaAs nanowires along the [10-1] zone axis. (b) High resolution TEM image showing defective radial growth nucleated through the twin plane (shown in red arrow). (c) SAD pattern obtained from the region shown in (a) where extra spots appear due to twinned structure of the radial growth.

Due to twin planes, it is possible to identify radial growth by TEM, as seen in Figure 3.7. The facets of nanowire are not smooth (Figure 3.7a), and in the higher magnification image the defective radial growth layer is seen (Figure 3.7b). The highly twinned radial growth layer is likely to be nucleated from the twin plane along the nanowire growth direction, the position is shown with the arrow in Figure 3.7b. The twinning of the radial growth is also apparent in the SAD pattern coming from the Figure 3.7a region – extra spots perpendicular to the sidewalls are seen in the SAD pattern. Therefore, we conclude that when radial growth occurs, there is a

signature effect on the nanowire structure that can be observed in high resolution TEM images and SAD patterns.

3.7. Effect of growth temperature

The effect of nanowire growth temperature on nanowire morphology was investigated. By changing growth temperature, nanowire nucleation kinetics such as growth rate and precursor decomposition kinetics are altered. Therefore, we investigated potential effects of growth temperature specifically on nanowire tapering and observed that nanowire tapering is independent of growth temperature within the temperature range of 420°C – 480°C. The temperature range was chosen based on decomposition kinetics of TMGa, at 420°C 20% TMGa decomposes, whereas at 480°C almost complete decomposition of TMGa is achieved.[98]

For this series, Ga-seeded GaAs nanowires were grown at varying growth temperatures between 420°C – 480°C and other growth conditions were kept the same. Ga seed deposition was performed by flowing 1.67 sccm of TMGa at 600°C for 1 min, followed by nanowire growth at respective growth temperature with TMGa and AsH_3 flow rates at 1.67 sccm and 18.60 sccm, respectively. Nanowire growth duration was 7 min, with the exception of growth at 450°C, where the growth duration was 3 min. Nanowires were cooled under H_2 ambient.

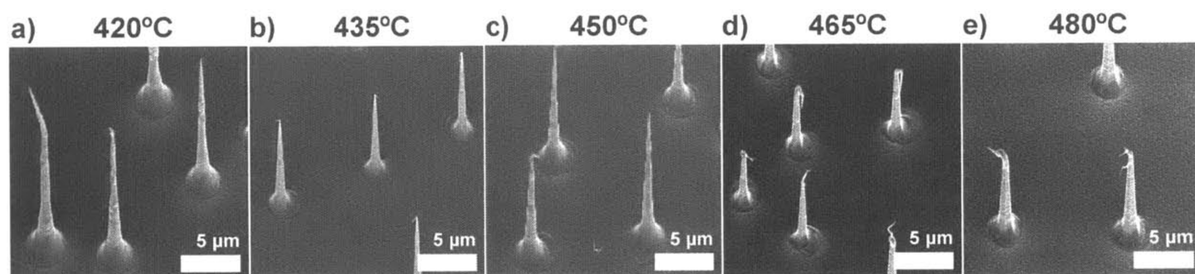

Figure 3.8 Growth temperature studies of GaAs nanowire growth. (a-e) SEM images of GaAs nanowire growth with similar growth conditions except growth temperature. Growth temperature ranges from 420°C to 480°C, as denoted on each image. Increasing growth temperature worsens the nanowire morphology and nanowire kinking is observed.

SEM images of nanowires grown at different growth temperatures are shown in Figure 3.8. Increasing growth temperature affects the morphological quality of nanowires such that for growth temperatures above 465°C the nanowires exhibit more prominent kinking near the tip. The nanowire length is different for varying growth temperature, but it also depends on the starting nanowire diameter due to tapering. Therefore, we investigated tapering rate for different growth temperatures. In this growth series, the tapering rate of nanowires ($|\Delta d/\Delta l|$) was found to be between 135-165 nm/μm. We do not observe a consistent change in tapering as a function of growth temperature.

The nanowire growth temperature range was chosen based on precursor decomposition kinetics, specifically TMGa. Studies have shown that TMGa thermally decomposes between 400°C – 480°C in H_2 ambient,[98] decomposition is ~20% at 420°C and is nearly complete at 480°C. Therefore, increasing growth temperature should increase the amount of Ga adatoms for a given TMGa flow rate. By increasing effective Ga amount during growth, tapering may be reduced – since tapering, $\Delta d/\Delta l$ is proportional to the imbalance of incorporation, I and extraction, E of Ga in and out of seed particle, $\Delta d/\Delta l \propto (I\text{-}E)$. However, if TMGa decomposes into Ga adatoms prior to reaching a seed particle, adatoms are likely to incorporate into the overgrowth layer on the substrate or nanowire sidewalls *via* VS mechanism. Therefore, even though growth temperature increases available Ga adatoms, these adatoms may not reach to the seed particle and increase incorporation rate k substantially. Furthermore, increasing growth temperature increases growth rate G due to kinetics of nucleation of layers at the seed/nanowire interface. Because tapering is not significantly changed with growth temperature, we conclude that growth temperature similarly affects the incorporation rate k and growth rate G.

3.8. Effect of AsH_3 flow during annealing and during cooling

In this section, the volatility of group-V elements at high temperatures and low pressures is discussed with respect to growth procedures applied for the growth of self-seeded nanowires. We review two relevant growth processes during self-seeded nanowire growth; (i) annealing before seed deposition and (ii) cooling after nanowire growth.

Self-seeded nanowire growth starts with annealing at 600°C for 10 min in atmospheric pressure MOCVD to remove native surface oxide. Throughout the thesis work, self-seeded nanowire growth studies have two types of annealing, either annealing is performed under H_2 carrier gas flow (15 liters per minute, lpm) for 10 min or under H_2 carrier gas (15 lpm) and AsH_3 flow (3.35 sccm) for 7 min, followed by H_2 flow (15 lpm) for 3 min. Following annealing, Ga seed deposition is performed. We did not observe a difference on Ga seed droplet formation based on annealing conditions.

It is reported that GaAs native oxide desorbs at temperatures between 580°C - 630°C.[105,106] Therefore, our choice of annealing at 600°C for 10 min should be sufficient to remove native oxide and prepare the substrate surface for epitaxial growth. However, at similar temperatures to annealing, preferential desorption of group-V elements from III-V material surfaces may become prominent following native oxide desorption. In literature, it is known that annealing of III-V semiconductor surfaces in vacuum at temperatures above the maximum temperature for congruent evaporation (T_c) leads to preferential evaporation of group-V elements from the surface and excess group-III materials form droplets on the surface,[99,107,108] following native oxide removal. For GaAs (100), this process is usually reported at ~625°C under vacuum conditions.[109] To observe if GaAs (111)B substrates reach the maximum congruent evaporation temperature and Ga droplet condense as a result of annealing, we performed a separate annealing

experiment. GaAs substrate was annealed at 600°C in H_2 carrier gas for 10 min and *ex situ* SEM images show that Ga droplets are not found on the GaAs surface; therefore in our study Ga seeds are deposited by TMGa flow and are not formed by excess evaporation of As. Furthermore, T_c can be increased by additional group-V flux during annealing to prevent excess evaporation of group-V materials and preserve stoichiometry of GaAs substrate surface.[109] Therefore, the second type of annealing (under AsH_3 flow for the first 7 min) should also prevent preferential As evaporation.

Following III-V material growth, cooling is usually performed under group-V precursor flow to suppress congruent evaporation of materials. In literature, this has been especially important for high-temperature thin-film growths to preserve stoichiometry and surface quality. In GaAs nanowire growth experiments, optimized growth temperatures are lower (between 420°C – 435°C) and nanowires are cooled in two different methods; either in only H_2 flow or H_2 and AsH_3 mixture flow until 350°C. Experiments with cooling under H_2 aimed to observe Ga droplet at the tip of the nanowire; however, either due to long growth durations nanowires were fully grown and Ga droplet was consumed, or Ga droplet was crystallized into kinked structures near the tip of nanowire. It should be noted that even though AsH_3 is not flown during cooling, this crystallization during cooling might have been possible due to excess AsH_3 adsorbed to the atmospheric pressure reactor walls and susceptor. In the experiments with cooling under H_2 and AsH_3 mixture flow, we aimed to preserve nanowire morphology near the tip and prevent kinking by supplying AsH_3.

In summary, we do not observe significant effects of additional AsH_3 flow during annealing or cooling on nanowire morphology. For the following experiments in Chapter 5:, we performed annealing under H_2 and AsH_3 mixture flow for the first 7 min, followed by 3 min annealing in H_2

flow, and for the experiments in Chapter 4: and Chapter 5: cooling in H_2 and AsH_3 mixture flow until 350°C, similar to the III-V growth in literature.

3.9. Conclusions

We have demonstrated controlled self-seeded GaAs nanowire growth by MOCVD. Nanowire growth *via* a self-seeded mechanism eliminates possible impurities from foreign metal seed by using one of the constituent elements of the nanowire as the seed particle. The growth is achieved in two steps; *in situ* Ga seed deposition at higher temperatures followed by nanowire nucleation and growth at lower temperatures. Separation of the seed deposition temperature from nanowire growth temperature has resulted in highly reproducible vertical nanowire growth. Two distinct parts of the nanowire were observed: a defect-free single crystalline nanowire base with a high degree of tapering followed by the nanowire itself, which has a lower degree of tapering but contains twin planes perpendicular to the nanowire growth direction. Nanowire tapering was found to be dependent on growth conditions and independent of seed deposition conditions and starting nanowire diameter. Constant tapering along nanowire is explained by modeling the seed particle incorporation-extraction dynamics. Due to imbalance of incorporation and extraction of Ga in and out of the seed particle, Ga seed is consumed during growth and VLS growth stops when Ga seed is consumed completely. Longer growths confirmed that upon Ga seed consumption precursors incorporate to the nanowire sidewalls *via* VS mechanism and result in radial growth. Nanowire growth temperature has not altered tapering of nanowires significantly. While higher temperatures increase decomposition of TMGa and provide larger amounts of Ga adatoms, VS growth mechanism competes with VLS at higher temperatures and incorporation of Ga into the seed particle for VLS growth does not significantly increase. Lower nanowire growth temperatures (420°C - 450°C) have shown better nanowire morphologies with suppressed

kinking at the tip of the nanowires. Our findings on the nucleation and growth mechanisms of GaAs nanowire arrays can be readily extended to other III-V material systems and serve as a general approach to self-assisted nanowire growth.

Chapter 4: Density and diameter control of self-seeded nanowires

In the previous chapter, we demonstrated self-seeded binary GaAs nanowire growth and investigated growth mechanism of Ga-seeded nanowire growth. Here we use this knowledge to demonstrate density and diameter control of self-seeded GaAs nanowires grown by metal-organic chemical vapor deposition (MOCVD). Self-seeded nanowires are grown in a two-step growth: *in situ* Ga seed deposition followed by nanowire growth. Separation of the seed deposition and nanowire growth steps enables us to control areal density and diameter of nanowires independent of the growth conditions, thus density and diameter can be altered within a larger parameter space than the optimized nanowire growth, which can be achieved within a small parameter space, especially in terms of growth temperature. Seed deposition temperature is a crucial parameter in controlling the nanowire density and diameter; we have observed that increased seed deposition temperature decreases the nanowire areal density and increases nanowire diameter due to larger surface diffusion length of Ga adatoms. Furthermore, choice of substrate orientation, such as (111)B, (110) and (111)A, significantly alters density and diameter of nanowires due to a change in nucleation kinetics, which depend on chemical potentials of Ga adatoms on the substrate. We have found that the nanowire areal density is smallest for nanowires grown on (111)B, it increases for nanowire grown on (110) and the highest densities are observed on (111)A. Also, effects of the seed deposition duration on nanowire density was investigated and found that longer seed deposition time increases the areal density of nanowires

with minimal effect on average nanowire diameter. The methods described in this section constitute the basis of density and diameter control in self-seeded nanowire growth and can be extended to other self-seeded nanowire growth of III-V binary and ternary material systems.

4.1. Introduction

In vapor-liquid-solid (VLS) growth of nanowires, density and diameter control of nanowires have been achieved using a variety of methods. In general, these methods can be classified in two branches: first branch involves techniques that may rely on self-assembly and are random in their nature, such as nanoparticle drop-casting, thin-film annealing to create seed nanoparticles, or *in situ* seed formation by flowing precursor material; second branch involves techniques that are deterministic in their nature, where uniform size and orderly position of seed particles sites are determined by additional methods such as lithography techniques to create a mask followed by the seed deposition. Lithography techniques can create ordered nanowires, but this approach requires an extra step that is time-intensive. In this chapter, we focus on a subsection of self-assembly techniques for seed deposition: *in situ* deposition of seed particles where seed element is group-III element of the nanowire.

Density and diameter control of nanowires is especially important for utilization of nanowires in device applications. Nanowire-based devices have been achieved using single-nanowires as well as nanowire arrays. Whereas single-nanowire devices are important as a proof-of-concept demonstration, devices based on nanowire arrays are usually necessary for real-world applications. Most of the nanowire array devices such as solar cells have been demonstrated for nanowire arrays that utilized lithography techniques to achieve ordered nanowire spacing and uniformity.[8] Ordered arrays can increase the absorption through scattering between nanowires.[30] However, depending on the device application, self-assembly techniques may suffice in terms of

density and diameter control, especially with narrow distributions of average size and fairly uniform positions of nanowires. Such nanowire arrays can be utilized for solar cells[110] and light-emitting diodes (LEDs) where nanowires do not need to be identical in morphology throughout the substrate. Self-seeded nanowire arrays without a mask, albeit more random than lithographically determined nanowire arrays, would still lead to increased scattering from nanowire sidewalls and increased absorption.[4] Therefore, it is crucial to establish methods to control the morphology, density, and alignment of self-seeded nanowire arrays.

The growth of self-seeded nanowires using *in situ* deposition of seed particles in MOCVD is detailed in 0. To summarize, in the case of III-V nanowire growth, seed deposition is achieved by exposing the substrate to group-III precursor flow – for example trimethylgallium (TMGa) for Ga seeds. The precursors decompose at high temperatures and form droplets on the surface due to substrate surface energies. Deposition parameters such as temperature and substrate energy can be used to control the nucleation of seed particles, which consequently determines the density and diameter of the seed particles. After seed particle deposition, nanowire growth is performed, where nanowire density and diameter mimics the seed characteristics at the time of nanowire nucleation.

It has been shown in the case of MBE-grown nanowires[111] that density and diameter control of self-seeded growth is more challenging compared to the foreign metal-seeded growth because nanowire density depends on the *in situ* nucleation step of the group-III seed particles. To achieve nucleation, MBE GaAs nanowire growth has been performed on substrates with a thin SiO_x layer[67,83,85,111,112] such that Ga droplets nucleate at pinholes in the oxide layer. In this way, the density of nanowires is affected by parameters such as oxide thickness[111] and growth temperature,[66,83] whereas the diameter of the nanowires is affected by the precursor flow

rates.[111,112] Recently, density and diameter control of self-seeded GaAs nanowires has been demonstrated by combining droplet epitaxy and self-seeded growth, where GaAs islands are formed by droplet epitaxy on oxide-free substrates and nanowire growth occurs on top of these islands.[113] This approach separates the nucleation and growth of nanowires providing control over density and diameter during the nucleation step.

In this chapter, we demonstrate self-seeded growth of GaAs nanowire arrays with controlled density and diameter on GaAs substrates without any mask or oxide layer and using MOCVD. While seed particle characteristics at the time of nanowire nucleation directly affect nanowire density and diameter characteristics, *in situ* study of these characteristics is not possible in MOCVD. Although *ex situ* study of seed particles may give information about particular trends, cooling of seed particles to room temperature may affect their size and distribution. To ensure that we investigate seed deposition characteristics at the time of nanowire nucleation, we performed nanowire growth after seed deposition and investigated nanowire density and diameter.

4.2. Effect of seed deposition temperature on density and diameter control

In this section we investigate the effect of seed deposition temperature on Ga seed formation kinetics. We altered the seed deposition temperature between 500 °C – 600 °C, while keeping all other growth parameters the same (seed deposition was performed with 1.67 sccm TMGa flow for 1 min and the nanowire growth was performed at 435°C on GaAs (111)B substrates with V/III ratio of 5). In these growth series, nanowires were cooled under AsH_3 flow down to 350°C to suppress kinking at the tip of the nanowires during cooling.

Top-view SEM images show the change in the areal density of nanowires as a function of the seed deposition temperature between 500 °C – 600 °C (Figure 4.1a – e). Nanowires appear as

dots in the top-view images due to their vertical alignment on the substrate. Insets of Figure 4.1a-e show single nanowires at 45° tilts to observe nanowire diameter and length, where nanowire diameter is measured at the bottom of constant tapering (shown schematically in Figure 3.2c) and base diameter is measured at the interface of substrate and the base. It should be noted that top-view image series and 45° tilt inset series are shown at the same magnification respectively for direct comparison of images between series. It is clearly seen from top-view images that *decreasing* seed deposition temperature leads to increased areal density reduced nanowire diameter. We observe that seed deposition temperature affects the areal density and diameter simultaneously. These characteristics are summarized in Figure 4.1f; areal density is controlled between 5.5×10^{-3} – 82.2×10^{-3} nanowires/μm^2 and average nanowire diameter is controlled between 167 nm – 1.3 μm. Furthermore, the seed deposition temperature change does not affect nanowire characteristics: by changing seed deposition temperature, but maintaining other growth parameters the same, we observe that the overall nanowire morphology and structure remain the same, with the single-crystalline nanowire base and twinned nanowires (insets of Figure 4.1a – e). Nanowire length variation as a function of seed deposition temperature is expected in our growth and it is a result of diameter-length dependence explained in section 3.4.

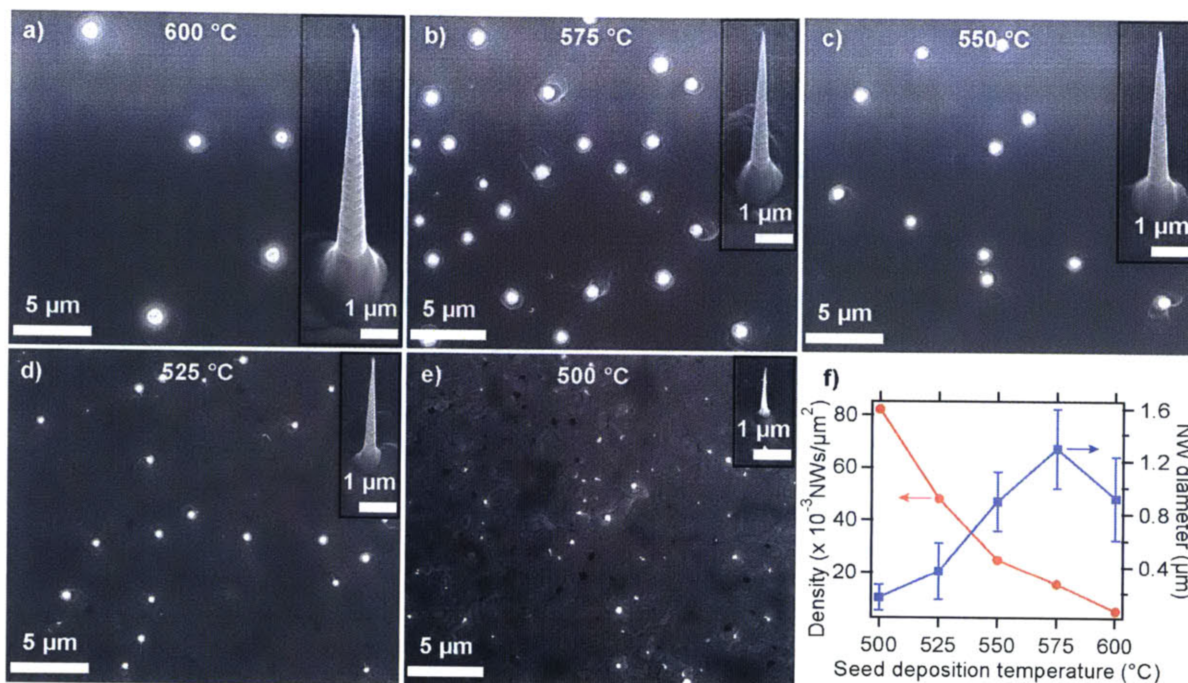

Figure 4.1 Effect of Ga seed deposition temperature on the nanowire density and diameter. (a-e) Top-view SEM images of GaAs nanowires grown with different Ga seed deposition temperatures (indicated in each image). All growths are performed on GaAs (111)B substrates at 435°C. Nanowires appear as dots in the top-view images because they grow vertically on the substrate. Insets show the nanowire morphology obtained at a 45° tilt. (f) Areal density and average diameters of nanowire arrays as a function on the seed deposition temperature.

The experimentally observed temperature-dependent density and diameter trends (Figure 4.1) can be explained by the surface diffusion of Ga adatoms and/or seed nucleation kinetics. At lower temperatures, limited mobility of Ga adatoms causes slow surface diffusion and results in a higher density of smaller seed particles, as seen in Figure 4.1f. The density-diameter trend is disrupted when the seed deposition temperature is increased from 575 °C to 600 °C, the average diameter decreases contrary to the density-diameter trend observed at lower temperatures (Figure 4.1f). This can be due to increased Ga adatom desorption at higher temperatures. Similar temperature-dependent density trends were observed in island growth by the droplet epitaxy, which is a similar process to the nanowire nucleation step described in section 2.1.2, and have

been attributed to surface diffusion.[114] The seed nucleation kinetics takes into account changes in chemical potentials and surface energies, and is described in section 4.4 in more details.

Our results indicate that the density and diameter of nanowires are coupled. However, in a recent self-seeded MBE study,[113] nanowire density and diameter were controlled by the seed deposition temperature and Ga flow supplied during the seed deposition, respectively, suggesting that a similar approach could be applied in the self-seeded MOCVD. We note that obtaining nanowires with smaller diameter than observed in this work could be possible by further decreasing the seed deposition temperature, but higher TMGa flows would be required to overcome its incomplete decomposition at lower temperatures.

4.3. Effect of substrate orientation on density and diameter control

In addition to the seed deposition temperature, the density and diameter of nanowires also depend on the substrate orientation, as shown in Figure 4.2a-c. In these experiments, seed particle deposition temperature and TMGa flow rate (600 °C and 1.67 sccm, respectively) and nanowire growth conditions were kept the same, and the nanowires were grown on GaAs (111)B, (110), or (111)A substrates at 435°C with V/III ratio of 11. The differences in nanowire diameter and density indicate that these parameters are dictated by the seed formation dynamics on different surfaces. The areal density increases from (111)B to (110) and (111)A, whereas the nanowire diameter shows the opposite trend. In addition, the nanowires grow along the <111> direction on all substrates, resulting in vertical nanowires on GaAs (111)B and (111)A surfaces and inclined nanowires on GaAs (110) surfaces.

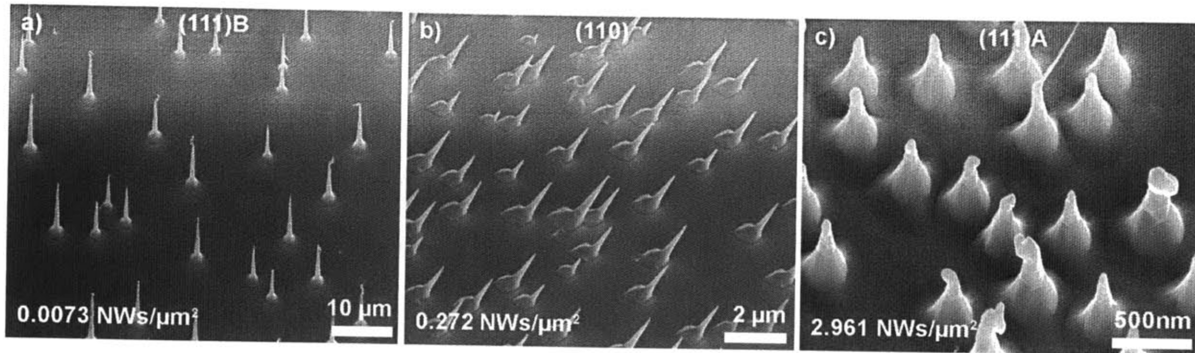

Figure 4.2 Effect of substrate orientation on nanowire density and diameter. (a-c) GaAs nanowire growth on (111)B, (110) and (111)A substrate, respectively. Areal density is given at the bottom-left corner of each image.

We now consider the same parameters (nucleation kinetics and surface diffusion) to understand the differences in density and diameter as a result of substrate orientation. Because the trend of larger diameter and lower density nanowires is similar to the temperature-controlled seed deposition, we first consider the effect of Ga adatom surface diffusion length on the seed formation dynamics. Denser nanowires on the GaAs (110) surface compared to (111)B surface would imply that the surface diffusion length on (110) surface should be shorter, but it has been reported that Ga surface diffusion length on GaAs (110) surface is longer than on GaAs (111)B surface.[115] Therefore, surface diffusion cannot explain the observed trends. Rather, we should consider the seed nucleation kinetics. According to the nucleation theory, the Gibbs free energy of seed particle nucleation, ΔG_N, is related to the chemical potentials of Ga adatom, Ga atom in liquid seed particle, and surface energies (see section 4.4). The trend of larger diameter and lower density nanowires would be observed when the critical nucleus size of the seed particle (the size above which the growth of the particle is energetically favorable) is larger on (111)B surface compared to (110) surface. Larger critical nucleus size on (111)B suggests that the Ga adatom chemical potential ($\mu^{surf}{}_{Ga}$) or substrate surface energy (γ_{sv}) under Ga-rich conditions is lower on (111)B surface compared to (110) surface. The chemical potential of Ga adatoms on a

(111)B surface should indeed be lower, because under ideal conditions, GaAs (111)B surface is As-terminated, whereas GaAs (110) surface has an equal distribution of Ga and As atoms on the surface. Same arguments also apply to describe the density-diameter differences on (111)A surface compared to (110) or (111)B surfaces.

4.4. Seed nucleation kinetics

The nanowire density and diameter trends can be explained by the seed particle formation kinetics. The Gibbs free energy of seed particle nucleation, ΔG_N, is related to the chemical potential difference and surface energies according to the nucleation theory:

$$\Delta G_N = (\mu^{l}_{Ga} - \mu^{surf}_{Ga})\, N + \gamma_{lv} A_{surf} + (\gamma_{ls} - \gamma_{sv})\, A_{int}$$

Equation 4-1

Here, relevant chemical potentials and surface energies are chemical potential of Ga adatoms ($\mu^{surf}{}_{Ga}$), chemical potential of Ga in liquid form ($\mu^{l}{}_{Ga}$), surface tension of Ga liquid particle (γ_{lv}), surface energy of substrate under Ga-rich conditions (γ_{sv}), and interface energy between substrate and the liquid Ga seed (γ_{ls}), as shown in Figure 4.3. The critical nucleus size of a particle, d_{crit} (the size of the particle for maximum ΔG_N, where $d\Delta G_N/dd_{crit} = 0$, or the size above which the growth of particle is energetically favorable), can be derived from Equation 4-1. If the seed particle is assumed to be hemispherical, then the size of seed particle can be expressed as $N = \rho$ ($\pi\, d^3/12$), where N is the number of atoms in the seed particle, ρ is the atomic density, and d is the diameter of seed particle.

$$d_{crit} = \frac{\gamma_{lv} + \frac{1}{2}(\gamma_{ls} - \gamma_{sv})}{\frac{1}{4}\rho\,(\mu^{surf}_{Ga} - \mu^{l}_{Ga})}$$

Equation 4-2

Although the exact values for $\mu^{surf}{}_{Ga}$, γ_{ls} or the droplet contact angle – from which interface area of seed droplet and substrate (A_{int}) and surface area of seed droplet (A_{surf}) can be calculated – are not known, from Equation 4-2, we can understand the dependence of the critical nucleus size on temperature or substrate energy. Critical nucleus size, d_{crit}, can be related to the nanowire density and average diameter of a nanowire array. While the precursor flow rate is the same, seed nucleation rate would be similar; however, when d_{crit} is smaller due to temperature or substrate orientation, more of the nucleated seed particles would be energetically favorable to grow, leading to a higher density array. Since the precursor flow rate is the same, the higher density seed arrays would have smaller average seed diameter.

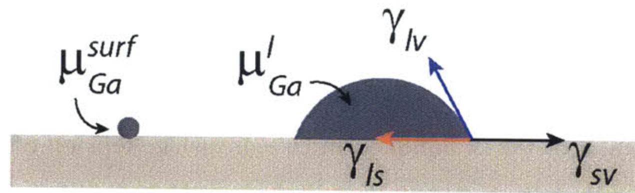

Figure 4.3 Chemical potentials and surface energies that affect seed particle formation. Here, chemical potential of Ga adatoms is indicated as $\mu^{surf}{}_{Ga}$, chemical potential of Ga in liquid form is $\mu^{l}{}_{Ga}$, surface tension of Ga liquid particle is γ_{lv}, surface energy of substrate under Ga-rich conditions is γ_{sv}, and interface energy between substrate - Ga liquid seed is γ_{ls}.

The effect of seed deposition temperature on nucleation density is mostly related to the changes in the chemical potential of Ga adatom and liquid phase Ga as a result of changes in temperature. We assume surface energy changes are relatively small between 500°C and 600°C, thus the seed particle contact angle should be similar as well. Increasing the nucleation temperature results in lower density of nanowires and larger diameters as shown in Figure 4.1a-e, which implies that the critical seed nucleation size must be larger at higher temperatures. This is expected, because the absolute value of the driving force for seed nucleation ($\mu^{l}{}_{Ga} - \mu^{surf}{}_{Ga}$)

decreases with increasing temperature. Since the driving force has a negative value, the decrease of the driving force at higher temperature increases the critical free energy and critical nucleus size.

The nanowire density can be plotted as a function of seed deposition temperature in Arrhenius plot (Figure 4.4), which suggests that the underlying mechanism has activation energy. If we consider surface diffusion of Ga adatoms as the main mechanism, we can estimate the diffusion length, λ, based on the density of seed particles, n, by the relationship $n = 1/(4\lambda^2)$ where adatom collection area of each seed particle is a square with 2λ edge length. This relation estimates the surface diffusion length to be 1.74 µm at 500 °C and 6.75 µm at 600 °C. Surface diffusion length, λ, and diffusion coefficient, D, are related by $\lambda = 2\sqrt{(Dt)}$. The activation energy for diffusion coefficient of Ga adatoms on GaAs (111)B surface can be extracted by inserting $D = D_0 * \exp(-E_{diff} / k_bT)$ and is found to be E_{diff} = 1.51 eV. It should be noted that this estimation does not take into account seed nucleation kinetics, which would also play a role in determining the density.

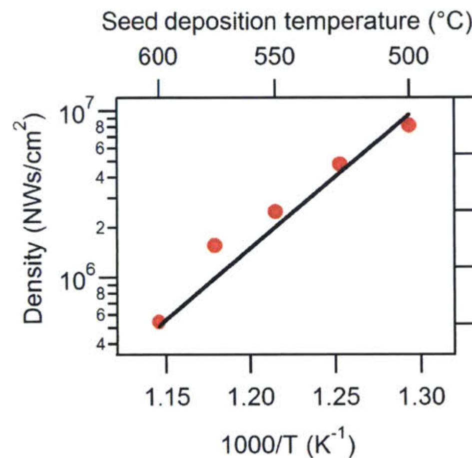

Figure 4.4 The dependence of nanowire density on seed deposition temperature shown in Arrhenius plot. Seed deposition is performed by flowing TMGa at 1.67 sccm for 1 min. Density is measured after nanowire growth.

The effect of the substrate orientation on nucleation density is related to two parameters; (i) the surface energies and (ii) chemical potential of Ga adatoms on different surfaces. As shown in Figure 4.2a-b, the density increases when the surface orientation is changed from (111)B to (110), which implies a smaller critical nucleus size on the (110) surface. According to Equation 4-2, a smaller critical nucleus size implies higher $\mu^{surf}{}_{Ga}$ or higher γ_{sv} for (110) substrate under Ga rich conditions. Data on the chemical potential of Ga adatoms on different surfaces is scarce; however, GaAs (111)B surface is As-terminated, whereas GaAs (110) surface has an equal distribution of Ga and As atoms on the surface, therefore it is likely that the chemical potential of Ga adatoms on a (110) surface will be higher due to the presence of Ga atoms. Additionally, surface energies are orientation-dependent. Under Ga-rich conditions, GaAs (111)B surface has $\sqrt{19} \times \sqrt{19}$ reconstruction,[116] for which the surface energy is expected to be between 40-63 meV/Å^2.[117] On the other hand, GaAs (110) surface has a surface energy of 52 meV/Å^2 under Ga-rich conditions. The same arguments are valid to explain the higher density on (111)A surface compared to (110) surface. The expected chemical potential of Ga adatom is higher on (111)A due to a Ga-terminated surface. The substrate surface energy is slightly higher on (111)A (54 meV/Å^2 under Ga-rich conditions) compared to (110) substrate (52 meV/Å^2 under Ga-rich conditions). Therefore, we explain the increased density on (110) and (111)A substrates by the increase of chemical potential of Ga adatom and/or substrate energy on these substrate orientations.

By understanding the effect of surface diffusion and seed nucleation kinetics, it is possible to predict density and diameter trends of self-seeded III-V nanowires in general. First, the effect of seed deposition temperature on nanowire density and diameter would be similar in other III-V material systems, *i.e.* increasing density with decreasing seed deposition temperature, as long as

the seed deposition temperature range is lower than the desorption-limited region for adsorbed seed adatoms. Second, the choice of the substrate is expected to result in similar trends for density and diameter, *i.e.* the areal density should increase for higher chemical potential of adatoms. Beyond the effect of temperature and substrate orientation, prediction of the trends based on material system selection is more complicated. When the seed particle material changes, the seed surface energy, seed-substrate interface energy and chemical potential of adsorbed seed atoms change as well, and the critical nucleus size of seed particles is a function of all of these (Equation 4-2). If surface energies are dominant, lower surface energy metal seed particles, or higher surface energy substrates would result in increased density and smaller diameters. The effect of chemical potential will be such that higher chemical potential of adsorbed atoms would result in smaller critical nucleus size, therefore higher density would be expected.

4.5. Effect of seed deposition duration on nanowire density

Another parameter investigated in this work to control density of self-seeded nanowires is the seed deposition duration. We have varied the seed deposition time between 0 – 60 s while maintaining TMGa flow ratio (0.674 sccm) and temperature (420°C) of seed deposition constant among growths. Following seed deposition, nanowire growth was performed by flowing TMGa at 0.674 sccm and AsH_3 at 3.35 sccm (V/III ratio = 5) at 420°C. These experiments explore a different parameter regime – specifically, lower seed deposition temperatures and lower TMGa flux compared to previously mentioned experiments in sections 4.2 and 4.3 – to extend the understanding of the seed deposition parameters on controlling density and diameter of nanowires. Figure 4.5 shows the SEM images of the resulting nanowire arrays where top-view images (a-d) give information about the areal density and 45° tilt images (e-f) about the nanowire

morphology. By increasing seed deposition duration, nanowire density increases from 15±4 nanowires/μm^2 to 36±2 nanowires/μm^2. These results have two interesting features; first, nanowire growth can be achieved without a seed deposition step, and second, dependence of areal density of nanowires on Ga seed deposition duration is not linear. These features give information about seed formation kinetics at lower seed deposition temperatures.

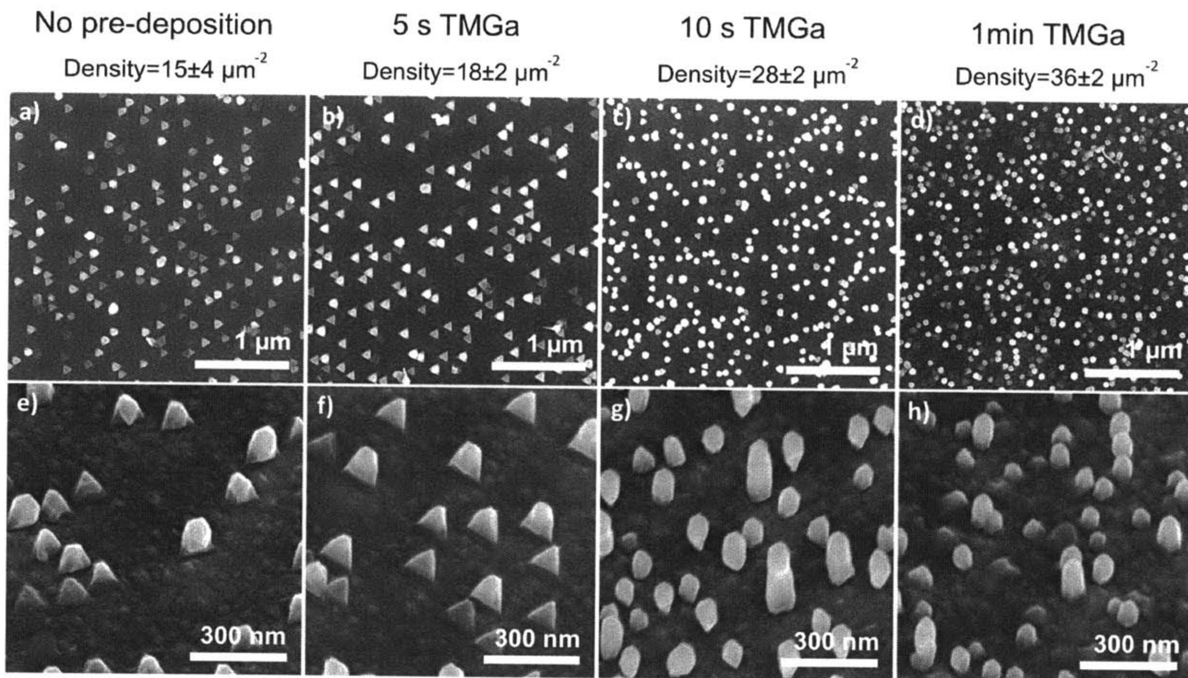

Figure 4.5 Effect of Ga seed deposition duration on GaAs nanowire density. Seed deposition is performed at 420°C with TMGa flow of 0.674 sccm and denoted on the caption for each nanowire growth. Top row shows top-view SEM images nanowires to reveal density, whereas bottom row shows 45°tilt SEM images to reveal the morphology of nanowires. Nanowire growth conditions are the same for all growths, with V/III=5.

We observed that nanowire growth was achieved when seed deposition step is omitted and only nanowire growth step is performed (Figure 4.5 a, e). This implies that at the beginning of nanowire growth, Ga seed formation can occur in the presence of AsH_3 flow and self-seeded nanowire growth can be achieved without a separate seed deposition step. This result indicates a high driving force for nucleation of Ga seed particles under nanowire growth conditions, such as

low temperatures and low V/III ratios compared to thin film growth conditions. In literature, various studies have realized self-seeded III-V nanowire growth without prior seed deposition,[66,80] similar to this result. However, if seed particles are present, such as *ex situ* deposited Au particles, when growth is started by flowing precursors, Ga diffuses into the Au seed particle and does not form separate Ga particles and result in self-seeded nanowire growth. Although self-seeded nanowire growth can be demonstrated in a single step (the nanowire growth step), in this case the control of nanowire diameter and density solely depends on nanowire growth conditions, which offers a limited parameter space to optimize nanowire growth. However, in a two-step growth, separation of seed deposition and nanowire growth steps enables control of density and diameter independent of nanowire growth conditions. Furthermore, this growth underlines the importance of analysis of diameter and density of nanowires rather than seed particles.

The areal density of nanowires increases with Ga seed deposition duration, but this relation is not linear and limits our ability to control density and diameter using seed deposition duration at lower seed deposition temperatures. Areal density of nanowires is 15±4, 18±2, 28±2, and 36±2 nanowires/μm^2 for TMGa deposition (0.674 sccm) of 0, 5, 10, and 60 s, respectively. The major difference occurs between 10 s deposition and 60 s deposition time; while total amount of Ga deposited increases six times, the areal density increases ~1.3 times. Because change in diameter is negligible between the two growths, this suggests that some Ga seed particles do not result in vertical nanowire growth and instead they may result in parasitic thin film growth on the substrate. More experiments need to be performed to understand the exact behavior between deposition duration and areal density. Therefore, our results show that increased duration of Ga

seed deposition may be utilized to increase areal density of nanowires; however we have not established controlled increase of density using seed deposition duration.

Increased seed deposition duration at 420°C alters the density of nanowires with minimal effect on nanowire diameter. Since we assume nanowires grow *via* Ga-seed particle VLS method and nanowire density and diameter depends on the seed density and diameter, this behavior may be explained by continuous nucleation during seed deposition. A larger amount of Ga deposited as a result of increased deposition duration can be distributed in two ways: i) Ga adatoms nucleate new seed particles; continuous nucleation occurs as adatoms arrive to substrate surface resulting in higher density of seed particles with minimal effect on diameter or ii) Ga adatoms join to the existing seed particles; surface diffusion of adatoms to the existing seed particles results in larger diameter particles with smaller effect on density. The probability of these mechanisms depends on temperature – driving force for nucleation decreases with increasing temperature and surface mobility of adatoms increases with increasing temperature according to nucleation theory. (Here we omit very high temperatures where desorption rate is higher than adsorption rate). Therefore, lower temperatures show continuous nucleation behavior during seed deposition due to increased driving force for nucleation and decreased surface mobility of adatoms and we observe increase in nanowire density as a result of increased Ga seed deposition duration.

Finally, we compare the experimental value of areal density of nanowires obtained in this section to extrapolation of nanowire density trend obtained for higher seed deposition temperatures (Figure 4.4). On one hand, experimental data for seed deposition at 420°C for 1 min (Figure 4.5 d, h) show that nanowire density, n, is 36±2 nanowires/μm^2, which estimates Ga adatom diffusion length, λ, to be 83 nm, using relationship $n = 1/(4\lambda^2)$. On the other hand, we can

extrapolate the dependence of the nanowire density on seed deposition temperature (Figure 4.4) to 420°C. Extrapolation of trend in Figure 4.4 to seed deposition temperature of 420°C predicts nanowire density, n = 1.4 nanowires/μm^2 and Ga adatom diffusion length, λ = 430 nm. The two values – experimental and extrapolated density – show that experimental data at 420°C has higher densities than values predicted by extrapolation of high temperature seed deposition density trends, therefore nucleation is enhanced at lower temperatures. This could be explained by increased driving force for nucleation at lower temperatures. As we have explained in the previous paragraph, at seed deposition temperature of 420°C continuous nucleation is observed, suggesting a nucleation-driven regime at this temperature. Whereas surface diffusion would be important for high temperatures due to decreased driving force for nucleation and the trend we observed for seed deposition temperatures between 500°C – 600°C was explained using surface diffusion kinetics. Furthermore, apart from enhanced surface diffusion length at higher temperatures, there is a cooling period where temperature is lowered from seed deposition temperature (500°C – 600°C) to nanowire growth temperature (435°C), that is not performed for seed deposition and nanowire growth at 420°C, which may give sufficient time for Ga surface diffusion. Lastly, it should be noted that TMGa flux would also affect the nucleation and density behavior. Experimental data for seed deposition at 420°C was obtained with a TMGa flux of 0.674 sccm, whereas high temperature seed deposition data is obtained with a TMGa flux of 1.67 sccm. Increased flux would increase nucleation rate; however, at high temperatures nanowire density depends on Ga surface diffusion rather than nucleation kinetics, therefore the effect of TMGa flux may not play a critical role while comparing low and high temperature seed deposition temperatures.

In summary, duration of seed deposition step affects the density of nanowires at low seed deposition temperatures (420°C). While increasing seed deposition duration can increase nanowire density, there is a nonlinear relationship between deposition duration and density and further investigates are necessary to be able to control density as a function of seed deposition duration. It was found that at lower temperatures (420°C) seed formation is nucleation-driven compared to the seed formation that is surface diffusion driven at higher seed deposition temperatures (500°C – 600°C).

4.6. Conclusions

In this chapter, we established nanowire density and diameter control using seed deposition parameters. Varying the seed deposition temperature and substrate orientation controlled the density and diameter of the nanowire arrays. These parameters affect the Ga adatom surface diffusion, Ga adatom chemical potential, and substrate surface energies. By understanding the nucleation kinetics and surface diffusion of Ga adatoms, we demonstrated that higher density and smaller diameter nanowire arrays are achieved by lower seed deposition temperatures or by using (111)A or (110) substrates instead of (111)B substrates. While surface diffusion of Ga adatoms was the main mechanism in the control of density and diameter on GaAs (111)B surface at high seed deposition temperatures, nucleation-driven behavior was observed to be principal mechanism for density-diameter control on GaAs (110) and GaAs (111)A surfaces at high seed deposition conditions, or on GaAs (111)B at low seed deposition temperatures.

Chapter 5: Ternary material system - GaAsP nanowire growth

In this chapter, we demonstrate the self-seeded growth of ternary $GaAs_{1-x}P_x$ nanowires using metal-organic chemical vapor deposition (MOCVD). GaAsP nanowires were grown *via* Ga-seeded growth method, which is described in more details in section 2.1.3. Composition control of $GaAs_{1-x}P_x$ nanowires for $x = 0 - 0.3$ as well as demonstration of GaP nanowires ($x = 1$) was achieved by varying group-V precursor flow percentage. Growth temperature was shown to have minimal effect on the control of nanowire composition, in contrast to analogous thin film growth. Strain in GaAsP nanowires grown on GaAs (111)B substrate was measured using reciprocal space mapping (RSM) in high-resolution x-ray diffraction (XRD) instrument. We found that strain in GaAsP nanowires caused by lattice mismatch with the substrate is released 65% – 100% (fully relaxed). Lastly, optical characterization of as-grown GaAsP nanowires confirmed that the energy bandgap tunability can be successfully achieved through compositional modulations.

5.1. Introduction

Ternary nanowires are of great interest for optoelectronic applications due to their band gap tunability through compositional modulation. Ternary semiconductors (*i.e.* $GaAs_{1-x}P_x$) are alloys of two binary compounds and as such have tunable properties – *e.g.* lattice constant and band gap – that lie between the two binary extremes. In thin films, lattice matching between the substrate and the film is critical for achieving epitaxial growth as their lattice mismatch causes strain, which can be released through formation of defects, when energetically favorable. Due to free

sidewall surfaces, nanowires can accommodate larger lattice mismatch before forming a defect. The ability to effectively relieve strain in nanowires opens up possibilities for growth of heterostructures without the need of buffer layers.

In this chapter, growth of III-V ternary nanowires is examined in the GaAsP nanowire system. GaAsP nanowires are of interest due to band gap tunability between 1.42 eV and 2.26 eV by adjusting the phosphorus content. Tunable band gap of GaAsP nanowires creates opportunities in solar cell heterostructures, for example an optimized dual junction tandem solar cell can be realized by combining two semiconductor materials with band gaps of 1.1 eV and 1.7 eV and achieve theoretical efficiency of 34% at 1 sun AM0 illumination[118,119]. While the choice for material with a band gap of 1.1 eV would be Si, 1.7 eV band gap requirement can be realized by using ternary GaAsP material. Whereas composition control of GaAsP grown by MOCVD has been investigated for thin-films, the effect of growth parameters for P content of self-seeded GaAsP nanowires grown by MOCVD remains an open question.

Growth of ternary nanowires is inherently more complicated than the growth of binary nanowires because different group-V precursors have i) different decomposition rates and ii) different adatom mobilities and sticking coefficients, thus their incorporation rates can vary along the nanowire. It has been shown that these properties can result in compositional variations along the nanowire length and across the nanowire diameter in Au-seeded AlGaAs nanowires; however, by elucidating the incorporation mechanism, control of nanowire composition and morphology was achieved. Similar compositional differences along the diameter and length were observed in GaAsP nanowires grown by MOCVD[120] and molecular beam epitaxy (MBE)[121]. For example, spontaneous formation of core-shell morphology was observed for GaAsP nanowires with P-enriched core compared to As-enriched shell[120]. This was attributed to the higher PH_3

decomposition around Au seed, therefore higher vapor concentration around the seed particle that is available for vapor-liquid-solid growth of the core compared to vapor-solid growth of the shell. In general, nonlinear incorporation as a function of precursor ratio has been observed for GaAsP nanowire growth[122–124], similar to the thin film growth of this system[125].

To present, self-seeded growth of ternary GaAsP nanowires has been mainly studied using solid source MBE[6,123]. In these reports, it was shown that incorporation of group V elements exhibits different trends in nanowire *vs.* thin film growths. These studies indicate that self-seeded ternary nanowire growth requires in-depth understanding of the growth parameters and their effects on the decomposition of precursors, adsorption/desorption kinetics, competing growth mechanisms (vapor-liquid-solid (VLS) nanowire growth *vs.* vapor-solid (VS) sidewall deposition), dynamics of material incorporation to the seed particle and material extraction from the seed particle.

Our objective in this chapter is to gain general knowledge of composition control in self-seeded ternary III-V nanowire growth using MOCVD. We investigate the effect of growth parameters, such as group-V precursor flow percentage and growth temperature, on composition control in GaAsP material system. Furthermore, through the use of techniques such as energy dispersive x-ray spectroscopy (EDS) and reciprocal space mapping in high-resolution x-ray diffractometer we analyzed compositional homogeneity of nanowires and studied the strain relaxation of lattice-mismatched interface. The techniques developed in this chapter can be extended to other self-seeded nanowire growth of III-V ternary material systems..

5.2. Self-seeded GaAsP nanowire growth

Self-seeded GaAsP nanowire growth is schematically shown in Figure 5.1 and it follows a similar process to the growth of binary GaAs nanowires described in 0. Growth procedure starts

with *in situ* Ga seed deposition by flowing trimethylgallium (TMGa) at high temperatures (600°C) for 1 min. During this process TMGa decomposes into gallium and forms seed droplets on the GaAs substrate. Following this step, nanowire growth is achieved at the growth temperature of 450°C – 500°C in two consecutive steps: (i) a GaAs stem is grown for a short period by flowing TMGa and arsine (AsH_3), (ii) GaAsP nanowire is then grown by flowing TMGa, AsH_3, and phosphine (PH_3). GaAs stem is grown to increase vertical alignment of GaAsP nanowires. During the growth, Ga, As and P are incorporated through the seed particle or from the seed particle/nanowire interface. GaAsP nucleates at the seed particle/nanowire interface and precursors are extracted from the seed particle during nucleation and growth of GaAsP layer. The balance of Ga incorporation into the seed particle and extraction out of the seed particle affects the seed particle volume, which determines the nanowire diameter.

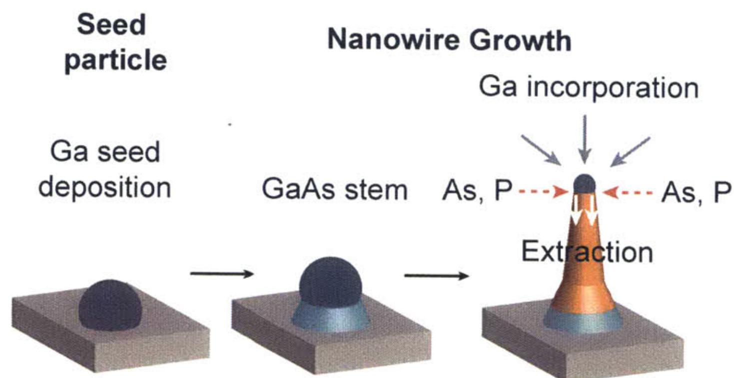

Figure 5.1 Schematic of GaAsP nanowire growth. First, Ga seed particles are *in situ* deposited on the substrate by flowing TMGa at higher temperatures (left). Then, at the nanowire growth temperature, GaAs stem is nucleated by flowing TMGa and AsH_3. (middle). Introduction of GaAs stem was found essential to increase yield of vertical GaAsP nanowire growth. Then, GaAsP nanowire growth occurs by flowing TMGa, AsH_3 and PH_3. Ga incorporates into the seed particle during growth, and then extracted at the seed/nanowire interface as a result of GaAsP layer nucleation. The balance of Ga incorporation and extraction dictates seed volume, hence nanowire diameter.

To alter the composition of the resulting GaAsP nanowires, the percentage of PH_3 within the group V precursor flow (Q_{PH3} / (Q_{PH3} + Q_{AsH3}) %) was varied between 50% - 100%, where Q_{PH3}

denotes the volumetric flow rate of PH_3 in sccm. The flow percentage, growth duration, and flow rates for different growths are given in Table 5-1. During the GaAs stem growth, TMGa and AsH_3 flow rates were 1.67 sccm and 8.49 sccm, respectively, resulting in a V/III ratio of 5. During GaAsP nanowire growth, total group V flow was kept constant with a V/III of ~10. We note that although the nominal V/III ratio is maintained, the decomposition of precursors dictates the effective V/III ratio. Since PH_3 decomposition is less efficient than that of AsH_3, it is expected that at high PH_3 flow percentages the amount of decomposed group V material would be lower resulting in a smaller effective V/III ratio. Upon change of the flow percentage, GaAsP nanowire growth time is increased to ensure nanowires are fully grown. We explored the region between 50-100% PH_3 flow percentage because PH_3 is known to incorporate with a lower efficiency than AsH_3 in thin film and nanowire growths[124,125].

Table 5-1 Growth conditions for GaAsP nanowires of varying PH_3 percentage flows. Flow percentage is PH_3 ranges 50% - 100% by keeping the total group-V flow, thus V/III ratio the same (~10). Growth time of GaAsP is adjusted to ensure fully grown nanowires.

PH_3 %	GaAs stem growth time (min)	GaAsP nanowire growth time (min)	TMGa flow (sccm)	AsH_3 flow (sccm)	PH_3 flow (sccm)
50	1.5	3.5	1.67	8.5	8.8
70	2	3.5	1.67	5.36	12.4
80	2	5	1.67	3.35	13.4
90	2	10	1.67	1.68	15.2
95	1.5	10	1.67	0.8	16.3
98	2	10	1.67	0.35	16.4
100	2	10	1.67	-	16.7

SEM images of the nanowire growths specified in Table 5-1 are given in Figure 5.2. These nanowires were grown with the same seed deposition conditions (TMGa flow rate of 1.67 sccm

for 1 min at 600°C) and at the same growth temperature (450°C). As we discuss in details later on, we successfully controlled the composition of ternary nanowires *via* PH_3 %; we also note that the PH_3 % also affects the nucleation and morphology of nanowires, where vertical nanowire nucleation is decreases and kinking of nanowires is increased, especially for very high PH_3 % ($\geq$ 95%).

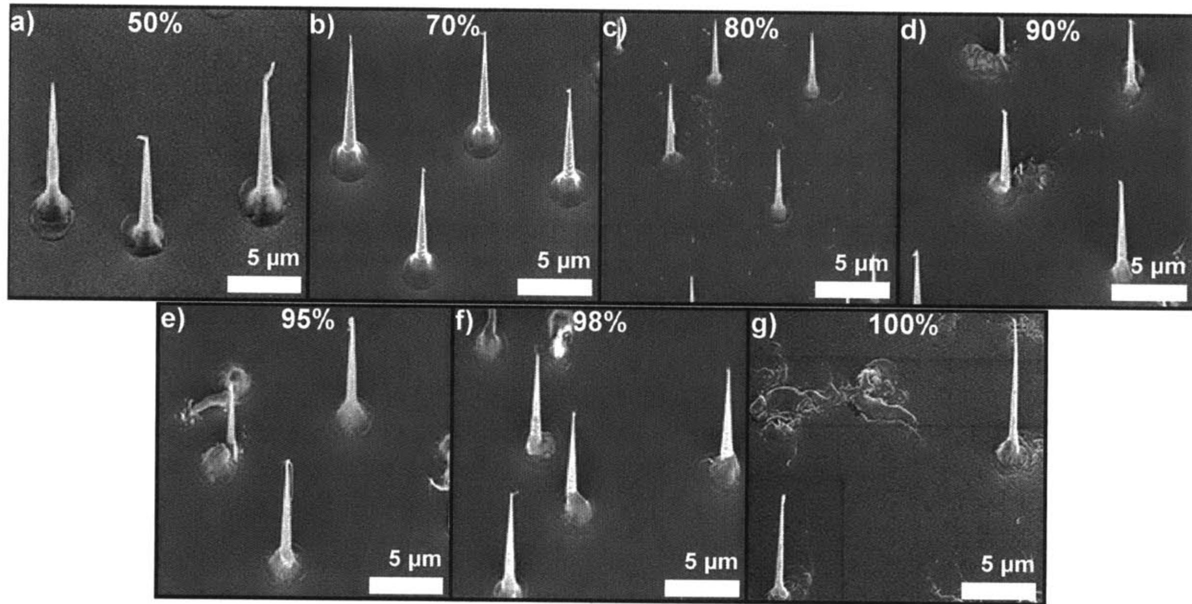

Figure 5.2 GaAsP nanowire morphology as a function of PH_3 %. (a-g) SEM images taken at 45°tilt show the morphology of nanowires, where PH_3% for each growth is given at the top of each image. Vertical nanowire nucleation yield decreases with increasing PH_3%.

We expect the nucleation and morphology of nanowires to be affected by the addition of PH_3 since the chemical potentials, surface energies and lattice mismatch of nanowire change compared to binary GaAs nanowires. As PH_3 % is increased in Figure 5.2, the most prominent morphological change occurs in the base of the nanowires. The seed particle surface energy and chemical potential are altered when switching from GaAs to GaAsP growth. This alteration can cause instability of the seed particle on the nanowire base and cause non-vertical growth at the base. Note that the base of nanowires starts with GaAs stem growth; however, the rest of the

base can be GaAsP due to slower growth rate at the base compared to nanowire. In fact, for 1.5 min GaAs stem growth followed by the growth of GaAsP, using cathodoluminescence we observed that the base emits light in the spectral region corresponding to GaAsP (see section 5.5). Therefore, while switching from GaAs to GaAsP, lattice mismatch could be another reason for decreased morphological quality of nanowire bases with increased PH_3 %. As the composition of ternary nanowires increases in P content, the lattice mismatch between GaAsP and GaAs increases, causing strain at the interface. This strain would alter the nucleation of the new layers at the base of nanowires. Finally, during the switch of GaAs to GaAsP, there is a short (10-40 s) pause during which all precursor flows are stopped and resumed with new values for GaAsP. In general, these interventions may cause instability at the seed particle and cause morphological issues such as kinking. We note that in the extreme case where growth is changed from GaAs to GaP, nanowire growth is still observed. However, nanowire nucleation rate decreases, meaning every Ga seed cannot evolve into a nanowire.

Next, the nanowire growth temperature was modulated to investigate its effect on nanowire morphology and composition. At each growth temperature (450°C, 475°C and 500°C), GaAsP nanowires were grown with PH_3 flow percentages of 70%, 90% or 98%. Morphology of nanowires depends on both growth temperatures and PH_3 %, as observed from Figure 5.3. Above 70% PH_3 flow, nanowire nucleation rate decreases with increasing PH_3 %, resulting in the fact that not every Ga seed evolves into a nanowire. Since the chemical potentials and surface energies of nanowire change when switching from binary GaAs to ternary GaAsP nanowire growth, nucleation of nanowires can be affected by addition of phosphine into the growth. Furthermore, when the growth temperature is increased, the nanowire morphology is also affected. Apart from effects on the base of nanowires, we observe higher rates of kinking along

the nanowires for a given PH_3 % with increasing growth temperature. This can be explained by seed particle instability at higher growth temperatures during nanowire growth. The adverse effects of high growth temperature and high PH_3 % on morphology of nanowires are prominent on Figure 5.3-f), h) and i). Improved morphology of GaAsP nanowires can be achieved by lowering PH_3 % at lower growth temperatures with sufficient GaAs stem growth duration.

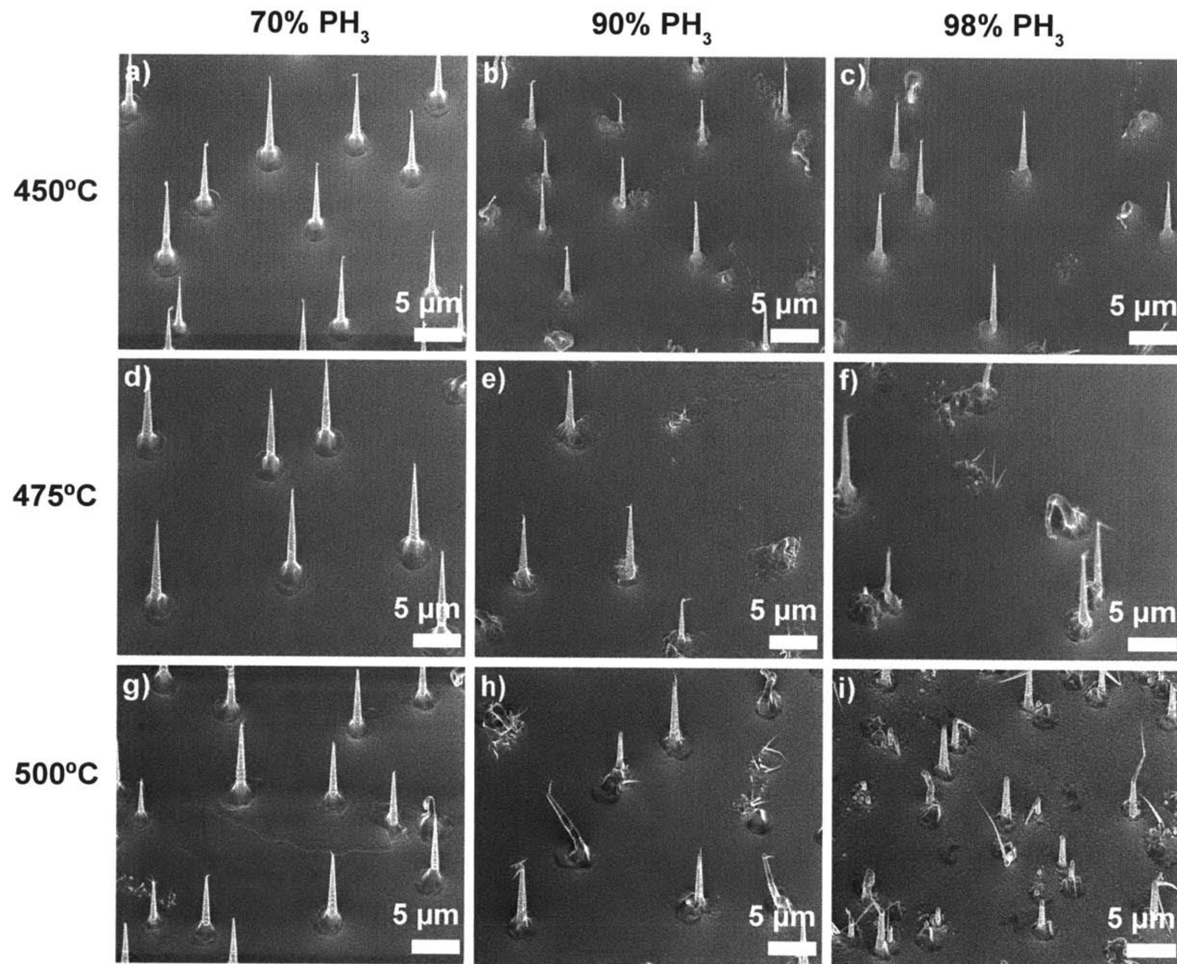

Figure 5.3 Effect of PH_3% and growth temperature on GaAsP nanowires. SEM images taken at 45°tilt shows the morphology of GaAsP nanowires grown at 450°C (a-c), 475°C (d-f) and 500°C (g-i). PH_3% ranges 70%, 90% and 98% from left to right. Increasing growth temperature and PH_3% results in to lower vertical nanowire yield.

In summary, GaAsP ternary nanowires were grown on GaAs (111)B substrates by changing growth temperature and PH_3 flow percentage. We observe that the growth conditions affect the

morphology of nanowires, and lower growth temperature (*i.e.* 450°C) can be effective in improving morphological quality and higher vertical nanowire yield. GaAs stem growth duration is also an important factor to increase vertical yield of nanowires, such that longer GaAs stem can increase the Ga droplet stability while switching to GaAsP nanowire growth.

5.3. Composition control using group V flow percentage and growth temperature

The composition of ternary nanowires (*i.e.* x in $GaAs_{1-x}P_x$ nanowires) can be modulated by growth parameters. In the previous section, we analyzed the morphological properties of nanowires grown with varying PH_3 % and growth temperature and confirmed that nanowire growth can be achieved within parameter range of 50% - 100% PH_3 flow percentage at 450°C – 500°C growth temperature. In this section, we investigate the effect of P precursor flow and nanowire growth temperature on the resulting nanowire composition. We observe that GaAsP nanowire composition can be controlled up to 30% P incorporation (between GaAs – $GaAs_{0.7}P_{0.3}$), as well as GaP nanowires can be grown on GaAs (111)B substrate.

To determine relationship between P content and growth parameters, a series of experiments with varying PH_3 flow percentage and growth temperature has been conducted. The composition of nanowires was measured using energy dispersive x-ray spectroscopy (EDS) coupled with transmission electron microscopy (TEM). Composition values are shown in Figure 5.4. EDS results confirm that P content increases as PH_3 flow percentage increases, as expected; however, growth temperature has little effect on composition of nanowires. At the growth temperature of 450°C, we observe that P content is less than 0.012 (1.2%) when the group V precursor mixture contains 50% of PH_3. Furthermore, P content increases nonlinearly with increasing PH_3 flow percentage. At 90%, 95% and 98% PH_3 flow percentages, the P content of nanowire is

0.10±0.01, 0.18±0.03 and 0.29±0.02, respectively. Even though 98% PH_3 flow percentage results in $GaAs_{0.7}P_{0.3}$, it is possible to achieve almost pure GaP ($GaAs_{0.03}P_{0.97}$) when 100% PH_3 is flown during nanowire growth. Therefore, we have shown that (1) GaAsP nanowires can be grown between GaAs – $GaAs_{0.7}P_{0.3}$ with good morphology and composition control at growth temperature of 450°C and (2) GaP nanowires can be grown on GaAs substrate, albeit vertical nanowire yield is low and growth conditions require further optimization for GaP nanowires.

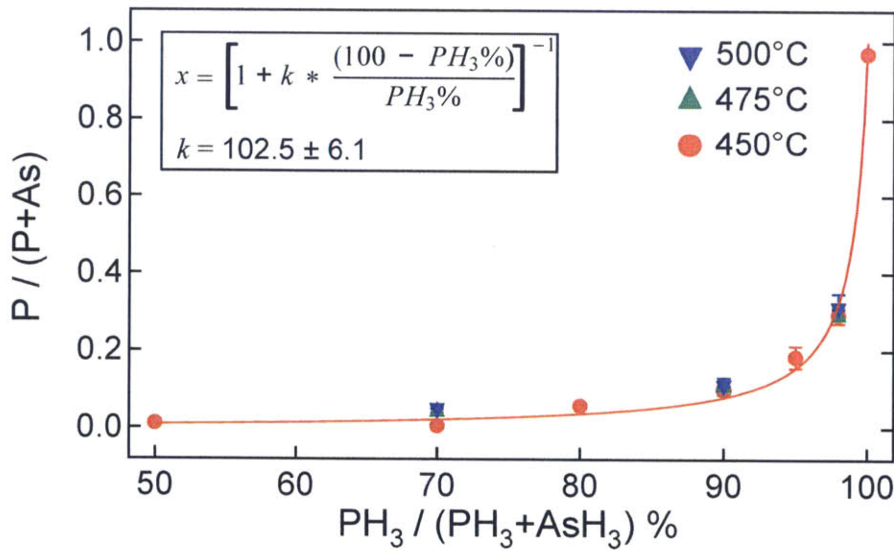

Figure 5.4 Composition of GaAsP nanowires as a function of the group V precursor composition. Composition is determined by quantification and averaging of tens of EDS-TEM point spectra for each growth. P content increases with increasing PH_3 flow percentage. Growth temperature does not affect composition of nanowires. The trend of composition (*x*) as a function of PH_3% can be fitted to an equation shown in the inset with a parameter *k*, which represents incorporation ratio.

The composition of nanowires as a function of the precursor flow composition can be described using the following expression, similar to studies of thin films[125,126]:

$$\frac{x}{1-x} = \frac{\beta * Q_{PH_3}}{\alpha * Q_{AsH_3}} = \frac{1}{k} * \frac{Q_{PH_3}}{Q_{AsH_3}}$$

Equation 5-1

Here, x represents the composition of the $GaAs_{1-x}P_x$ nanowire, Q_{PH3} and Q_{AsH3} represents the flow rates of precursors in sccm, and α and β are incorporation coefficients for As and P, respectively. To represent the equation as a function of P content and PH_3 flow percentage only, P content is replaced with x, As content by $1-x$, and PH_3 flow rate is replaced with PH_3 flow percentage (Q_{PH3} / (Q_{PH3} + Q_{AsH3}) %) and AsH_3 flow rate replaced with AsH_3 flow percentage (100 – PH_3 %). Rearranging the equation, we get:

$$x = \left[1 + k * \frac{(100 - PH_3\%)}{PH_3\%}\right]^{-1}$$

Equation 5-2

where $k = \alpha/\beta$ represents the ratio of incorporation coefficient for As and P (incorporation coefficient ratio). We fit the experimental data to this equation and find the fit parameter, k = 102.5±6.1. This result indicates that the incorporation of As is 102 times more likely than P when AsH_3 and PH_3 are provided as precursors.

Incorporation coefficients represent all of the processes that the gas phase hydride sources (AsH_3 and PH_3) experience until they are incorporated into GaAsP. These processes are surface- and gas-phase-reaction of the hydride source decomposition, adsorption/desorption of adatoms, and nucleation of GaAsP layers under the seed particle. Due to presence of the seed particle, some of these processes are different than for thin film growth of III-V ternary materials. For example, decomposition of precursors is different on a solid surface (substrate) compared to liquid surface (seed particle) and this is reflected in the incorporation coefficient. For self-seeded nanowire growth between 450°C – 500°C, we observe that growth temperature does not significantly alter the incorporation coefficient ratio, k (Figure 5.4). This shows that although growth temperature may affect processes such as the kinetics of decomposition and adsorption/desorption, at this growth temperature window, the incorporation efficiency ratio does

not change, possibly due to the fact that temperature dependences of many of these processes cancel out each other, as discussed further below.

The nonlinear incorporation of P as a function of PH_3 flow percentage. Comparing our results to thin film growth studies of GaAsP, we observe similar trend of nonlinear incorporation of phosphorus as a function of precursor flow percentage for a given growth temperature (Figure 5.5). P content of thin films was fitted with the same equation to the experimental thin film growth data[125,126], however, resulting in a different incorporation coefficient ratio, k (Equation 5-1 and Equation 5-2). The incorporation coefficient ratio of As over P, k, found in thin film studies varies as a function of temperature and is generally lower than the nanowire value of ~102 (see Table 5-2), but higher than unity. As a result, for a given flow composition, P content is higher in thin films than in nanowires (*i.e.* at 80% PH_3, P content of $GaAs_{1-x}P_x$ is $x = 0.21$ for thin films grown at 650°C, whereas $x = 0.09$ for nanowires grown between 450°C – 500°C). It should be noted that in both thin film growth and nanowire growth, the incorporation of As is more efficient than P for a given precursor ratio (k values are higher than unity in Table 5-2). Therefore, we observe that ternary GaAsP nanowire growth qualitatively follows a similar trend to thin film growth where As incorporation is more efficient than P incorporation.

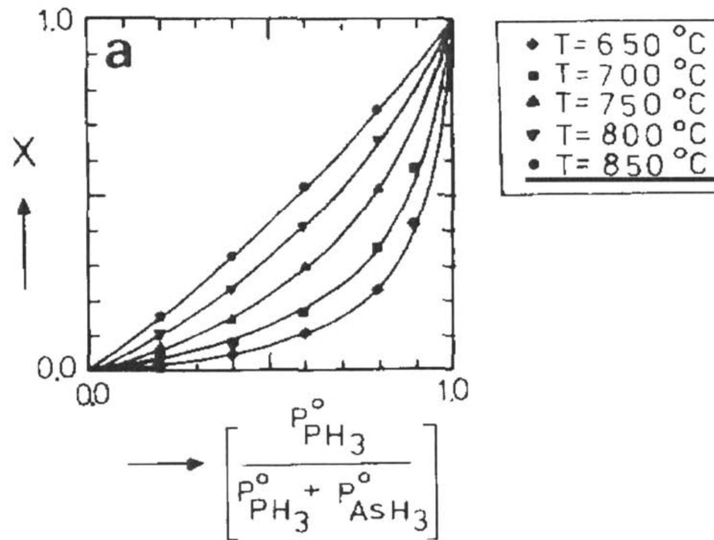

Figure 5.5 $GaAs_{1-x}P_x$ thin film growth. Phosphorus content of thin film (x) as a function of the input phosphine ratio for growth temperatures between 650 - 850°C. Adapted from Smeets.[126]

Effect of growth temperature on composition. The fact that we do not observe effects of the growth temperature on the composition of nanowires is unique to the nanowire growth. In GaAsP thin film studies, a strong growth temperature dependence of P incorporation was observed for growth temperatures between 650 – 850 °C[125,127]. For thin film growth by MOCVD, incorporation efficiency of PH_3 increases with increasing growth temperature[125,127] (incorporation coefficient of As over P, k, decreases), whereas for self-seeded nanowire growth incorporation coefficient ratio is constant. The increase of P incorporation coefficient with temperature has been attributed to the thermally activated processes of decomposition of PH_3 over the growth temperature range[126,128] and adsorption and desorption kinetics and processes[125,129] in thin film growth.

Using the temperature dependence of P incorporation during thin film growth, we extrapolate incorporation coefficient ratio for the growth temperatures of self-seeded nanowires. It should be

noted that the temperature dependence of P incorporation in thin film growth $\beta/\alpha = 1/k$ is proportional to $\exp(-E_A/kT)$ where $E_A = 1.0 \pm 0.1$ eV between growth temperatures of 650 – 850 °C[125]. Using this data, we estimate the incorporation coefficient for various temperatures below this range in Table 5-2. If nanowire growth had the same growth mechanism as thin film growth, the expected incorporation coefficient of As over P, k, would be between 165 – 483 for the growth between 450-500°C. However, the value $k = 102.5$ obtained from our measurements shows that nanowire growth kinetics is different than the thin film growth such that P incorporation is enhanced for these growth temperatures. The factors that cause temperature dependence of P incorporation for thin film growth were attributed to PH_3 decomposition rate and adsorption/desorption kinetics (note that at the thin film growth temperatures AsH_3 decomposition is complete[104,130,131]). While these factors would still be relevant for nanowire growth, it should be noted that at nanowire growth temperatures, AsH_3 decomposition rate is thermally activated and lower percentage of AsH_3 decomposes at nanowire growth temperatures compared to complete decomposition at thin film growth temperatures, which could be the reason for stagnant incorporation ratio at these temperatures.

Table 5-2 Incorporation coefficient values (k) for thin film growth experiments[125] (left column) is extrapolated to lower growth temperature ranges where nanowire growth is generally performed.

	T (°C)	$k = \alpha / \beta$		T (°C)	$k = \alpha / \beta$
Experimental data[125]	650	12.99	Extrapolation to lower growth temperatures	450	483.77
	700	7.14		475	277.61
	750	3.57		500	165.13
	800	2.08		550	64.23
	850	1.33		600	27.84

Homogeneity of composition within nanowires. The distribution of P within single GaAsP nanowires has been investigated with EDS in STEM using point measurements, linescans, and elemental maps. Point measurements have confirmed fairly homogenous distribution in the nanowire along the length and diameter within ±5% (Figure 5.6). It should be noted that the sensitivity of EDS detector is about 1-2%, which could affect the precision and increase standard deviation. While some of the inhomogeneity may be attributed to the limitations of measurement method, other reasons could be local availability of precursors as the nanowire growth progresses. Depending on the local variations of precursors, the incorporation kinetics may be different such that the P content could be affected along the length of nanowires.

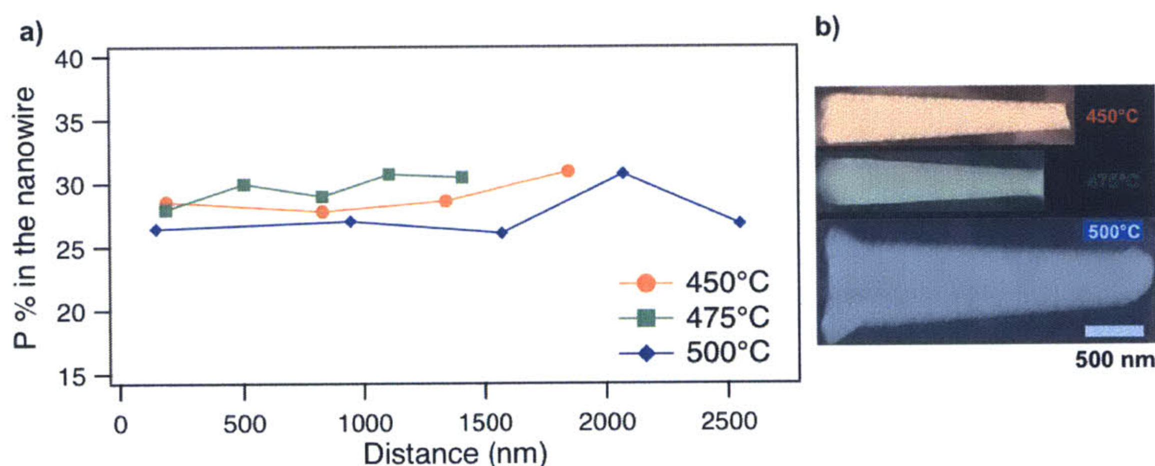

Figure 5.6 Compositional homogeneity along the length of GaAsP nanowires. a) Phosphorus distribution along the nanowire length for different growth temperatures, given in percentage, and b) artificially-colored dark-field STEM images. These nanowires are grown with 98% PH_3 flow percentage; scale bar is the same for all nanowires shown in (b).

Compositional homogeneity along nanowire diameter was investigated *via* EDS linescans qualitatively. In Figure 5.7, we show nanowires grown with the highest PH_3 flow percentage (98%) and corresponding EDS linescans for different growth temperatures. Because overall composition of GaAsP nanowires has 50% group-III element (Ga) and 50% group-V elements

(As and P), Ga composition is constant at every point in the nanowire, thus intensity of EDS signal for Ga is dependent on Ga amount and reflects the thickness of nanowire along the line scan (yellow line in dark field STEM images in Figure 5.7).The homogeneity of P can be deduced by comparing P intensity to Ga and As intensities of the EDS signal. For growth temperatures of 450°C and 475°C, we observe that intensity of the EDS signal for P follows a similar profile to Ga and As intensities (Figure 5.7 a, b), meaning that P content is homogenous in these nanowires and there is no discrete change in P composition along the linescan. For growth temperature of 500°C, P intensity of the EDS signal shows some inhomogeneity, P intensity does not follow Ga intensity in linescan position around 400 nm. The increase of P intensity is accompanied with a small dip in As intensity suggesting a larger P content on the right hand side of nanowire towards the edge. It should be noted that these intensity profiles of the EDS signal are raw data; to quantify the composition one should consider the relative x-ray emission efficiency of elements and thickness of the material for the absorption of x-ray emission. However, even without quantification, it is possible to comment on the unintentional shell deposition by looking at discrete changes near the periphery of nanowire diameter. In the case of 500°C growth temperature, P distribution profile is not monotonic, suggesting a non-uniform core-shell type distribution of P content. It should be noted that at the growth temperature of 500°C, the nanowire morphology is also affected as the optimal growth conditions is not achieved. This could alter the local precursor availability and may create this inhomogeneity.

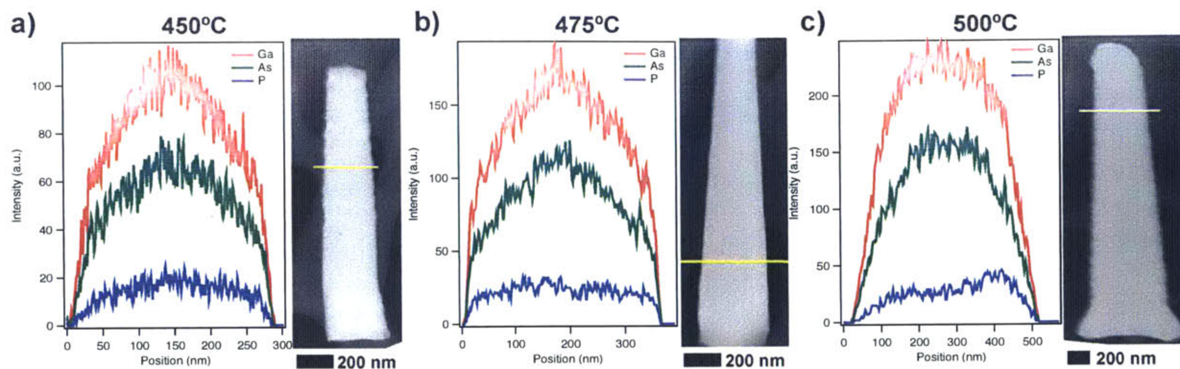

Figure 5.7 EDS linescans and corresponding dark-field STEM images showing elemental distributions along nanowire diameter for growths performed with 98% PH_3 flow at different growth temperatures (labeled for each figure). EDS intensity is shown in red, green and blue for Ga, As and P, respectively (a-c, images on the left). Linescan locations are given by yellow line on the dark-field STEM images (a-c, images on the right).

The P distribution along the diameter may show discrete changes due to unintentional shell deposition during nanowire growth at high growth temperatures. Unintentional shell deposition was observed for Au-seeded GaAsP nanowire growths[45,120,121] and is explained by radial growth *via* vapor-solid (VS) growth mechanism at higher temperatures, where precursors decompose on the nanowire sidewalls and deposition occurs on the nanowire sidewalls. This mode of growth is named vapor-solid referring to the fact that vapor precursors incorporate to solid directly in contrast to vapor-liquid-solid growth where gas precursors decompose and alloy/diffuse through seed particle or seed/nanowire interface and deposit solid layers. Two growth modes lead to different incorporation ratio of competing group V elements during ternary nanowire growth; therefore P content could be different in the VLS-grown core compared to VS-grown unintentional shell. VS growth mechanism is pronounced at high temperatures where thermally activated processes such as precursor decomposition and nucleation can occur at a higher probability without the necessity of a seed particle.

Overall, we have shown that GaAsP nanowires have homogenous composition along their length and diameter for lower growth temperatures of 450°C and 475°C.

5.4. Strain and composition measured by x-ray diffraction

A common method to determine composition and strain state of epitaxially grown ternary semiconductors is reciprocal space mapping (RSM) in an x-ray diffractometer (XRD). Lattice parameter of a ternary semiconductor is a function of its composition; however, epitaxial growth exerts in-plane biaxial strain due to lattice mismatch and distorts the crystal structure, thus lattice parameter in normal and plane direction changes. Diffraction spot from a crystal plane will have a different position for GaAs substrate and GaAsP nanowire and difference in position of diffraction spot for a plane that is not normal to growth direction (asymmetrical reflection) is dependent on composition and strain state of GaAsP nanowire. Working principle of this method and calculation of composition and strain from RSM are described in 2.2.4. The advantage of RSM over EDS-TEM (section 5.3) for composition determination is sample size – nanowire composition is calculated from a large area (in the order of mm^2), therefore statistically more significant average composition can be obtained. Furthermore, RSM uses nanowires that are still attached to the substrate and provides information on the strain state of GaAs/GaAsP interface. The RSM method is commonly used in thin film growth to determine the composition and relaxation of the films; here we apply this method to nanowires to get insight about relaxation of nanowires as well as the applicability of this method for nanowire composition determination.

Collection of RSM maps and analysis was performed as follows: first coupled 2theta (2θ)/omega (ω) scans that varies over omega values (relative omega) are collected. Intensity profile of each coupled scan is combined together to create a map. Then, these maps are converted to $q_x - q_z$ maps. Using the peak information data in the RSM, the lattice mismatch of nanowire and substrate is found and composition of nanowires is calculated. In these experiments, we collected (422) asymmetrical reflection to gain information about lattice spacing

and strain simultaneously using a grazing incidence condition that is surface-sensitive. (see 2.2.4 for more detailed description).

2theta/omega maps were collected for GaAsP nanowires on GaAs substrate to observe the effect of growth conditions on lattice spacing, which reflects the composition of $GaAs_{1-x}P_x$ nanowires. In Figure 5.8, we observe the effect of group V precursor percentage on lattice spacing, where nanowires grown at the same growth temperature of 450°C with different $PH_3/(PH_3+AsH_3)$% are shown. The strong peak at ~83.7° 2θ belongs to GaAs substrate, while GaAsP peak partially overlaps with GaAs substrate peak at 70% and 80% PH_3 (Figure 5.8 a-b) and separates as a distinct peak after 90% PH_3(Figure 5.8 c-e). GaAsP peak is observed at higher 2theta values due to smaller lattice constant of GaAsP than GaAs. Therefore, the lattice spacing of (422) crystal planes in GaAsP is getting smaller with increasing PH_3 percentage as the P content of nanowires increases.

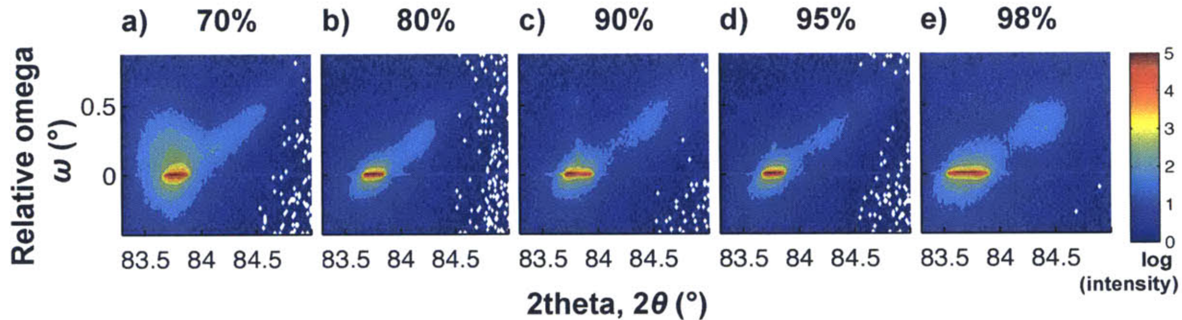

Figure 5.8 2theta-omega diffraction maps shown for (422) reflections coming from GaAsP nanowires and GaAs (111)B substrate. We qualitatively investigate the shift of (422) peak coming from GaAsP nanowire as a function of PH_3 percentage during growth (top right turquoise spot in images is GaAsP reflection, below 90% PH_3 the spot for GaAsP nanowire overlaps with GaAs spot). All nanowires are grown at 450°C.

Apart from the effect of PH_3 percentage on the lattice spacing, we also investigated the effect of growth temperature on nanowire structure. The growth temperature affects the growth kinetics and may alter the incorporation of group V atoms, which would alter the composition of

nanowires. This compositional change, in turn, results in a change in the lattice spacing that can be detected by XRD. Figure 5.9 shows the 2theta/omega maps of GaAsP nanowires grown with different growth conditions (growth temperature and PH_3 flow percentage). The strong peak at ~83.7° belongs to the GaAs substrate, whereas the weaker peak at higher wavelengths belongs to GaAsP nanowires. The peak position of GaAsP nanowires changes as a function of growth conditions, showing that the lattice constant of the nanowires, thus composition, is changing. For each growth temperature, the effect of PH_3 percentage exhibits a similar trend, where GaAsP peak position is observed at higher 2θ and higher relative ω with increasing PH_3 percentage. On the other hand, for a given PH_3 percentage, the growth temperature does not have a clear effect on the peak position, such that GaAsP peak position is observed at higher 2θ and higher relative ω when temperature is increased from 450°C to 475°C, however GaAsP peak is at lower 2θ and lower relative ω position when temperature is increased from 475°C to 500°C.

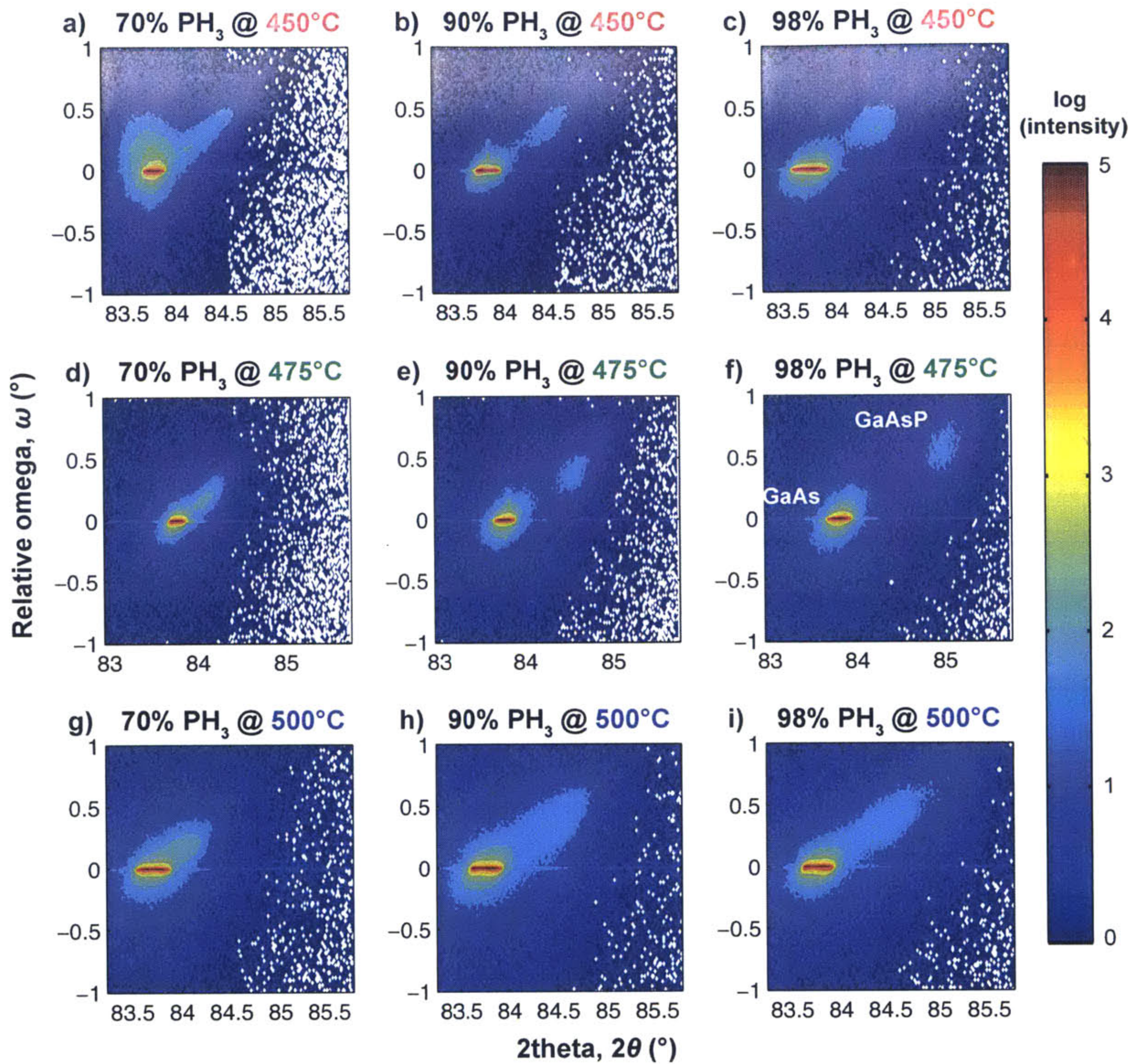

Figure 5.9 Effect of growth temperature and PH_3% on P composition, deduced from 2theta-omega diffraction maps. Growth conditions are given at the label of each image. (422) reflections coming from GaAsP nanowires and GaAs (111)B substrate are labeled in figure (f). GaAsP peak shifts in 2theta and omega, showing the changes in lattice spacing as a result of compositional changes.

In Figure 5.9, certain features of RSM present challenges in composition quantification. GaAsP nanowires grown with 70% PH_3 exhibit a peak that is close to the GaAs substrate peak, complicating the peak shift analysis for this growth condition. For growth temperatures of 450°C and 475°C at 90% and 98% PH_3 flow percentage, GaAsP nanowires exhibit a separate peak, but

at 500°C it broadens. The broadening of the peak at 500°C could be a result of the inhomogeneous composition and the lattice spacing. In fact, as shown in section 5.3, we observed P inhomogeneity for nanowires grown at 500°C using EDS. Apart from a broader peak, the GaAsP peak position is observed at lower 2θ and lower relative ω position when temperature is increased from 475°C to 500°C, suggesting at this growth temperature, the composition of GaAsP nanowire has a lower P content than nanowires grown at 475°C.

Using these two peak positions (2theta values) in Figure 5.9, it is possible to calculate the lattice spacing, *d*, *via* Bragg's law; however, the calculated value does not relate directly to the lattice constant (therefore composition) due to distortion of the lattice as a result of the lattice mismatch. Epitaxial growth of GaAsP on GaAs results in lattice mismatch strain, and can be defined as biaxial isotropic in-plane strain, with zero stress along the growth direction, and zero shear strain at the interface. For cubic materials, elastic theory under biaxial strain dictates the relationship between strains in plane (ε_{xx}) and normal directions (ε_{zz}) as follows:

$$\varepsilon_{zz} = -\frac{2\nu}{1-\nu}\varepsilon_{xx}$$

Equation 5-3

where ν is Poisson's ratio along <111> direction (growth direction). Once the lattice constants of the strained nanowire at lateral and normal directions are found, they can be related to the strain in those directions and Equation 5-3 can be numerically solved for composition, x (see 2.2.4 for more detailed description).

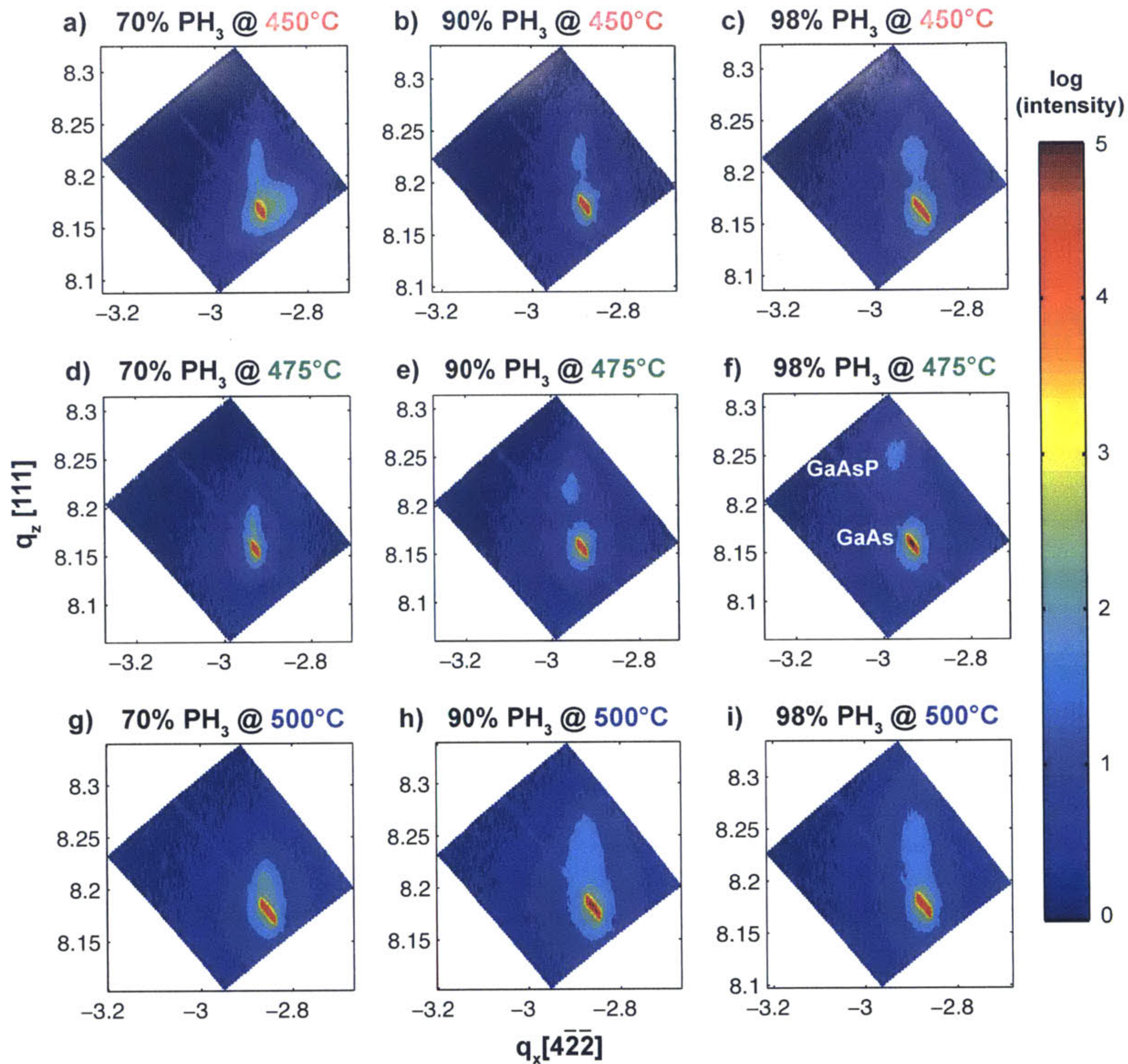

Figure 5.10 RSM ($q_x - q_z$ maps) of (422) reflection of GaAsP nanowires grown on GaAs (111) substrates under different growth temperature and PH_3% conditions (each image is labeled with the growth conditions). Composition and strain is later calculated using the peak positions of GaAs and GaAsP reflections.

Reciprocal space maps (RSM) of $q_x - q_z$ were calculated by converting 2theta/omega maps using relations given in section 2.2.4 by LEPTOS software. Using the peak information of $q_x - q_z$ RSM, composition and strain of nanowire can be calculated. We plot RSM of GaAsP nanowires grown with different PH_3 flow percentage (70%, 90% and 98%) and growth temperatures

(450°C, 475°C and 500°C) in Figure 5.10. The strong peak at lower q_z values belongs to GaAs substrate, whereas the smaller peak above GaAs peak belongs to GaAsP nanowires, as labeled in Figure 5.10-f. In these maps, we observe that GaAsP reflection is distinct with respect to the substrate, showing different composition and strain states.

Using the peak information (q_x and q_z values), we calculated the composition and relaxation of the nanowires in each map (Figure 5.11). For a given growth temperature, calculation of relaxed lattice parameter indicate that P content increases with increasing PH_3 flow ratio, which is similar to EDS composition determination in section 5.3. An exception is 95% PH3 flow ratio, where the P content exhibits a small decrease for that flow ratio. For a given PH_3 flow ratio, however, the P content trend is different than the one measured by EDS. According to RSM, the P composition increases as the growth temperature is increased from 450°C to 475°C and then decreases for 500°C; whereas according to EDS measurements, P content is the same for different growth temperatures. The observed discrepancy for 500°C might be attributed to the broader GaAsP peak – according to EDS results, we observed inhomogeneity of P content along the nanowire diameter, suggesting higher P content along the circumference compared to the nanowire core. P content inhomogeneity would cause a broader RSM peak due to variations in lattice constant in the nanowire. Because the broad GaAsP peak starts to overlap with GaAs peak, the highest intensity position of broad peak may be shifted and may cause inaccuracy in calculating the average composition of GaAsP nanowires. Also, it should be noted that for 70% PH_3 flow percentage the P composition is around x=0.1 for 450°C and 475°C, which is different than EDS, where P composition was found less than x=0.05, where RSM method may contain inaccuracy due to combined peak of GaAs and GaAsP. In general, composition estimation using

RSM shows a linear dependence on PH_3 flow percentage compared to the nonlinear nature of EDS measurements.

Relaxation data shows that with PH_3 flow percentage, relaxation of GaAsP nanowires generally increases, except at growth temperature of 500°C. Theoretical relaxation values vary between 0 and 1, where fully strained pseudomorphic layer has a relaxation of 0, and fully relaxed layer has a relaxation of 1. The minimum relaxation value of GaAsP nanowires is over 0.65, which means that nanowires are 65% relaxed. This confirms the contribution of relaxation at releasing strain from the sidewalls of the nanowires due to free surfaces. It should be noted that thermal expansion coefficient is not taken into account during calculation of composition and relaxation, even though the nanowires are grown on the substrate at high temperatures and measurement is performed at room temperature. This may induce experimental errors in calculation of composition and relaxation and may result in relaxation values >1.

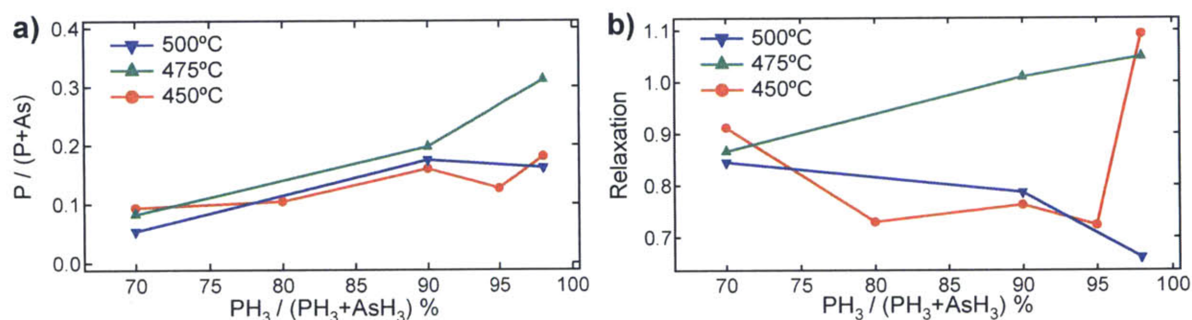

Figure 5.11 a) Composition and b) relaxation of GaAsP nanowires calculated using RSM of (422) reflection by XRD. P content increases with increasing PH_3% during growth, similar to results measured by EDS (a). Relaxation graph shows the relaxation of strain in GaAsP built up due to lattice mismatch between GaAs and GaAsP. Nanowires show over 65% relaxation in all cases; however, a clear trend between growth conditions and relaxation was not observed.

Strain in the GaAsP nanowires is accommodated for an epitaxial growth by means of elastic or plastic deformation. Since nanowires have a large surface area on the sidewalls, most of the strain is expected to accommodate by elastic deformation. The strain state of nanowires is

determined by the relaxation, R, calculated using RSM data. Complimentary techniques may be applied to understand the strain relaxation mechanism.

To confirm that GaAsP peak comes from nanowires, and not from the parasitic growth on the substrate, we designed a control experiment in which nanowires were removed from the substrate and the resulting film was investigated using diffraction, as shown in Figure 5.12. The first row shows the 2theta/omega maps, $q_x - q_z$ maps, and nanowire morphology of GaAsP nanowires on the growth substrate (Figure 5.12 a-c). During nanowire growth, a thin defective layer of parasitic growth can grow on the substrate in addition to nanowires. When nanowires are removed (Figure 5.12 f), 2theta/omega maps, $q_x - q_z$ maps only exhibit GaAs substrate peak (Figure 5.12 d-e). This confirms that GaAsP peak observed in the maps previously results from the nanowires and not from the parasitic thin film growth.

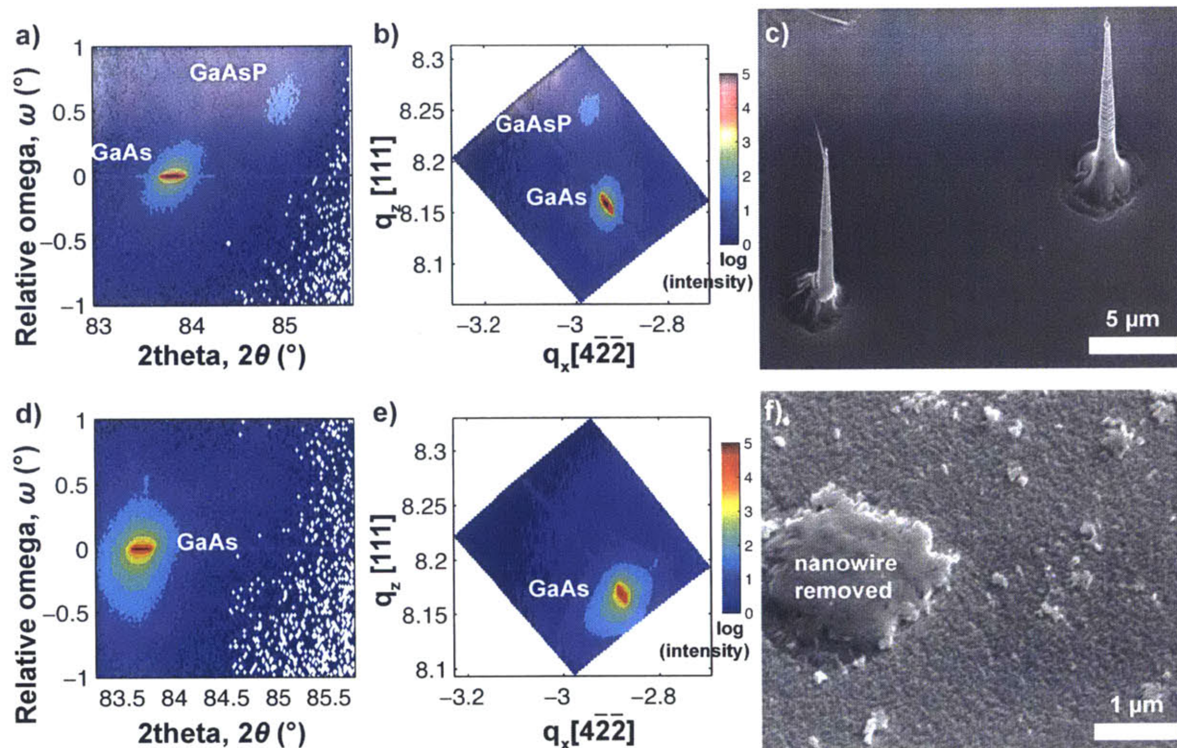

Figure 5.12 The source of GaAsP peak in RSM is nanowires. a, b) RSM is performed on a GaAs substrate that has GaAsP nanowires. c) Corresponding SEM image of sample used to obtain maps in (a, b) is shown. d, e) RSM is performed on a sample, where GaAsP nanowires are removed mechanically. f) Corresponding SEM image of sample used to obtain maps in (d, e). Nanowires are removed but an overgrowth layer is observed. During growth, along with nanowires, a parasitic over-growth occurs on the substrate. By removing the nanowires but keeping the over-growth layer intact, we performed RSM measurement and observed only GaAs peak. Therefore, the over-growth layer does not contribute to the information on RSM and GaAsP peak comes from GaAsP nanowires.

Discussion of discrepancy in composition determination by XRD-RSM and TEM-EDS. In this chapter, we investigated the composition of GaAsP nanowires using two methods: TEM-EDS and XRD-RSM and obtained slightly different results. The discrepancy in measured/calculated P content may rise from the indirect nature of XRD method for composition determination. XRD measures the lattice spacing in the structure and the accuracy of XRD depends on uniformity of lattice spacing. When the lattice spacing is not uniform in the structure, the diffraction peak is broadened and peak information is less accurate. For example, relaxation at the sidewalls may

cause nonuniform strain in the nanowire, therefore nonuniform lattice spacing. Furthermore, inhomogeneity of P content would alter the lattice spacing. Therefore indirect nature of XRD combined with probing a large area with many nanowires may cause imperfect estimations of composition especially for complex nanowire structures where a three dimensional relaxation should be considered. On the other hand, TEM-EDS is a direct method to quantify composition where relative x-ray intensities emitted from each element of nanowire is detected and correlated with the composition in the nanowire. While there are some other parameters to consider for EDS measurements, such as the reabsorption of x-rays within the thickness of the nanowire, the probe size is much smaller and composition information from a small region of a single nanowire can be investigated. From RSM measurement, average composition and relaxation information over a large area is attained.

5.5. Optical properties of GaAsP nanowires

The control of optical properties of nanowires is crucial for integration of nanowires in devices. An important property is the band gap of nanowires that is directly dependent on the composition (in our case, P content) of ternary nanowires. To determine the band gap of the nanowires, cathodoluminesce (CL) coupled with scanning electron microscopy (SEM) was conducted on GaAsP nanowires. The advantage of CL-SEM is that single nanowires can be excited while they are attached to the growth substrate and the band gap of the irradiated region of the single nanowire can be determined.

We investigated GaAsP nanowires grown with 90% PH_3 flow percentage in CL-SEM. Figure 5.13a shows the SEM image of GaAsP nanowires epitaxially grown on GaAs substrates. Panchromatic CL at room temperature reveals a bright emission from the base of nanowires (Figure 5.13b), whereas the rest of the nanowire shows relatively low CL intensity. Point spectra

obtained at 77K both along the nanowire and at the base (Figure 5.13c) confirmed that the base and nanowires consist of GaAsP. However, the emission peak has a lower energy at the base (1.703 eV *vs.* 1.727 eV - 1.731 eV for nanowire regions), which indicates lower P content or in-plane tensile strain at the base due to lattice mismatch compared to relaxed nanowires[132]. We can convert the emission energy to composition assuming relaxed nanowires[133] and find that these nanowires exhibit a P content of 0.157 at the base (*i.e.* $GaAs_{0.843}P_{0.157}$) and $x = 0.176 - 0.180$ at the nanowire, which is higher than the composition determined by EDS, $x = 0.10$ ($GaAs_{0.9}P_{0.1}$).

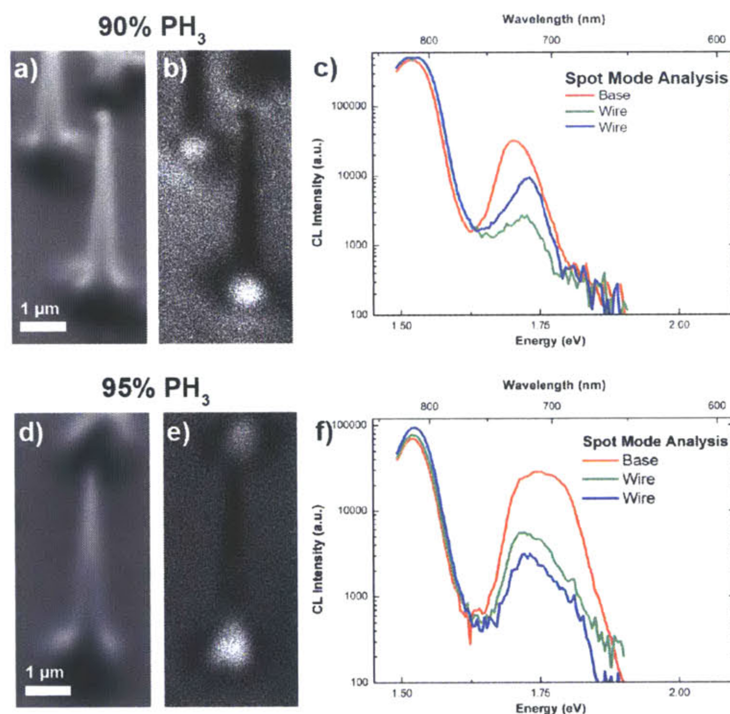

Figure 5.13 Optical properties of GaAsP nanowires measured by CL in SEM. a,d) SEM image, b,e) PanCL image at room temperature and c,f) spot mode analysis at 77K are shown for GaAsP nanowire growths performed with 90% PH_3 (a-c) and 95% PH_3 flow percentage at 450°C.

Furthermore, we investigated GaAsP nanowires grown with 95% PH_3 flow percentage in CL-SEM. SEM image and panchromatic CL images (Figure 5.13d,e) show the nanowire morphology and the corresponding emission at room temperature that again comes from the base

of the nanowire. Analysis of point spectra taken at 77K reveals that the base emission has a larger CL peak width, suggesting that there may be compositional or strain variation at the base. The emission peak at the base can be fitted to two peaks at 1.721 eV and 1.772 eV, corresponding to x = 0.172 and x = 0.213, respectively. Emissions peaks from the two spots on nanowire have peaks both at 1.734 eV, corresponding to x = 0.182. Emissions from nanowire regions agree well with EDS measurements for nanowires grown with 95% PH_3 flow percentage which exhibited composition of $x = 0.18$ ($GaAs_{0.78}P_{0.18}$).

While investigating GaAsP nanowires that are still attached to the growth substrate, the morphological and compositional structure of nanowire nucleation is important to consider. To review the growth process, vertical GaAsP nanowire growth was achieved by growing a few layers of GaAs base firstly, and then GaAsP nanowire growth is started, as described in section 5.2. Therefore, nanowire bases are initiated with GaAs and then switched to GaAsP. The monochromatic CL emission at 720 nm at room temperature (refers to $GaAs_{0.76}P_{0.24}$) confirms that bases are consisting of GaAsP. Even though nanowire morphology is exhibiting kinked growth, the bases of nanowires show bright emission centered at 720 nm, which corresponds to GaAsP composition $x = 0.24$.

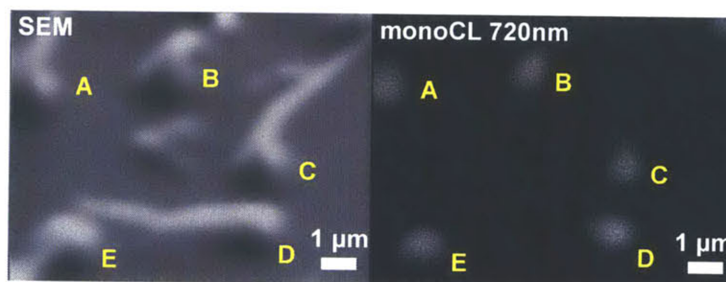

Figure 5.14 Room temperature monochromatic CL (720nm) of GaAsP nanowires on GaAs (111)B substrate grown at 450°C with 95% PH_3 flow percentage. Emission at 720nm would indicate a P composition x = 0.24. Comparing SEM image and monoCL map of corresponding region confirms that nanowire bases consist of GaAsP. Locations of the nanowire bases are labeled for ease of comparison.

CL showed high intensity emission at the base of the nanowires compared to the nanowire itself, as observed in Figure 5.13 and Figure 5.14. This high intensity emission in the base suggests that the base is high quality crystal, free of defects. Furthermore, the surface area at the base is smaller compared to nanowires. The nonradiative recombination rate is larger at the free surfaces; therefore this might be one of the reasons of quenched CL emission at the nanowires. Also, the base is thicker compared to the nanowires, and since the material amount directly relates to CL emission intensity, it is expected that nanowires exhibit lower intensity than nanowires.

5.6. Summary

In this study, we investigate the compositional control of Ga-seeded GaAsP ternary nanowires grown by MOCVD. The effects of the group V precursors percentage (arsine and phosphine) and the growth temperature (450-500°C) on P content in GaAsP nanowires were studied. We observe that P content in nanowires increases nonlinearly with increasing phosphine flow percentage, similar to thin film experiments. However, in contrast to thin-film growth, growth temperature dependence of P incorporation was not observed for nanowires grown between 450-500°C, suggesting that at this growth temperature decomposition of both precursors is kinetically limited. RSM measurements revealed GaAsP nanowires relieves the strain due to lattice mismatch between GaAs and GaAsP to the degree of 65% - 100%. The nanowire base exhibits high intensity cathodoluminescence (CL) emission, indicative of high crystalline quality and therefore elastic accommodation of strain between GaAs substrate and GaAsP nanowire. Band gap tunable, high quality self-seeded GaAsP nanowires would be beneficial for solar cell applications.

Chapter 6: Gas sensor application

In this chapter, we investigate the nanowire/polymer hybrid gas sensors for room temperature sensing of volatile organic compounds such as methanol and toluene.[1] Self-seeded GaAs nanowires grown on GaAs (110) and GaAs (111)A are chosen based on the high densities of nanowire that can be achieved. GaAs nanowires are coated with polymer and tested for sensing of methanol and toluene.

6.1. Introduction

Although we acclaim the semiconductor nanowires due to their ability to combine optoelectronic properties of semiconductors with one-dimensional morphology, morphological aspects of nanowires such as increased surface area may be beneficial for other applications. Nanowires provide high surface-to-volume ratio and are aligned on a substrate *via* epitaxial relationship. This highly uniform nanowire arrays can be utilized as a scaffold in other applications, such as gas sensors. Gas sensors can be built by coating a surface with a conducting polymer layer, where polymer resistance depends on surface coverage of adsorbed gases that is being detected, defined as chemiresistor. Nanowire morphology addresses some of the challenges of gas sensor applications such that the sensitivity and signal to noise ratio would be increased with increased surface area. Such gas sensors have been demonstrated using carbon nanotube arrays, where increased surface area was essential for sensitivity and response of gas

---

[1] The gas sensor application project is performed in collaboration with Xiaoxue Wang, Dr. Hilal Goktas and Prof. Karen Gleason in Chemical Engineering Department at Massachusetts Institute of Technology.

sensors.[134] In this case, however, the conformal coating of polymer on the carbon nanotube scaffold was challenging due to clumping of carbon nanotubes. Good conformal coating on GaAs nanowire arrays would be possible and enhanced gas sensing response could be achieved for nanowire/polymer chemical sensors. We have investigated using GaAs nanowires grown on (110) and (111)A substrates in gas sensor applications and high resistive response of GaAs/polymer gas sensors is observed. Since this application is not the main scope of this thesis and this is an ongoing effort, we describe some of the progress with GaAs/polymer gas sensors briefly below.

6.2. Gas sensor device structure

Self-seeded GaAs nanowires are grown on GaAs (110) and GaAs (111)A substrates as described in section 2.1.2. The knowledge built in Chapter 4: is utilized to obtain nanowires with different densities, and we used nanowires grown on (110) substrate to provide medium density (Figure 6.1a) and nanowires grown on (111)A substrate to provide high density (Figure 6.1b). The structure of the gas sensor is shown schematically in Figure 6.1c, where nanowires are coated with polymer and two aluminum alligator clips on both ends of the samples are used to measure the resistance change when exposed to analytes. Nanowires are conformally coated with poly(3,4-ethylenedioxylthiophene) (PEDOT) using oxidative chemical vapor deposition (oCVD) (Figure 6.1 d,e). The thickness of the polymer coating is controlled by the duration time of oCVD. The measured thickness of the polymer is between 100-150 nm.

The test on the sensing performance was conducted on a homemade test chamber. During measurement, concentration of 0-2400 ppm of analyte gas is flown with N_2 carrier gas (3000 sccm). The testing is performed in a controlled flow oven, and the temperature is set at 30°C.

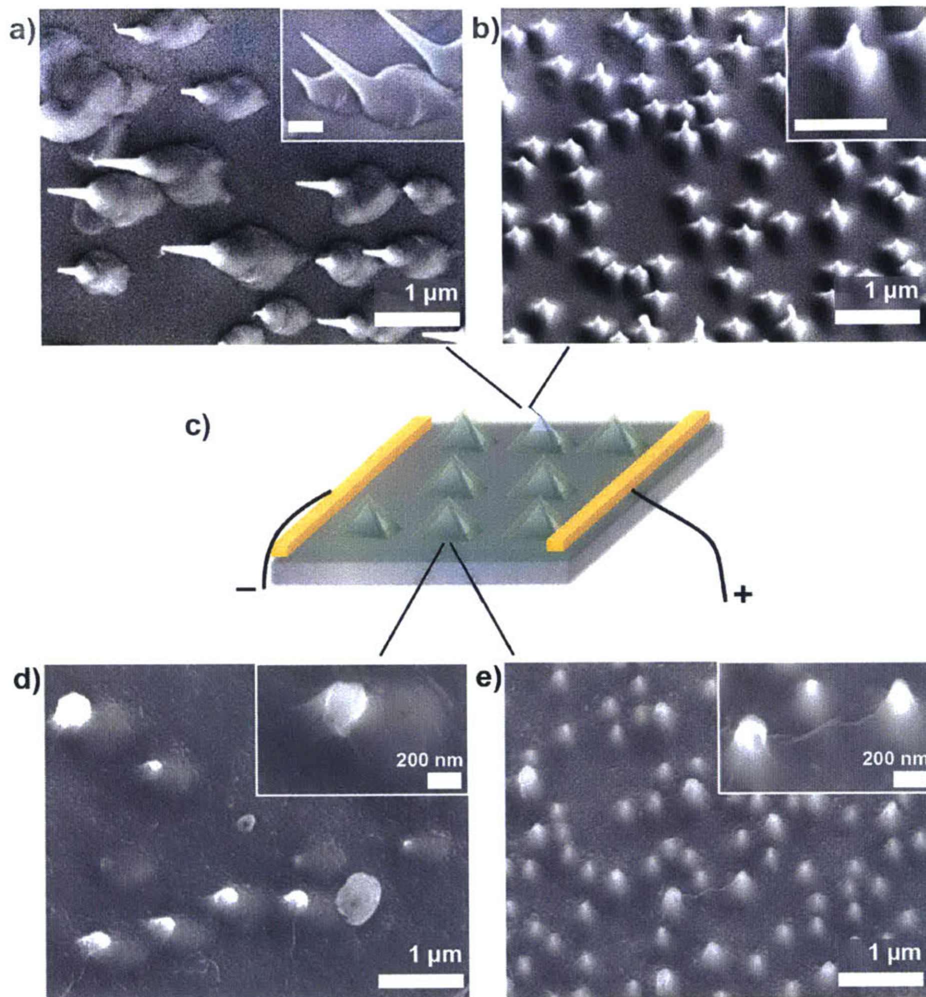

Figure 6.1 The structure of GaAs nanowire/PEDOT polymer gas sensor. a-b) SEM images of GaAs nanowires grown on (110) substrate (shown at top view) and (111)A substrate (shown at 45° tilt), respectively. The insets show the nanowire morphology at 45° tilt, scale bar is 500nm. c) Schematic of gas sensor device structure, where GaAs nanowires are coated with PEDOT polymer and metal contacts are placed to measure the resistance. d-e) SEM images of PEDOT polymer coating on GaAs nanowires grown on GaAs (110) and (111)A, respectively (shown at 45° tilt). Conformal coating of polymer can be seen in the insets of the images.

6.3. Volatile organic compound sensing using GaAs/polymer chemiresistors

The sensing response of gas sensors was measured for two different volatile organic compound analytes: methanol and toluene (Figure 6.2). For each analyte, gas sensors based on different density of GaAs nanowires were used to measure the resistive response. For both analytes, the sensors with higher density exhibit a larger absolute resistive response. Since higher density arrays provide a larger surface area, this larger resistive response is expected with the increase of sensing area. Among different analytes (methanol and toluene, Figure 6.2), the resistive response of PEDOT polymer is larger in methanol than toluene. This could be due to the polar nature of methanol compared to toluene. shows the resistive response of gas sensors to methanol and toluene, respectively.

The resistive response is defined as

$$Resistive\ response\ (\%) = \frac{R_{gas} - R_0}{R_0} \times 100$$

where R_{gas} is the device resistance with the presence of the analyte gas and R_0 is the resistance of the device exposed to nitrogen gas with the same flow rate and temperature.

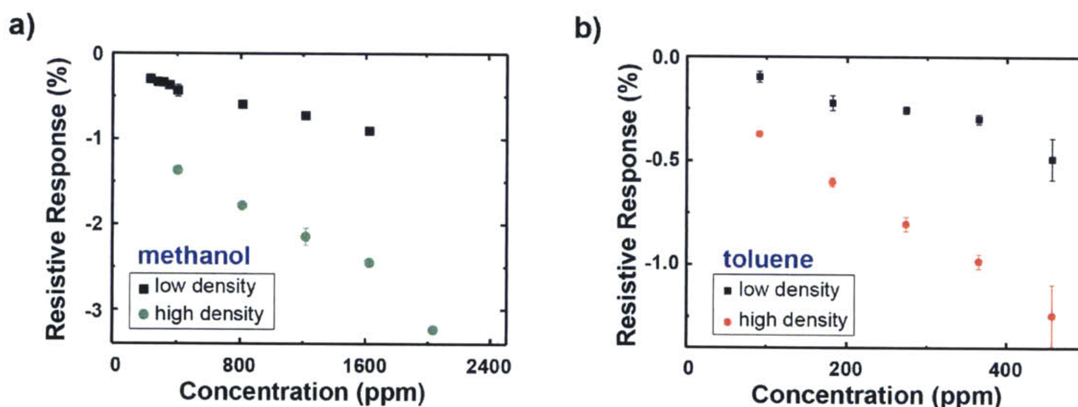

Figure 6.2 Resistive response of GaAs/PEDOT polymer gas sensors to a) methanol and b) toluene. Two types of gas sensors is used based on the density of GaAs nanowires. Ga sensors based on high density nanowire arrays give a larger absolute resistive response, suggesting the importance of surface area increase as a result of density increase.

6.4. Conclusion

We have investigated a potential application of GaAs nanowires in volatile organic compound sensing. The morphology of nanowires provide increased surface area, which increases the sensing quality of these devices. GaAs nanowires grown on (110) and (111)A substrates were conformally coated with PEDOT polymer and resistive response of PEDOT polymer was measured as a function of analyte concentration. The analytes used in this project were methanol and toluene. High signal-to-noise ratio, room temperature operation gas sensors are viable alternative sensor direction.

Chapter 7: Conclusions

In this thesis, we established an experimental framework for self-seeded growth of III-V nanowires by MOCVD. Nanowires are potential building blocks for a range of opto-electronic applications, and thanks to their non-planar morphology they offer potential advantages in the physical processes that leads to enhanced absorption, reduced reflection, or confinement of carriers. To achieve the potential advantages of nanowires for device applications, controlled growth in terms of morphology, alignment, areal density, and composition is required. Furthermore, high purity of materials that is achieved in thin film growth should be ideally achieved in nanowire growth. Whereas typical nanowire growth involves a foreign metal seed particle, nanowire growth *via* a self-seeded mechanism eliminates possible incorporation of impurities from foreign the metal seed by using one of the constituent elements of the nanowire as the seed particle. In this thesis, we established controlled growth of self-seeded binary and ternary III-V nanowires in the case of GaAs and GaAsP materials systems.

7.1. Summary of the thesis

Controlled self-seeded III-V nanowire growth was investigated in three distinct stages. First, we established self-seeded growth of III-V binary nanowires and demonstrated GaAs nanowire growth using MOCVD where *in situ* deposited Ga droplets were used as seed particles. Next, density and diameter control of self-seeded nanowire arrays were demonstrated in Chapter 4. Next, these findings on binary GaAs nanowire growth were extended into self-seeded ternary

GaAsP nanowire growth and composition of $GaAs_{1-x}P_x$ nanowires was achieved between $x = 0 – 0.3$ as well as GaP ($x = 1$) nanowire growth was demonstrated.

In Chapter 3, self-seeded GaAs nanowire growth was achieved by a two-step growth. We have demonstrated the importance of separation of seed deposition temperature and nanowire growth temperature to achieve growth of highly reproducible, high yield vertical nanowire arrays. Furthermore, by investigating the morphology and structure of these nanowires, we were able to elucidate the growth mechanism of Ga-seeded GaAs nanowires. To summarize, *in situ* Ga deposition results in formation of Ga droplets on the substrate. When nanowire growth was initiated by flowing Ga and As precursors, nanowire nucleation starts with a wider base that has a high degree of tapering followed by the nanowire growth, where nanowires have a smaller degree of tapering compared to the base. Investigation of the tapering behavior among nanowires with varied diameters has shown that the tapering rate is independent of the starting diameter. With this knowledge, tapering rate was modeled by relating seed diameter change with respect to the growth rate, and seed diameter was calculated using the seed volume changes due to incorporation and extraction of Ga. This model shows that the tapering is dependent of the Ga flux into the seed particle and the growth rate. We also investigated radial shell growth, which occurs due to incorporation of precursors directly on the nanowire sidewalls *via* vapor-solid mechanism. The presence of radial shell growth was only found for longer growth durations, which showed that once Ga seed is consumed, precursors incorporate to the nanowire sidewalls *via* VS mechanism. Radial shell growth was eliminated by optimized growth durations. These findings on nucleation and growth mechanisms of Ga-seeded GaAs nanowire arrays are expected to be similar for other self-seeded III-V nanowires and therefore can guide the research for other material systems.

In Chapter 4, density and diameter control of Ga-seeded GaAs nanowire arrays were achieved by varying seed deposition temperature and substrate orientation. Density of nanowires was increased from 5.5×10^{-3} nanowires/μm^2 to 82.2×10^{-3} nanowires/μm^2, whereas nanowire diameter was decreased from 1.3 μm to 167 nm by decreasing seed deposition temperature from 600°C to 500°C. Furthermore, substrate orientation was found to have a key impact on nanowire density and diameter. For the same seed deposition and nanowire growth procedures, nanowires grown on GaAs (111)B substrates had smallest density and largest average diameter. Nanowires grown on GaAs (110) had medium density and diameter, whereas nanowires grown on GaAs (111)A substrates had the highest density and smallest nanowire diameter. This vast difference of density, almost three orders of magnitude, is caused by only the substrate orientation and is linked to the seed nucleation kinetics – a change in chemical potential of adsorbed Ga atoms and surface energies of substrates would play a role in the seed formation. This result illustrates the importance of surface properties and versatility of density control of self-seeded nanowire growth.

In Chapter 5, ternary $GaAs_{1-x}P_x$ nanowire growth on GaAs (111)B substrate was demonstrated using Ga-seeded nanowire growth mechanism. We achieved composition control between $x = 0 - 0.3$ as well as demonstrated GaP ($x = 1$) nanowire growth. Composition control was achieved by altering the relative percentages of group-V precursors during growth. P content has shown a nonlinear relationship with respect to the precursor (*i.e.* phosphine) flow percentage; however, this behavior was fitted to an equation derived in a similar way to thin film experiments. This analysis allows us to relate controlled composition of ternary nanowires to the growth parameters. The strain in GaAsP nanowires due to lattice mismatch between GaAs and GaAsP was investigated using reciprocal space mapping and it was observed that most of the

strain is relaxed, as expected in nanowire systems. The cathodoluminescence emission of GaAsP nanowire base indicated the high crystalline quality of GaAsP nanowires, which suggested elastic accommodation of strain due lattice mismatch. High quality, compositionally controlled ternary nanowires enables band gap engineering, which would be beneficial for solar cell applications.

The implications of this work can be summarized as following: in this thesis, high throughput, highly scalable self-seeded III-V nanowire growth method has been established and GaAs and GaAsP nanowire grown with this method has been demonstrated. Ga-seeded nanowire growth by MOCVD had very limited success prior to this work, whereas MBE-grown Ga-seeded GaAs nanowires were demonstrated; therefore, our work opens up realm of Ga-based III-V binary and ternary nanowire growth using MOCVD, where high throughput and scalability can be achieved. Furthermore, the two-step method developed for self-seeded nanowire growth, where *in situ* seed deposition at higher temperatures is followed by nanowire growth at lower temperatures, has been essential to control the density and diameter of nanowires. Because nanowire growth can be achieved within a limited growth parameter space, decoupling of seed deposition and nanowire growth parameter spaces enables density and diameter control required from self-seeded nanowire growth. Two-step method can be applied to other materials system to achieve diameter and density control of self-seeded nanowire growth. Lastly, after demonstration of self-seeded mechanism for binary materials, we extended this work to ternary materials where band gap engineering through compositional control is possible. Composition control affects the band gap and lattice parameter simultaneously; however, lattice mismatch can be accommodated in nanowires to some extend thanks to effective relaxation at the nanowire sidewalls. Band gap engineering of ternary nanowires with minimum constraints on lattice mismatch would open up

the possibilities in opto-electronic devices that cannot be readily achieved in devices based on a planar morphology.

7.2. Suggested future work

7.2.1 Nanowire growth on more abundant substrates

In this thesis, we have demonstrated III-V nanowire growth on III-V substrates by MOCVD. However, from a cost and scalability perspective, more abundant and less expensive Si substrates can be utilized for nanowire growth. Therefore, an extension of the thesis work could focus on Ga-seeded nanowire growth on Si substrates by MOCVD. According to the knowledge developed in this thesis, the density and diameter of nanowires would be dependent on the surface energy of Si substrates as well as chemical potential of Ga adatom on Si substrate. Further considerations for the growth of self-seeded nanowire growth on Si substrate can be acquired from literature: Ga-seeded GaAs nanowire growth on Si substrates has been demonstrated in MBE and silicon oxide layer was found to be important to immobilize Ga droplets.

7.2.2 Axial heterostructures

Axial heterostructures, where abrupt compositional changes occur along the nanowire length, can be beneficial to localize carriers along the nanowire growth direction for the optoelectronic applications. In the self-seeded mechanism, such abrupt axial structures should be possible for compositional changes of group-V material due to the low solubility of group-V element in group-III seed particle. Changing precursors of group-V material would result in change in the composition of nanowire. It should be noted that a purge step might be necessary to achieve abrupt transition of composition, since the remaining precursors on the reactor walls could

incorporate into the nanowire and create a compositional gradient at the heterostructure interface. For axial structures achieved by compositional changes of group-III materials, abrupt changes in composition would be more challenging since the seed particle consists of the group-III element. One possible route for achieving abrupt changes in composition of group-III element would be consumption of seed particle first and then restarting growth by implanting new seed particles with desired composition only on the nanowires. In this approach, a mask layer on the substrate may be required to facilitate selective placing of seed particles on nanowires.

References

1. Duan, X., Huang, Y., Cui, Y., Wang, J. & Lieber, C. M. Indium phosphide nanowires as building blocks for nanoscale electronic and optoelectronic devices. *Nature* **409,** 66–69 (2001).
2. Thelander, C. *et al.* Nanowire-based one-dimensional electronics. *Mater. Today* **9,** 28–35 (2006).
3. Li, Y., Qian, F., Xiang, J. & Lieber, C. M. Nanowire electronic and optoelectronic devices. *Mater. Today* **9,** 18–27 (2006).
4. Garnett, E., Brongersma, M., Cui, Y. & McGehee, M. Nanowire Solar Cells. *Annu. Rev. Mater. Res.* **41,** 269–295 (2011).
5. Borgström, M. T. *et al.* Nanowires With Promise for Photovoltaics. *IEEE J. Sel. Top. Quantum Electron.* **17,** 1050–1061 (2011).
6. Holm, J. V. *et al.* Surface-passivated GaAsP single-nanowire solar cells exceeding 10% efficiency grown on silicon. *Nat. Commun.* **4,** 1498 (2013).
7. Mariani, G., Scofield, A. C., Hung, C.-H. & Huffaker, D. L. GaAs nanopillar-array solar cells employing in situ surface passivation. *Nat. Commun.* **4,** 1497 (2013).
8. Wallentin, J. *et al.* InP Nanowire Array Solar Cells Achieving 13.8% Efficiency by Exceeding the Ray Optics Limit. *Science* **339,** 1057–1060 (2013).
9. Guo, W., Zhang, M., Banerjee, A. & Bhattacharya, P. Catalyst-Free InGaN/GaN Nanowire Light Emitting Diodes Grown on (001) Silicon by Molecular Beam Epitaxy. *Nano Lett.* **10,** 3355–3359 (2010).
10. Qian, F., Gradečak, S., Li, Y., Wen, C.-Y. & Lieber, C. M. Core/Multishell Nanowire Heterostructures as Multicolor, High-Efficiency Light-Emitting Diodes. *Nano Lett.* **5,** 2287–2291 (2005).
11. Li, Y. *et al.* Dopant-Free GaN/AlN/AlGaN Radial Nanowire Heterostructures as High Electron Mobility Transistors. *Nano Lett.* **6,** 1468–1473 (2006).
12. Miao, X. & Li, X. Scalable Monolithically Grown AlGaAs-GaAs Planar Nanowire High-Electron-Mobility Transistor. *IEEE Electron Device Lett.* **32,** 1227–1229 (2011).
13. Larrieu, G. & Han, X.-L. Vertical nanowire array-based field effect transistors for ultimate scaling. *Nanoscale* **5,** 2437–2441 (2013).
14. Egard, M. *et al.* Vertical InAs Nanowire Wrap Gate Transistors with ft > 7 GHz and fmax > 20 GHz. *Nano Lett.* **10,** 809–812 (2010).
15. Zhang, C. & Li, X. III-V Nanowire Transistors for Low-Power Logic Applications: A Review and Outlook. *IEEE Trans. Electron Devices* **63,** 223–234 (2016).
16. Tomioka, K., Yoshimura, M. & Fukui, T. A III-V nanowire channel on silicon for high-performance vertical transistors. *Nature* **488,** 189–192 (2012).
17. Nah, J., Dillen, D. C., Varahramyan, K. M., Banerjee, S. K. & Tutuc, E. Role of Confinement on Carrier Transport in Ge–SixGe1–x Core–Shell Nanowires. *Nano Lett* (2011). doi:10.1021/nl2030695
18. Nduwimana, A., Musin, R. N., Smith, A. M. & Wang, X.-Q. Spatial Carrier Confinement in Core–Shell and Multishell Nanowire Heterostructures. *Nano Lett.* **8,** 3341–3344 (2008).
19. Yan, R., Gargas, D. & Yang, P. Nanowire photonics. *Nat Photon* **3,** 569–576 (2009).
20. Ra, Y.-H., Navamathavan, R., Park, J.-H. & Lee, C.-R. Coaxial InxGa1–xN/GaN Multiple Quantum Well Nanowire Arrays on Si(111) Substrate for High-Performance Light-Emitting Diodes. *Nano Lett.* **13,** 3506–3516 (2013).

21. Chu, S. *et al.* Electrically pumped waveguide lasing from ZnO nanowires. *Nat. Nanotechnol.* **6,** 506–510 (2011).
22. Chesin, J., Zhou, X. & Gradečak, S. Light extraction in individual GaN nanowires on Si for LEDs. in *Proceedings of SPIE* **8467,** 846703–846703 (2012).
23. Diedenhofen, S. L. *et al.* Controlling the Directional Emission of Light by Periodic Arrays of Heterostructured Semiconductor Nanowires. *ACS Nano* **5,** 5830–5837 (2011).
24. Saxena, D. *et al.* Optically pumped room-temperature GaAs nanowire lasers. *Nat. Photonics* **7,** 963–968 (2013).
25. Kayes, B. M., Atwater, H. A. & Lewis, N. S. Comparison of the device physics principles of planar and radial p-n junction nanorod solar cells. *J. Appl. Phys.* **97,** 114302 (2005).
26. Ke Sun *et al.* Compound Semiconductor Nanowire Solar Cells. *IEEE J. Sel. Top. Quantum Electron.* **17,** 1033–1049 (2011).
27. Yu, K. & Chen, J. Enhancing Solar Cell Efficiencies through 1-D Nanostructures. *Nanoscale Res. Lett.* **4,** 1–10 (2008).
28. Zhu, J. *et al.* Optical Absorption Enhancement in Amorphous Silicon Nanowire and Nanocone Arrays. *Nano Lett* **9,** 279–282 (2008).
29. Kelzenberg, M. D. *et al.* Enhanced absorption and carrier collection in Si wire arrays for photovoltaic applications. *Nat. Mater.* **9,** 239–244 (2010).
30. Muskens, O. L. *et al.* Large Photonic Strength of Highly Tunable Resonant Nanowire Materials. *Nano Lett.* **9,** 930–934 (2009).
31. Czaban, J. A., Thompson, D. A. & LaPierre, R. R. GaAs Core−Shell Nanowires for Photovoltaic Applications. *Nano Lett.* **9,** 148–154 (2009).
32. Colombo, C., Heiβ, M., Grätzel, M. & Fontcuberta i Morral, A. Gallium arsenide p-i-n radial structures for photovoltaic applications. *Appl. Phys. Lett.* **94,** 173108 (2009).
33. Wagner, R. S. & Ellis, W. C. VAPOR-LIQUID-SOLID MECHANISM OF SINGLE CRYSTAL GROWTH. *Appl. Phys. Lett.* **4,** 89–90 (1964).
34. Huang, Z., Fang, H. & Zhu, J. Fabrication of Silicon Nanowire Arrays with Controlled Diameter, Length, and Density. *Adv. Mater.* **19,** 744–748 (2007).
35. Talin, A. A., Hunter, L. L., Léonard, F. & Rokad, B. Large area, dense silicon nanowire array chemical sensors. *Appl. Phys. Lett.* **89,** 153102 (2006).
36. Huang, Z., Geyer, N., Werner, P., de Boor, J. & Gösele, U. Metal-Assisted Chemical Etching of Silicon: A Review. *Adv. Mater.* **23,** 285–308 (2011).
37. Hobbs, R. G., Petkov, N. & Holmes, J. D. Semiconductor Nanowire Fabrication by Bottom-Up and Top-Down Paradigms. *Chem. Mater.* **24,** 1975–1991 (2012).
38. Zhang, M.-L. *et al.* Preparation of Large-Area Uniform Silicon Nanowires Arrays through Metal-Assisted Chemical Etching. *J Phys Chem C* **112,** 4444–4450 (2008).
39. Li, Q. *et al.* Optical performance of top-down fabricated InGaN/GaN nanorod light emitting diode arrays. *Opt. Express* **19,** 25528–25534 (2011).
40. Jalabert, L. *et al.* High aspect ratio GaAs nanowires made by ICP-RIE etching using Cl2/N2 chemistry. *Microelectron. Eng.* **85,** 1173–1178 (2008).
41. Chang, S., Chuang, V. P., Boles, S. T., Ross, C. A. & Thompson, C. V. Densely Packed Arrays of Ultra-High-Aspect-Ratio Silicon Nanowires Fabricated using Block-Copolymer Lithography and Metal-Assisted Etching. *Adv. Funct. Mater.* **19,** 2495–2500 (2009).
42. Chang, S., Chuang, V. P., Boles, S. T. & Thompson, C. V. Metal-Catalyzed Etching of Vertically Aligned Polysilicon and Amorphous Silicon Nanowire Arrays by Etching Direction Confinement. *Adv. Funct. Mater.* **20,** 4364–4370 (2010).

43. Fontcuberta i Morral, A., Arbiol, J., Prades, J. D., Cirera, A. & Morante, J. R. Synthesis of Silicon Nanowires with Wurtzite Crystalline Structure by Using Standard Chemical Vapor Deposition. *Adv. Mater.* **19,** 1347–1351 (2007).
44. Tambe, M. J., Lim, S. K., Smith, M. J., Allard, L. F. & Gradečak, S. Realization of defect-free epitaxial core-shell GaAs/AlGaAs nanowire heterostructures. *Appl. Phys. Lett.* **93,** 151917–151917–3 (2008).
45. Lim, S. K., Tambe, M. J., Brewster, M. M. & Gradečak, S. Controlled Growth of Ternary Alloy Nanowires Using Metalorganic Chemical Vapor Deposition. *Nano Lett* **8,** 1386–1392 (2008).
46. Harmand, J. C. *et al.* Analysis of vapor-liquid-solid mechanism in Au-assisted GaAs nanowire growth. *Appl. Phys. Lett.* **87,** 203101 (2005).
47. Ikejiri, K., Noborisaka, J., Hara, S., Motohisa, J. & Fukui, T. Mechanism of catalyst-free growth of GaAs nanowires by selective area MOVPE. *J. Cryst. Growth* **298,** 616–619 (2007).
48. Paetzelt, H., Gottschalch, V., Bauer, J., Benndorf, G. & Wagner, G. Selective-area growth of GaAs and InAs nanowires--homo- and heteroepitaxy using SiNx templates. *J. Cryst. Growth* **310,** 5093–5097 (2008).
49. Dick, K. A. A review of nanowire growth promoted by alloys and non-alloying elements with emphasis on Au-assisted III-V nanowires. *Prog. Cryst. Growth Charact. Mater.* **54,** 138–173 (2008).
50. Bauer, J., Paetzelt, H., Gottschalch, V. & Wagner, G. GaAs nanowires grown by MOVPE. *Phys. Status Solidi B* **247,** 1294–1309 (2010).
51. Zhou, X., Chesin, J., Crawford, S. & Gradečak, S. Using seed particle composition to control structural and optical properties of GaN nanowires. *Nanotechnology* **23,** 285603 (2012).
52. Han, N. *et al.* Crystal phase and growth orientation dependence of GaAs nanowires on NixGay seeds via vapor-solid-solid mechanism. *Appl. Phys. Lett.* **99,** 083114 (2011).
53. Hillerich, K., Messing, M. E., Reine Wallenberg, L., Deppert, K. & Dick, K. A. Epitaxial InP nanowire growth from Cu seed particles. *J. Cryst. Growth* **315,** 134–137 (2011).
54. Heun, S. *et al.* Coexistence of Vapor–Liquid–Solid and Vapor–Solid–Solid Growth Modes in Pd-Assisted InAs Nanowires. *Small* **6,** 1935–1941 (2010).
55. Heun, S. *et al.* Pd-Assisted Growth of InAs Nanowires. *Cryst. Growth Des.* **10,** 4197–4202 (2010).
56. Xu, H. *et al.* Defect-Free <110> Zinc-Blende Structured InAs Nanowires Catalyzed by Palladium. *Nano Lett.* **12,** 5744–5749 (2012).
57. Wacaser, B. A. *et al.* Preferential Interface Nucleation: An Expansion of the VLS Growth Mechanism for Nanowires. *Adv. Mater.* **21,** 153–165 (2009).
58. Wen, C.-Y., Tersoff, J., Reuter, M. C., Stach, E. A. & Ross, F. M. Step-Flow Kinetics in Nanowire Growth. *Phys. Rev. Lett.* **105,** 195502 (2010).
59. Hofmann, S. *et al.* Ledge-flow-controlled catalyst interface dynamics during Si nanowire growth. *Nat. Mater.* **7,** 372–375 (2008).
60. Wen, C.-Y. *et al.* Formation of Compositionally Abrupt Axial Heterojunctions in Silicon-Germanium Nanowires. *Science* **326,** 1247–1250 (2009).
61. Wen, C.-Y. *et al.* Periodically Changing Morphology of the Growth Interface in Si, Ge, and GaP Nanowires. *Phys. Rev. Lett.* **107,** 025503 (2011).
62. Johansson, J. *et al.* Structural properties of <111>B -oriented III-V nanowires. *Nat Mater* **5,** 574–580 (2006).

63. Lim, S. K., Crawford, S. & Gradečak, S. Growth mechanism of GaN nanowires: preferred nucleation site and effect of hydrogen. *Nanotechnology* **21,** 345604 (2010).
64. Woo, R. L. *et al.* Kinetic Control of Self-Catalyzed Indium Phosphide Nanowires, Nanocones, and Nanopillars. *Nano Lett.* **9,** 2207–2211 (2009).
65. Mattila, M., Hakkarainen, T., Lipsanen, H., Jiang, H. & Kauppinen, E. I. Catalyst-free growth of In(As)P nanowires on silicon. *Appl. Phys. Lett.* **89,** 063119 (2006).
66. Mandl, B. *et al.* Growth Mechanism of Self-Catalyzed Group III−V Nanowires. *Nano Lett.* **10,** 4443–4449 (2010).
67. Fontcuberta i Morral, A., Colombo, C., Abstreiter, G., Arbiol, J. & Morante, J. R. Nucleation mechanism of gallium-assisted molecular beam epitaxy growth of gallium arsenide nanowires. *Appl. Phys. Lett.* **92,** 063112–3 (2008).
68. Lim, S. K., Crawford, S., Haberfehlner, G. & Gradečak, S. Controlled Modulation of Diameter and Composition along Individual III–V Nitride Nanowires. *Nano Lett.* **13,** 331–336 (2013).
69. Crawford, S., Lim, S. K. & Gradečak, S. Fundamental Insights into Nanowire Diameter Modulation and the Liquid/Solid Interface. *Nano Lett.* **13,** 226–232 (2013).
70. Hiesinger, P. Hall-effect levels in Ag- and Au-doped p-type GaAs. *Phys. Status Solidi A* **33,** K39–K41 (1976).
71. Yan, Z. X. & Milnes, A. G. Deep Level Transient Spectroscopy of Silver and Gold Levels in LEC Grown Gallium Arsenide. *J. Electrochem. Soc.* **129,** 1353–1356 (1982).
72. Breuer, S. *et al.* Suitability of Au- and Self-Assisted GaAs Nanowires for Optoelectronic Applications. *Nano Lett.* **11,** 1276–1279 (2011).
73. Allen, J. E. *et al.* High-resolution detection of Au catalyst atoms in Si nanowires. *Nat. Nanotechnol.* **3,** 168–173 (2008).
74. Moutanabbir, O. *et al.* Colossal injection of catalyst atoms into silicon nanowires. *Nature* **496,** 78–82 (2013).
75. Bar-Sadan, M., Barthel, J., Shtrikman, H. & Houben, L. Direct Imaging of Single Au Atoms Within GaAs Nanowires. *Nano Lett.* **12,** 2352–2356 (2012).
76. Tambe, M. J., Ren, S. & Gradečak, S. Effects of Gold Diffusion on n-Type Doping of GaAs Nanowires. *Nano Lett.* **10,** 4584–4589 (2010).
77. Ren, S. *et al.* Heterojunction Photovoltaics Using GaAs Nanowires and Conjugated Polymers. *Nano Lett* **11,** 408–413 (2011).
78. Mandl, B. *et al.* Au-Free Epitaxial Growth of InAs Nanowires. *Nano Lett.* **6,** 1817–1821 (2006).
79. Forbes, D., Hubbard, S., Raffaelle, R. & McNatt, J. S. Au-catalyst-free epitaxy of InAs nanowires. *J. Cryst. Growth* **312,** 1391–1395 (2010).
80. Novotny, C. J. & Yu, P. K. L. Vertically aligned, catalyst-free InP nanowires grown by metalorganic chemical vapor deposition. *Appl. Phys. Lett.* **87,** 203111 (2005).
81. Colombo, C., Spirkoska, D., Frimmer, M., Abstreiter, G. & Fontcuberta i Morral, A. Ga-assisted catalyst-free growth mechanism of GaAs nanowires by molecular beam epitaxy. *Phys. Rev. B* **77,** 155326 (2008).
82. Tatebayashi, J., Lin, A., Wong, P. S., Hick, R. F. & Huffaker, D. L. Visible light emission from self-catalyzed GaInP/GaP core-shell double heterostructure nanowires on silicon. *J. Appl. Phys.* **108,** 034315 (2010).
83. Cirlin, G. E. *et al.* Self-catalyzed, pure zincblende GaAs nanowires grown on Si(111) by molecular beam epitaxy. *Phys. Rev. B* **82,** 035302 (2010).

84. Ambrosini, S., Fanetti, M., Grillo, V., Franciosi, A. & Rubini, S. Self-catalyzed GaAs nanowire growth on Si-treated GaAs(100) substrates. *J. Appl. Phys.* **109,** 094306 (2011).
85. Krogstrup, P. *et al.* Structural Phase Control in Self-Catalyzed Growth of GaAs Nanowires on Silicon (111). *Nano Lett.* **10,** 4475–4482 (2010).
86. Plissard, S. *et al.* Gold-free growth of GaAs nanowires on silicon: arrays and polytypism. *Nanotechnology* **21,** 385602 (2010).
87. Physical properties of gases, safety, MSDS, enthalpy, material compatibility, gas liquid equilibrium, density, viscosity, flammability, transport properties. Available at: http://encyclopedia.airliquide.com/. (Accessed: 27th March 2016)
88. Williams, D. B. & Carter, C. B. *Transmission Electron Microscopy: A Textbook for Materials Science*. (Springer, 2009).
89. BEARDEN, J. A. X-Ray Wavelengths. *Rev. Mod. Phys.* **39,** 78–124 (1967).
90. DiffracPlus LEPTOS 7 User Manual. (2009).
91. Hegedus, S. & Luque, A. *Handbook of Photovoltaic Science and Engineering*. (Wiley, 2011).
92. *CRC Handbook of Chemistry and Physics, 94th Edition*. (CRC Press, 2013).
93. Kasahara, J., Kajiwara, K. & Yamada, T. GaAs whiskers grown by a thermal decomposition method. *J. Cryst. Growth* **38,** 23–28 (1977).
94. Breuer, S., Karouta, F., Tan, H. H. & Jagadish, C. MOCVD growth of GaAs nanowires using Ga droplets. in *2012 Conference on Optoelectronic and Microelectronic Materials Devices (COMMAD)* 39–40 (2012). doi:10.1109/COMMAD.2012.6472349
95. Statkute, G. *et al.* GaAs Nanowire and Crystallite Growth on Amorphous Substrate from Metalorganic Precursors. *Jpn. J. Appl. Phys.* **49,** 020213 (2010).
96. Mohan, P., Bag, R., Singh, S., Kumar, A. & Tyagi, R. Mechanism of self-assembled growth of ordered GaAs nanowire arrays by metalorganic vapor phase epitaxy on GaAs vicinal substrates. *Nanotechnology* **23,** 025601 (2012).
97. Noborisaka, J., Motohisa, J. & Fukui, T. Catalyst-free growth of GaAs nanowires by selective-area metalorganic vapor-phase epitaxy. *Appl. Phys. Lett.* **86,** 213102 (2005).
98. Larsen, C. A., Buchan, N. I., Li, S. H. & Stringfellow, G. B. Decomposition mechanisms of trimethylgallium. *J. Cryst. Growth* **102,** 103–116 (1990).
99. Tersoff, J., Jesson, D. E. & Tang, W. X. Running Droplets of Gallium from Evaporation of Gallium Arsenide. *Science* **324,** 236 –238 (2009).
100. Caroff, P. *et al.* Controlled polytypic and twin-plane superlattices in iii–v nanowires. *Nat. Nanotechnol.* **4,** 50–55 (2009).
101. Algra, R. E. *et al.* Twinning superlattices in indium phosphide nanowires. *Nature* **456,** 369–372 (2008).
102. Burgess, T. *et al.* Twinning Superlattice Formation in GaAs Nanowires. *ACS Nano* **7,** 8105–8114 (2013).
103. Grap, T. *et al.* Self-catalyzed VLS grown InAs nanowires with twinning superlattices. *Nanotechnology* **24,** 335601 (2013).
104. Larsen, C. A., Li, S. H., Buchan, N. I., Stringfellow, G. B. & Brown, D. W. Kinetics of the reaction between trimethylgallium and arsine. *J. Cryst. Growth* **102,** 126–136 (1990).
105. Frank, M. M. *et al.* HfO2 and Al2O3 gate dielectrics on GaAs grown by atomic layer deposition. *Appl. Phys. Lett.* **86,** 152904 (2005).
106. Vasquez, R. P., Lewis, B. F. & Grunthaner, F. J. Cleaning chemistry of GaAs(100) and InSb(100) substrates for molecular beam epitaxy. *J. Vac. Sci. Technol. B* **1,** 791–794 (1983).

107. Hilner, E. *et al.* Ordering of the Nanoscale Step Morphology As a Mechanism for Droplet Self-Propulsion. *Nano Lett.* **9,** 2710–2714 (2009).
108. Goldstein, B., Szostak, D. J. & Ban, V. S. Langmuir evaporation from the (100),(111A), and (111B) faces of GaAs. *Surf. Sci.* **57,** 733–740 (1976).
109. Zhou, Z. Y., Zheng, C. X., Tang, W. X., Jesson, D. E. & Tersoff, J. Congruent evaporation temperature of GaAs(001) controlled by As flux. *Appl. Phys. Lett.* **97,** 121912 (2010).
110. Shin, J. C. *et al.* InxGa1-xAs Nanowires on Silicon: One-Dimensional Heterogeneous Epitaxy, Bandgap Engineering, and Photovoltaics. *Nano Lett* **11,** 4831–4838 (2011).
111. Rieger, T., Heiderich, S., Lenk, S., Lepsa, M. I. & Grützmacher, D. Ga-assisted MBE growth of GaAs nanowires using thin HSQ layer. *J. Cryst. Growth* **353,** 39–46 (2012).
112. Paek, J. H., Nishiwaki, T., Yamaguchi, M. & Sawaki, N. Catalyst free MBE-VLS growth of GaAs nanowires on (111)Si substrate. *Phys. Status Solidi C* **6,** 1436–1440 (2009).
113. Somaschini, C. *et al.* Control over the Number Density and Diameter of GaAs Nanowires on Si(111) Mediated by Droplet Epitaxy. *Nano Lett.* **13,** 3607–3613 (2013).
114. Ueda, T., Gao, Q. Z., Yamaichi, E., Yamagishi, C. & Akiyama, M. Growth of GaAs microcrystal by Ga droplet formation and successive As supply with low-pressure metalorganic chemical vapor deposition. *J. Cryst. Growth* **145,** 707–713 (1994).
115. Takebe, T., Fujii, M., Yamamoto, T., Fujita, K. & Watanabe, T. Orientation-dependent Ga surface diffusion in molecular beam epitaxy of GaAs on GaAs patterned substrates. *J. Appl. Phys.* **81,** 7273–7281 (1997).
116. Biegelsen, D. K., Bringans, R. D., Northrup, J. E. & Swartz, L.-E. Reconstructions of GaAs($\bar{1}\ \bar{1}\ \bar{1}$) surfaces observed by scanning tunneling microscopy. *Phys. Rev. Lett.* **65,** 452–455 (1990).
117. Moll, N., Kley, A., Pehlke, E. & Scheffler, M. GaAs equilibrium crystal shape from first principles. *Phys. Rev. B* **54,** 8844–8855 (1996).
118. Geisz, J. F. & Friedman, D. J. III-N-V semiconductors for solar photovoltaic applications. *Semicond. Sci. Technol.* **17,** 769 (2002).
119. Meillaud, F., Shah, A., Droz, C., Vallat-Sauvain, E. & Miazza, C. Efficiency limits for single-junction and tandem solar cells. *Sol. Energy Mater. Sol. Cells* **90,** 2952–2959 (2006).
120. Sun, W. *et al.* Spontaneous formation of core–shell GaAsP nanowires and their enhanced electrical conductivity. *J. Mater. Chem. C* **3,** 1745–1750 (2015).
121. Mohseni, P. K., Rodrigues, A. D., Galzerani, J. C., Pusep, Y. A. & LaPierre, R. R. Structural and optical analysis of GaAsP/GaP core-shell nanowires. *J. Appl. Phys.* **106,** 124306 (2009).
122. Svensson, C. P. T. *et al.* Epitaxially grown GaP/GaAs1−xPx/GaP double heterostructure nanowires for optical applications. *Nanotechnology* **16,** 936 (2005).
123. Zhang, Y. *et al.* Self-Catalyzed GaAsP Nanowires Grown on Silicon Substrates by Solid-Source Molecular Beam Epitaxy. *Nano Lett.* **13,** 3897–3902 (2013).
124. Sun, W. *et al.* Unequal P Distribution in Nanowires and the Planar Layer during GaAsP Growth on GaAs {111}B by Metal–Organic Chemical Vapor Deposition. *J. Phys. Chem. C* **117,** 19234–19238 (2013).
125. Samuelson, L., Omling, P. & Grimmeiss, H. G. Alloying mechanisms in MOVPE GaAs1-xPx. *J. Cryst. Growth* **61,** 425–426 (1983).
126. Smeets, E. T. J. M. Solid composition of GaAs1-xPx grown by organometallic vapour phase epitaxy. *J. Cryst. Growth* **82,** 385–395 (1987).

127. Takeyasu, M., Sakai, S., Soga, T. & Umeno, M. MOCVD Growth of GaAs(1-x)Px (x=0-1) and Fabrication of GaAs0.6P0.4 LED on Si Substrate. *Jpn. J. Appl. Phys.* **25,** 1388–1392 (1986).
128. Stringfellow, G. B. Thermodynamic aspects of organometallic vapor phase epitaxy. *J. Cryst. Growth* **62,** 225–229 (1983).
129. Leys, M. R., Titze, H., Samuelson, L. & Petruzzello, J. Growth and characterization of strained layers of GaAsxP1−x. *J. Cryst. Growth* **93,** 504–511 (1988).
130. Harrous, M. *et al.* Phosphine and arsine decomposition in CVD reactors for InP and InGaAs growth. *J. Cryst. Growth* **92,** 423–431 (1988).
131. Krautle, H., Roehle, H., Escobosa, A. & Beneking, H. Investigations on low temperature mo-cvd growth of GaAs. *J. Electron. Mater.* **12,** 215 – 222 (1983).
132. Kuo, C. P., Vong, S. K., Cohen, R. M. & Stringfellow, G. B. Effect of mismatch strain on band gap in III-V semiconductors. *J. Appl. Phys.* **57,** 5428–5432 (1985).
133. Nelson, R. J., Holonyak, N. & Groves, W. O. Free-exciton transitions in the optical absorption spectra of GaAs(1-x)Px. *Phys. Rev. B* **13,** 5415–5419 (1976).
134. Wang, X. *et al.* Room Temperature Resistive Volatile Organic Compound Sensing Materials Based on a Hybrid Structure of Vertically Aligned Carbon Nanotubes and Conformal oCVD/iCVD Polymer Coatings. *ACS Sens.* (2016). doi:10.1021/acssensors.5b00208